

**FINITE ELEMENT ANALYSIS OF AN EMPTY 37-ELEMENT
CANDU® FUEL BUNDLE TO STUDY THE EFFECTS OF
PRESSURE TUBE CREEP**

**ANALYSE PAR ÉLÉMENTS FINIS D'UNE GRAPPE DE
COMBUSTIBLE CANDU® VIDE À 37 CRAYONS POUR L'ÉTUDE
DES EFFETS DU FLUAGE DU TUBE DE FORCE**

A Thesis Submitted to the Division of Graduate Studies
of the Royal Military College of Canada
by

A/S Lt. Andy Lee, rmc, BEng

In Partial Fulfillment of the Requirements for the Degree of
Master of Applied Science

March 2020

© This paper may be used within the Department of National Defence but
copyright for open publication remains the property of the author.

Abstract

CANDU® fuel bundles and pressure tubes experience deformations over time, and the horizontal configuration of the bundle in a crept pressure tube causes coolant to bypass the bundle. The rods in the bundle can also deform and sag due to harsh reactor conditions and further reduce the sub-channel areas in the bundle. Parts of the bundle and sub-channels where the flow is limited may experience dryout earlier than expected due to reactor aging. Therefore, it is imperative to quantify the effects of pressure tube creep by modelling the bundle deformation inside a pressure tube.

This thesis seeks to first develop a 3D finite element model of a complete CANDU 37-element fuel bundle without pellets. Then the pressure tube was expanded to determine the effects of diametral creep on bundle deformations. Past efforts in simulations and experimental work were compiled, yet no full bundle deformation model with contact was established. Post Irradiation Examinations and bundle heat up tests were performed, and their profilometry data were used to establish a qualitative benchmark for the deformation of the full bundle model. The finite element model was constructed using the commercial finite element software ANSYS. Contact was demonstrated between the appendages, and sensitivity of the deformation to different boundary conditions was explored. The complexity of the model necessitated the use of high-powered computing hardware. Expanding the pressure tube up to 8% diametral creep demonstrated the proper functioning of the spacer pads and bearing pads in preventing sheath to sheath contact at the midplane, and sheath to pressure tube contact. However, the quarter plane was deemed to be the critical region due to the lack of spacer pads preventing excessive rod bowing.

Keywords: CANDU, fuel bundle, deformations, finite element method, pressure tube diametral creep, ANSYS, sub-channels.

Résumé

Les grappes de combustible CANDU® et les tubes de force subissent des déformations au fil du temps, et la configuration horizontale de la grappe dans un tube de force déformé par le fluage permet au caloporteur de contourner la grappe. Les crayons de la grappe peuvent aussi se déformer et s'affaisser à cause des dures conditions ambiantes dans le réacteur et causer une réduction additionnelle des aires des sous-canaux. Des parties de la grappe et des sous-canaux où le débit du caloporteur est réduit peuvent subir des conditions d'assèchement prématurées causées par le vieillissement du réacteur. Il est donc important de quantifier les effets du fluage du tube de force en modélisant les déformations de la grappe à l'intérieur du tube de force.

Cette thèse vise d'abord à développer un modèle en trois dimensions d'une grappe de combustible CANDU® complète, mais sans les pastilles de combustible. Puis, les dimensions du tube de force ont été agrandies pour déterminer les effets du fluage diamétral sur la déformation de la grappe. On a compilé les résultats de tentatives passées de modélisation et de travail expérimental, qui cependant n'ont pas permis d'établir un modèle de déformation de la grappe entière. Des examens post-irradiation et des tests de chauffage de la grappe ont été effectués, et leurs résultats de profilométrie ont été utilisés pour établir un ensemble de données de référence pour le modèle de la déformation de la grappe entière. Le logiciel commercial d'éléments finis, ANSYS, a été utilisé pour construire le modèle par éléments finis. Le contact a été démontré entre les entretoises et on a exploré la sensibilité de la déformation aux conditions frontières. La grande complexité du modèle numérique a nécessité l'emploi de très grandes ressources de calcul. Une expansion par fluage diamétral du tube de force jusqu'à 8% a confirmé le fonctionnement approprié des entretoises et des patins qui ont empêché tout contact entre les gaines des crayons adjacents, de même qu'entre les gaines des crayons et la paroi du tube de force au plan situé au milieu de la grappe. Cependant, on a déterminé que le plan situé au quart de la longueur de la grappe était la région la plus critique à cause de l'absence d'entretoises et de patins qui empêchent tout gauchissement excessif du crayon de combustible.

Mots-clefs : CANDU®, grappe de combustible, déformations, méthode par éléments finis, fluage diamétral du tube de force, ANSYS, sous-canaux.

Contents

Abstract.....	ii
Résumé.....	iii
Contents.....	iv
List of Tables.....	viii
List of Figures.....	ix
List of Acronyms.....	xiv
Acknowledgements.....	xv
1. Introduction.....	1
2. Background.....	3
2.1 Reactor Operation.....	3
2.2 Fuel Channel Components.....	5
2.3 Bundle Deformation and Aging.....	8
2.4 Heat Transfer Mechanisms.....	10
2.5 Safety Analysis Techniques.....	11
3. State of the Art.....	13
3.1 Fuel codes.....	13
3.2 3D Mechanical Models and Experiments.....	14
3.3 3D Fluid dynamics model.....	17
3.4 Experimental Studies.....	18
4. Objectives of the Research.....	23
5. Theory.....	24

5.1 Solid Mechanics Equation	24
5.2 Finite Element Method	27
5.4 Non-Linearity.....	29
5.5 Contact.....	31
5.5.1 Parallel Computing	33
6. Preliminary Studies.....	37
6.1 Overall model approach.....	37
6.2 Single rod model description	38
6.2.1 Geometry and Element Type	38
6.2.2 Mesh.....	41
6.2.3 Contact.....	42
6.2.4 Material Properties.....	43
6.2.5 Loads and Boundary Conditions.....	44
6.2.5.1 Preliminary study on boundary conditions	44
6.2.5.2 Preliminary study on thermal loading	47
6.2.5.3 Preliminary study on bearing pad placement.....	47
6.2.6 Solution.....	48
6.3 Single Rod Results.....	49
6.3.1 Effects of Boundary Conditions.....	49
6.3.2 Effects of Thermal Loading	52
6.3.3 Effects of Bearing Pad Placement.....	53
6.4 Discussion and Conclusions	54
7. Thirty Seven Element bundle models	57

7.1 First iteration bundle model	57
7.1.1 First iteration bundle model description	57
7.1.1.1 Geometry and Element Type	57
7.1.1.2 Mesh.....	57
7.1.1.3 Contact.....	59
7.1.1.4 Material Properties.....	59
7.1.1.5 Loads and Boundary Conditions.....	59
7.1.1.6 Solution.....	61
7.1.2 Results.....	61
7.1.2.1 First iteration Full Bundle Results	61
7.1.2.2 Sensitivity Analysis on Web Constraint	64
7.1.2.3 Effects of applied load on bundle deformation.....	69
7.2 Crept PT Bundle Deformation Comparisons	75
7.2.1. 37-Element Final Bundle Model Description	75
7.2.2. Results.....	75
8. Discussion.....	80
9. Limitations	84
10. Conclusion	85
11. Recommendations.....	87
12. References.....	90
Appendices.....	94
Appendix A: CMC HPC Hardware Specifications.....	94
Appendix B: Major Dimensions for 1-Rod Model	95

Appendix C: Table of Mesh Settings.....	96
Appendix D: Full Bundle with crept PT axial views	97

List of Tables

Table 1: Electricity generated by source in Ontario from 2016 to 2018 [5].	2
Table 2: Contact type and behaviour [42].	31
Table 3: Zircaloy - 4 Young's Modulus temperature dependence [47].	43
Table 4: Zircaloy - 4 Norton creep constants temperature dependence [47].	43
Table 5: Preliminary studies using the single rod model.	44
Table 6: Boundary condition small scale test cases.	45
Table 7: Load condition small scale test cases.	47
Table 8: Boundary conditions sensitivity analysis on Full Bundle Cases.	65
Table 9: Vertical deflections of various endplate radial web axial constraints.	67
Table 9: Continued vertical deflections of various endplate radial web axial constraints.	68
Table 10: Gap measurement between rods 24 and 9.	78
Table 11: Major dimensions for 1-rod model.	95
Table 12: Mesh settings for full bundle model.	96

List of Figures

Figure 1: Percent increase in global energy demand, population, and GDP [2].	1
Figure 2: Pellets, rods, and bundles in the reactor core [8].	3
Figure 3: Bundle inside fuel channel and calandria tube [10].	4
Figure 4: Simplified CANDU reactor operations [8].	4
Figure 5: CANDU 37 element fuel bundle numbering (edited) [13].	5
Figure 6: Location of bearing pads, spacer pads, sub-channel flow.	6
Figure 7: CANDU 6 bundle design [7].	7
Figure 8: Bruce/Darlington plant bundle design [14].	7
Figure 9: By-pass flow in a crept PT with red arrows showing the diametral creep of the PT (edited) [15].	9
Figure 10: Effects of creep on pressure tubes [10].	9
Figure 11: Horizontal flow pattern with changing quality in heated tube [7].	11
Figure 12: Odd numbered outer element vertical deflections (um) [31].	19
Figure 13: Even numbered outer element vertical deflections (um) [31].	19
Figure 14: Outer element radial bow (mm) for both channels [13].	21
Figure 15: Simply supported beam with uniformly distributed load.	24
Figure 16: Both end cantilever beam with uniformly distributed load.	26
Figure 17: Effect of coarse and fine mesh in capturing geometry [34].	28
Figure 18: Newton Raphson Method [39].	30
Figure 19: Contact definition in ANSYS [40].	31

Figure 20: Normal force during contact [40].	32
Figure 21: Constraints for MPC Formulation [40].	33
Figure 22: Shared Memory Parallel Architecture [43].	34
Figure 23: Distributed Memory Parallel Architecture [43].	35
Figure 24: Runtimes compared to benchmark core count [46].	35
Figure 25: Full bundle isometric view with coordinate system.	38
Figure 26: Full bundle axial view.	39
Figure 27: Spacer pad contact pair misalignment.	40
Figure 28: Axial view of 1 rod model configuration inside pressure tube.	41
Figure 29: Mesh for the 1-rod in the PT.	42
Figure 30: Bundle free body diagrams.	45
Figure 31: Illustration of test 1.	45
Figure 32: Illustration of test 2.	46
Figure 33: Illustration of test 3.	46
Figure 34: Illustration of test 4.	46
Figure 35: Configuration of the pellets inside the rods [27].	47
Figure 36: One rod model with staggered BPs.	48
Figure 37: One rod model with in-line BPs.	48
Figure 38: Test 1 - vertical deflection (mm) of 1 rod at 55x scale with endplates axially fixed, centre BP bonded to PT.	49
Figure 39: Test 2 - vertical deflection (mm) of 1 rod at 96x scale with endplates axially fixed, all 3 BP bonded to PT.	50

Figure 40: Test 3 - vertical deflection (mm) of 1 rod at 51x scale with endplates axially free, centre BP bonded to PT.	50
Figure 41: Test 4 - vertical deflection (m) of 1 rod at 45x scale with endplates axially fixed, centre BP frictional condition, outer BPs bonded to PT	51
Figure 42: Vertical deflections (mm) lengthwise plot of BC test case 1.	51
Figure 43: Test 1 - side view of vertical deflections (mm) at 48x scale of an empty rod with vertical force, gravity, thermal creep, and constant thermal load.....	52
Figure 44: Test 2 - side view of vertical deflections (mm) at 44x scale of a rod with pellets and vertical force, gravity, thermal creep, and constant thermal load.	52
Figure 45: Test 3 - side view of vertical deflections (mm) at 67x scale of an empty rod with an axial thermal gradient.	53
Figure 46: Test 4 - side view of vertical deflections (mm) at 78x scale with pellets and thermal gradient.	53
Figure 47: Side view of vertical deflection (mm) of in line BPs at 78x scale.	54
Figure 48: Mesh convergence study on a single rod.....	55
Figure 49: Isometric view of the bundle and PT mesh.	58
Figure 50: Isometric view of the bundle mesh.....	58
Figure 51: Close up of a sheath.....	59
Figure 52: Remote displacements for the first iteration full bundle model.	60
Figure 53: First iteration full bundle vertical deflections (mm) true scale.	62
Figure 54: Vertical deflections (mm) of outer elements axial view 5x scale.....	63
Figure 55: Vertical deflections (mm) of rods 10 and 9 side view 19x scale.....	63

Figure 56: Vertical deflection (mm) of endplates with fixed webs (a) and constrained face (b) 5x scale.....	64
Figure 57: Test 2 - one endplate faced fixed, outer webs fixed	65
Figure 58: Test 3 - one endplate faced fixed, inner webs fixed	66
Figure 59: Test 6 - one endplate faced fixed, lower 4 webs fixed	66
Figure 60: Axial view of vertical deflections (mm) of entire bundle with nominal PT diameter (top) and 8% diametral creep (bottom) with pellet weight at true scale	70
Figure 61: Axial view of vertical deflections (mm) of entire bundle with nominal PT diameter (top) and 8% diametral creep (bottom) with 60 N at true scale.	71
Figure 62: Axial view of vertical deflections (mm) of entire bundle with nominal PT diameter (top) and 8% diametral creep (bottom) with 120 N at true scale.	72
Figure 63: Axial view of vertical deflections (mm) of entire bundle with nominal PT diameter (top) and 8% diametral creep (bottom) with 240 N at true scale.	73
Figure 64: Plot of outer elements' vertical deflections (mm) compared to undeformed bundle	74
Figure 65: Axial view of vertical deflections (mm) entire bundle (left), midplane (right), quarter plane (bottom) of nominal PT diameter at true scale.	76
Figure 66: Axial view of vertical deflections (mm) entire bundle (left), midplane (right), quarter plane (bottom) of 2% crept PT diameter at true scale.	76
Figure 67: Axial view of vertical deflections (mm) entire bundle (left), midplane (right), quarter plane (bottom) of 4% crept PT diameter at true scale.	77

Figure 68: Axial view of vertical deflections (mm) entire bundle (left), midplane (right), quarter plane (bottom) of 6% crept PT diameter at true scale. 77

Figure 69: Axial view of vertical deflections (mm) entire bundle (left), midplane (right), quarter plane (bottom) of 8% crept PT diameter at true scale. 78

Figure 70: Gap distance between rods 24 and 9 with increasing diametral creep. . 79

Figure 71: Hardware specifications of CMC Microsystem HPC. 94

Figure 72: Axial view of full bundle mesh with 0% PT diametral creep. 97

Figure 73: Axial view of full bundle mesh with 2% PT diametral creep. 97

Figure 74: Axial view of full bundle mesh with 4% PT diametral creep. 98

Figure 75: Axial view of full bundle mesh with 6% PT diametral creep. 98

Figure 76: Axial view of full bundle mesh with 8% PT diametral creep. 99

List of Acronyms

AECL	Atomic Energy of Canada Limited
ANSYS	Commercial Finite Element Analysis Software
BP	Bearing Pad
CAC	Centre for Advanced Computing
CANDU®	CANada Deuterium Uranium
CANFLEX	CANDU FLEXible
CCP	Critical Channel Power
CFD	Computational Fluid Dynamics
CMC	Supplier of Commercial and Academic Software
CNL	Canadian Nuclear Laboratories
CNSC	Canadian Nuclear Safety Commission
DOF	Degree of Freedom
ELESTRES	ELEment STRESs
FEA	Finite Element Analysis
FGR	Fission Gas Release
GUI	Graphical User Interface
HPC	High Power Computing
MATPRO	MATERial PROperties
MPC	Multiple Point Constraint
MRV	Magnetic Resonance Velocimetry
PT	Pressure Tube
RAM	Random Access Memory
RMC	Royal Military College
SP	Spacer Pad

Acknowledgements

First, I would like to express my gratitude for my dedicated supervisors Dr. Paul Chan and Dr. Diane Wowk for their tireless commitment, talent, leadership, guidance and support throughout my time at RMC, both as a cadet and an officer. Their devotion and skill to their crafts were inspiring as an undergraduate student, and invaluable during graduate school for my personal growth. Their understanding during my surgery and recovery was much appreciated. I would also like to thank the staff in Chemistry and Chemical Engineering department as well as the Mechanical and Aerospace department for their support. Thank you to Dr. Hughes Bonin for the assistance in translating the thesis abstract.

Next, I want to extend my appreciation towards the technical support teams from CMC Microsystems and SimuTech, especially Chris Donnelly, Alex Pickard, and Peter Budgell, without whom the research would have been much more difficult.

I would also like to acknowledge Defence Research and Development Canada (DRDC), CANDU Owners Group (COG), and Natural Science and Engineering Research Council of Canada (NSERC) for their financial aid in allowing me to pursue my graduate studies.

Finally, I thank God, my loving family and friends, in particular to Jamie, Jason, and Joseph for their immense encouragement, stress-relief, and support during my time at RMC.

1. Introduction

Many forms of energy generation involve the use of turbines to produce electricity, but the means to create a fluid to spin the turbines vary with each source of energy. The burning of fossil fuel to create steam that enters the turbines has been most prevalent since the Industrial Revolution, but it has also been detrimental for the environment. The increase in economic output and standard of living was at the cost of air, water and other environmental pollution [1]. The post-World War II era saw a decline in colonialism, an increase in many countries' independence, and the spread of the Industrial Revolution among third world countries. In fact, since the 1970s, there has been a clear correlation between global population, economic development, and energy demands as shown in Figure 1 [2].

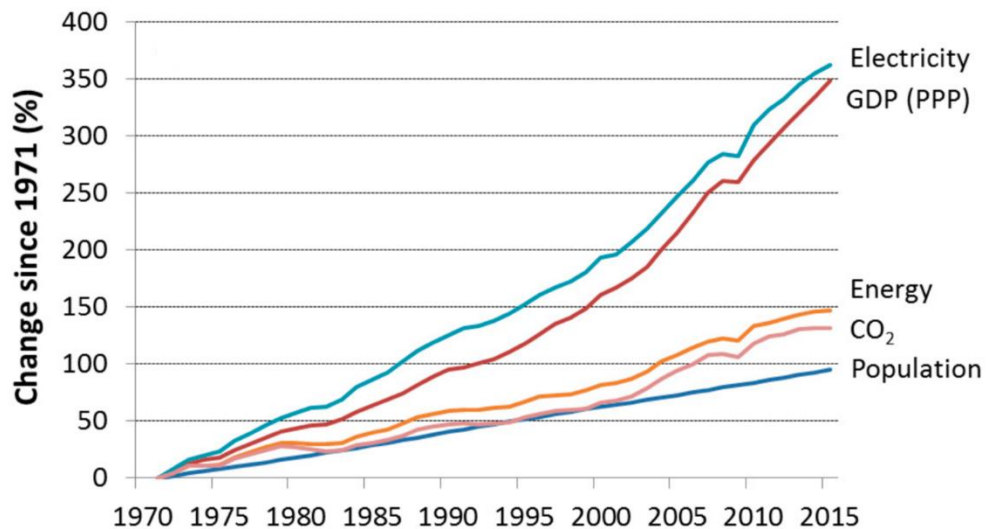


Figure 1: Percent increase in global energy demand, population, and GDP [2].

While the trends are the same, electricity demands are far out-pacing global demographic changes and the rates of increase are poised to remain steady for the foreseeable future.

To reduce growing environmental impacts, sources of clean energy have been explored such as solar, wind, and water, but nuclear power has been proven to be reliable and sustainable. Though common types of reactor design are Light Water Reactors and Boiling Water Reactors, the CANDU reactor is one of the few Pressurized Heavy Water Reactors [3]. In total, there are 31 CANDU power

reactors in operation around the world with 19 in Canada, 1 in Argentina and Pakistan, 2 in China, India, and Romania and 4 in South Korea [4]. In fact, nuclear energy is most prevalent in Ontario using the Canadian designed and manufactured CANDU reactors. There are also other reactor types used for academic and research purposes, such as the SLOWPOKE-2 reactor and the ZED-2 reactor. Since 2016, nuclear power met the demands of over 60% of all of Ontario’s energy needs. Table 1 illustrates the electricity output for different sources of power production in Ontario from 2016 to 2018.

Table 1: Electricity generated by source in Ontario from 2016 to 2018 [5].

Year	Nuclear	Hydro	Gas/Oil	Wind	Biofuel	Solar
2018	90.1 TWh	36.2 TWh	9.6 TWh	10.7 TWh	0.4 TWh	0.6 TWh
	61%	25%	6%	7%	<1%	<1%
2017	90.6 TWh	37.7 TWh	5.9 TWh	9.2 TWh	0.4 TWh	0.5 TWh
	63%	26%	4%	6%	<1%	<1%
2016	91.7 TWh	35.7 TWh	12.7 TWh	9.3 TWh	0.49 TWh	0.46 TWh
	61%	24%	9%	6%	<1%	<1%

Despite being one of the few reactor types to incorporate heavy water and natural uranium as fuel, the CANDU reactors have unique capabilities, such as on-powered refueling, defence-in-depth safety systems, and fuel bundle design that distinguishes itself from other reactors. Section 2 will focus on reactor operations and the fuel bundle design.

2. Background

2.1 Reactor Operation

Nuclear power is similar to a natural gas or fossil fuel plant where water is heated to produce steam which is passed through turbines. However, the process of steam generation is performed by nuclear fission. The CANDU reactor is the only reactor type used in Canada. A CANDU fuel bundle consists of 37 fuel rods, 48 cm in length, with each rod containing about 30 uranium pellets that undergo fission reactions [6]. One of the many benefits of CANDU is that the fuel consists of natural Uranium with fissile content of about 0.71% Uranium-235. Utilizing natural Uranium removes the costly step of enriching the fuel [7]. 12-13 bundles fit inside a horizontal pressure tube (PT) which are placed in the reactor core as illustrated in Figure 2. The reactor core or calandria consists of 380 to 480 pressure tubes depending on the reactor type, such as the CANDU 6 or CANDU 9 reactors respectively [7]. The horizontal configuration of the PT and bundle fuel design allows for on-powered refuelling unique to the CANDU reactor.

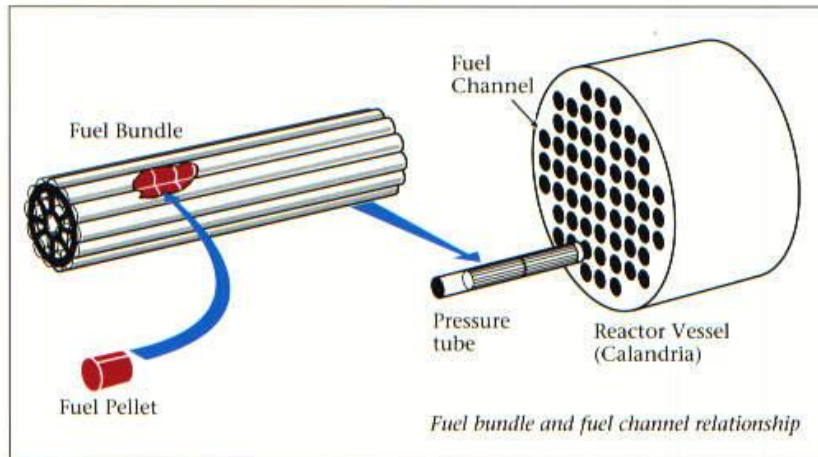


Figure 2: Pellets, rods, and bundles in the reactor core [8].

The heavy water coolant travels through the bundles to absorb the heat from the fission reactions within the pressure tube at a pressure of 10 MPa [9]. The coolant flows in the channel at a rate of about 24 kg/s with an outlet temperature of 310 °C. The PT is also held inside a calandria tube separated by an annulus spacer that holds the annulus gas. CO₂ gas flows in the annulus and serves as a leak test for

any fuel defects [10]. The bundle, PT, and calandria tube configuration is shown in Figure 3.

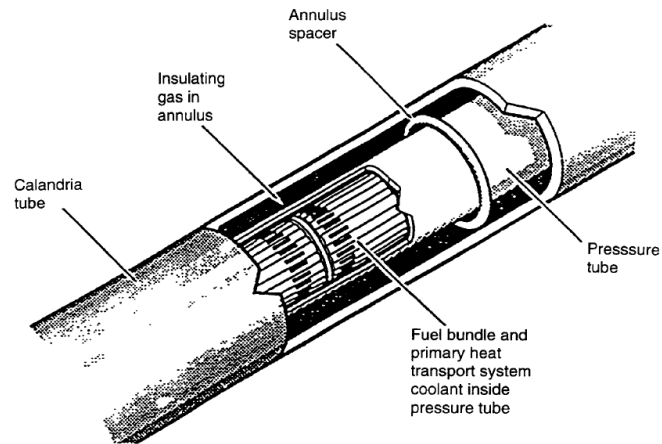


Figure 3: Bundle inside fuel channel and calandria tube [10].

The coolant then travels through a heat exchanger to transfer the heat to a secondary circuit. The secondary circuit serves as a traditional power plant and as a steam cycle. The heat exchanger is the heat input to the secondary circuit that boils light water which is then fed into the turbine. The mechanical energy of the turbine generates electricity while being cooled by an external body of water. The simplified schematic of CANDU reactor operations is shown in Figure 4.

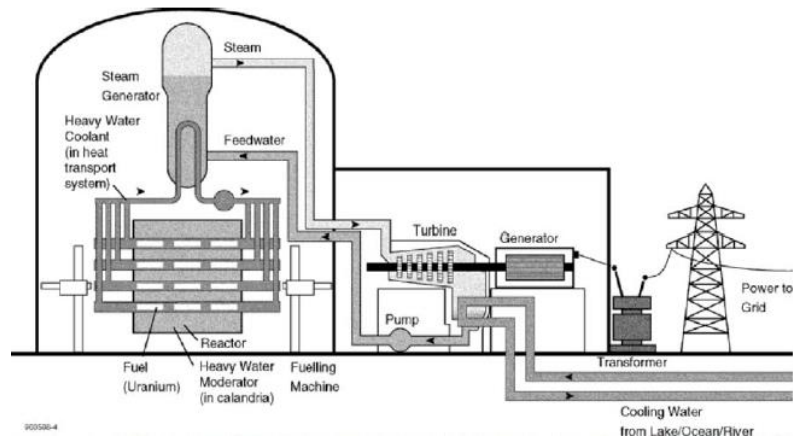


Figure 4: Simplified CANDU reactor operations [8].

2.2 Fuel Channel Components

The CANDU 37-element fuel bundle sitting within the pressure tube is the assembly under investigation. Each of the 37 elements or rods contain 30 Uranium Dioxide pellets that undergo fission reactions, and the sheath interior is coated with CANLUB, which is a graphite coating to mitigate stress corrosion cracking (SCC). The remaining void within the rods are backed filled with helium as a leak detector [11]. The rods are sealed with endcaps on each end that are resistance welded, and all the rods are joined to two endplates that hold the bundle structurally while providing clearance for coolant flow [12]. Figure 5 reveals the configuration of all 37 fuel elements and their numbering. The same numbering system is used in the current thesis.

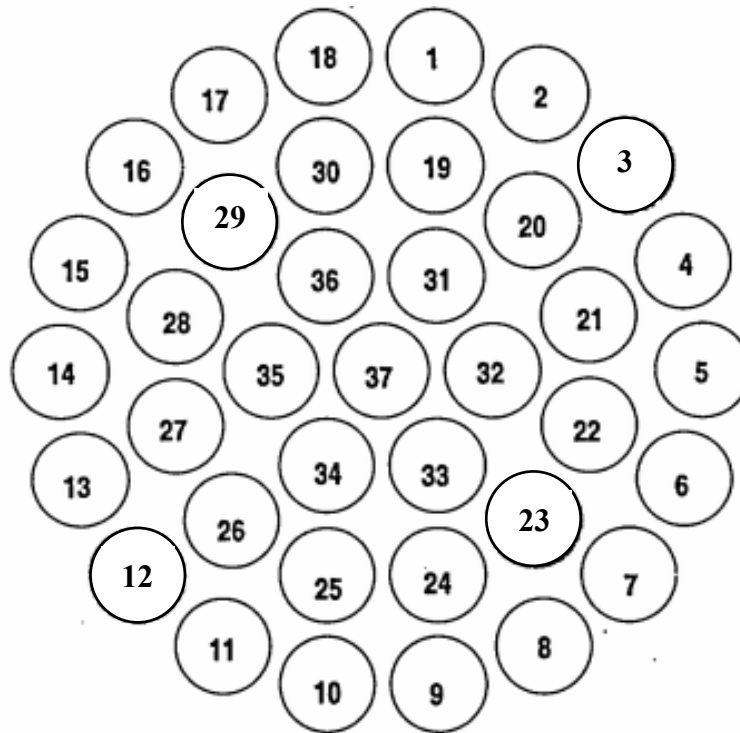


Figure 5: CANDU 37 element fuel bundle numbering (edited) [13].

Small appendages are brazed on the outside surface of the rods for different purposes. The outermost ring of rods has bearing pads (BP) on the outer surface to prevent the hot sheaths from directly contacting the pressure tube. Sheath to PT contact restricts the sheath surface to coolant heat transfer and can lead to sheath failure. All rods have spacer pads (SP) to prevent rod to rod contact. These

appendages are labeled on the rods in Figure 6. The sub-division of the fuel elements permits not only greater surface area for heat transfer, but more sub-channels for coolant to travel through.

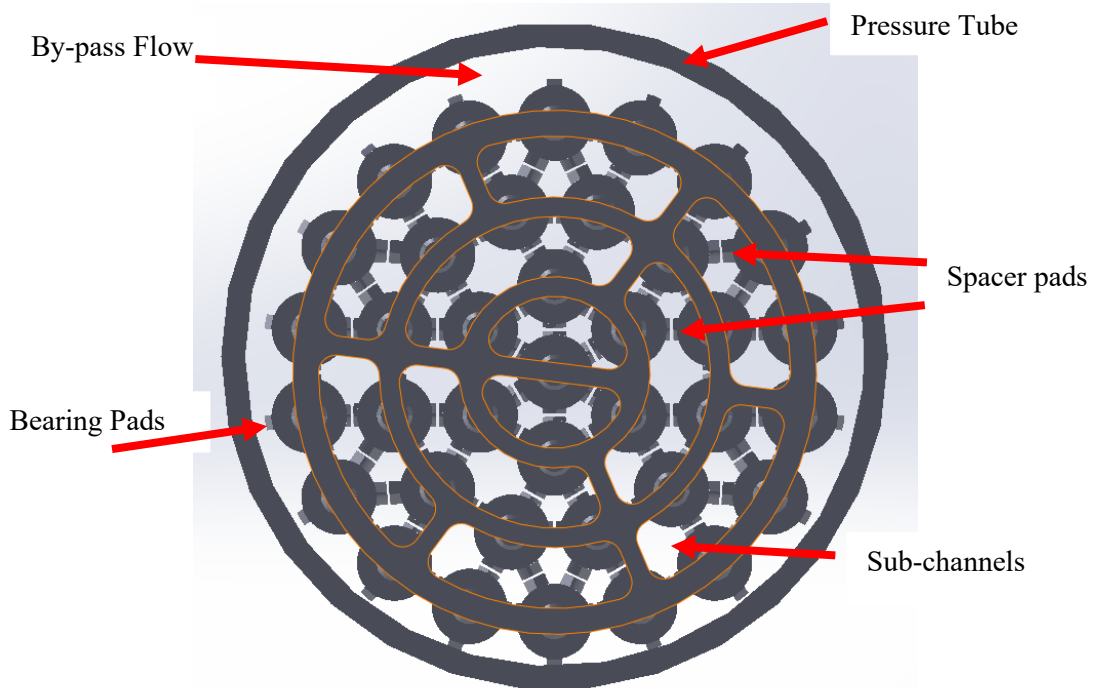


Figure 6: Location of bearing pads, spacer pads, sub-channel flow.

All bundle components are formed from a Zirconium alloy material, Zircaloy-4 (Zr-4), and offer several advantages. First Zr-4 allows for excellent neutron economy due to their small absorption cross section, which is important for a natural Uranium fuel [7]. Next, suitable mechanical properties provide robust mechanical protection while still being thin enough to collapse onto the pellets due to the coolant pressure. Thin, collapsible sheaths allow for better neutron economy and heat transfer between the pellet and coolant. Finally, Zr-4's chemical properties allow for a high corrosion resistance [7].

There are two different 37-element fuel bundle designs depending on the reactor types. The design differences are highlighted in Figures 7 and 8. The two bundles are distinguished by their endplate design, centre rod diameter, and configuration of the bearing pads whether they are in-line or staggered.

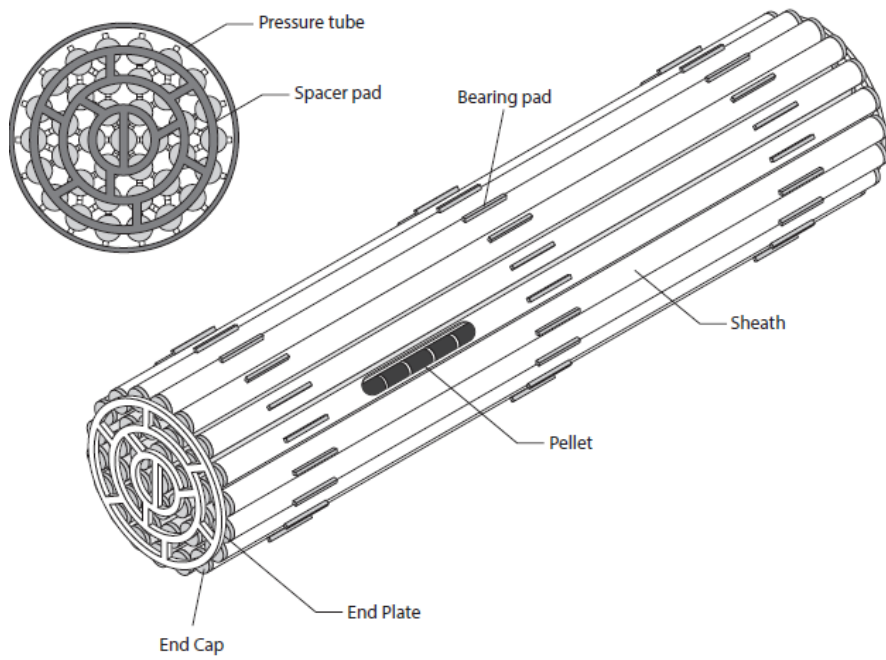


Figure 7: CANDU 6 bundle design [7].

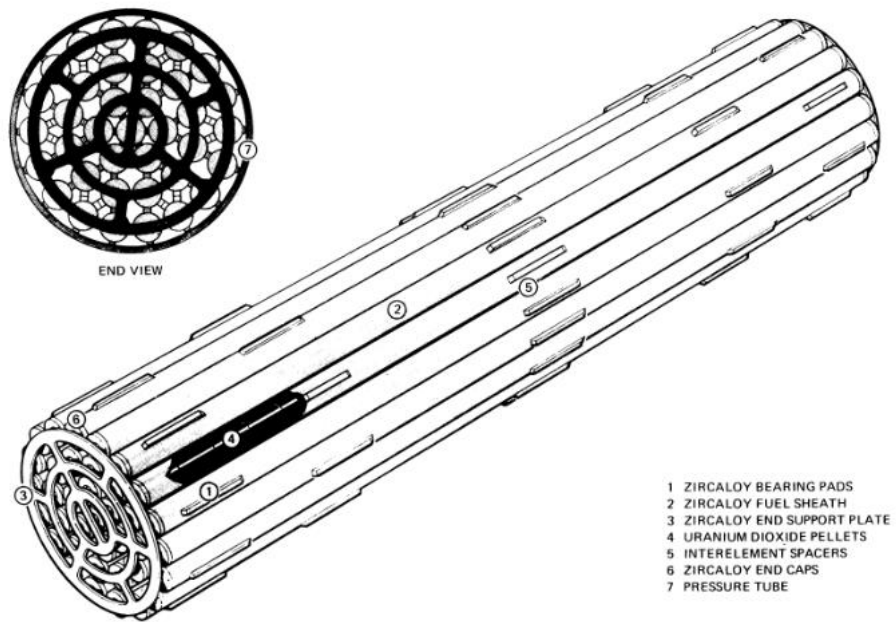


Figure 8: Bruce/Darlington plant bundle design [14].

The work in the thesis is based upon the staggered bearing pad design of the Bruce/Darlington plant with a modified endplate to reflect the experimental work from previous research efforts.

The pressure tube plays a critical role in housing all the fuel bundles and supporting coolant flow to remove the heat. At approximately 6 m long and only 4 mm thick, the pressure tube must have the mechanical properties to withstand the weight of the fuel and coolant, the flow induced vibration, seismic load, and loads from the fueling machine and end fitting bearings [10]. Chemical properties are also a consideration due to the corrosion from the alkaline coolant and creep growth. While the original material of choice was Zircaloy-2, Zirconium with 2.5% Niobium content was selected to meet the mechanical and chemical requirements in a reactor environment [9]. The Zr-Nb alloys are cold-rolled for service in the CANDU-6 and CANDU-9 reactors.

2.3 Bundle Deformation and Aging

Over time, the bundles and pressure tubes can deform which could potentially affect the performance and safety of the reactor. The pressure tube is susceptible to creep and the bundle is prone to sagging due to gravity and different operating conditions such as high temperatures and intense radiation. Creep is defined as permanent deformation that occurs over a long duration due to loads such as gravity, irradiation and is augmented by high temperatures. The high temperatures, irradiation, and gravity over the lifetime of the reactor result in diametral creep and sag of the pressure tube. In fact, the pressure tube can creep up to 6% of its original diameter [15]. This creates an opening on the top of the bundle as it sits horizontally in the pressure tube. More flow by-passes through this top opening rather than via the bundle's sub-channels, resulting in lower cooling through the actual bundle. Figure 9 illustrates this phenomenon of by-pass flow.

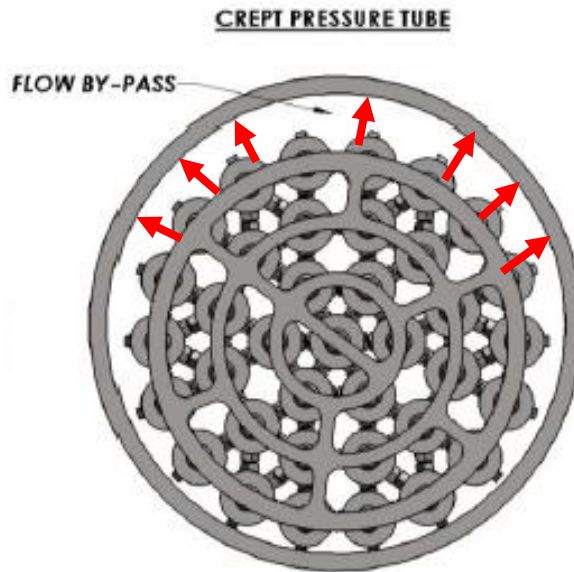


Figure 9: By-pass flow in a crept PT with red arrows showing the diametral creep of the PT (edited) [15].

Not only does by-pass flow affect a single channel, diametral creep causes a redistribution of flow in the entire core [16]. Neutron flux is greater in the central region of the core, and the central channels experience greater PT creep. As a result, more flow is redirected from the outer channels to the middle of the core.

In addition to PT diametral creep, reactor aging can create other issues. First, the pressure tube could also sag and elongate due to creep as illustrated in Figure 10.

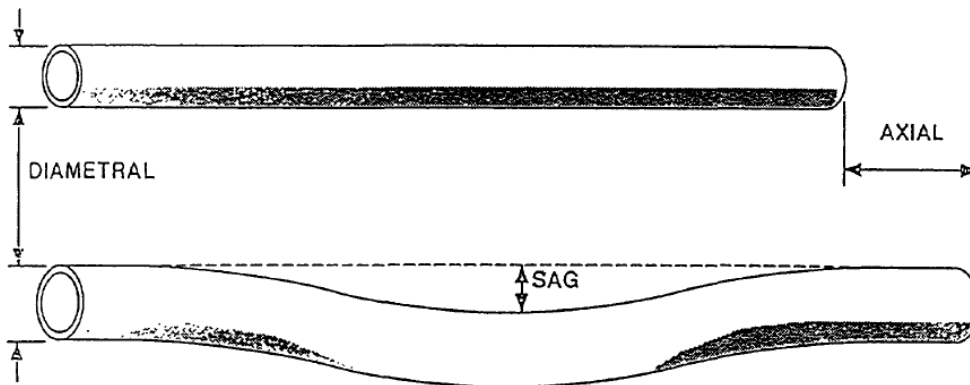


Figure 10: Effects of creep on pressure tubes [10].

The creep effects cause these permanent deformations and elongations, which changes the dimensions and material properties over time. As a result, the pressure tubes are rated for about 30 years of operation before the need to be refurbished [10]. Feeder corrosion and increase in roughness could result in a decrease in heat transfer and flowrate between the pressure tube inlet and outlet[17]. Consequently, this would reduce the dryout margin or loss of sheath and coolant contact. Other effects of aging include fouling of other tubes and piping, such as the boiler and preheater and the electrical components degradation.

The same reactor environment also influences the bundle as well. Thermal bowing of the fuel rods is another phenomenon that could reduce coolant flow through the bundle and heat transfer between the pellet and heavy water. The definition of thermal bowing is the lateral deflection of the fuel rod, and maximum bowing is the peak between the constrained ends. The main cause of thermal bowing is the differential cooling of the rods creating a temperature gradient. This leads to the rods bowing towards the hotter surface to relieve the axial strain [18]. The differential cooling can be attributed to the non-uniform heat transfer causing varying heat transfer coefficients, variations in sub-channel area and bundle geometry, and non-uniform pellet heat generation due to a neutron flux gradient. The two biggest concerns due to thermal bowing are the reduction in sub-channel area and the fuel elements in contact with the pressure tube. Sub-channel area reduction could lead to localized overheating of some rods and promote fuel defects due to the coolant starvation. Fuel bundle contact requires greater force for bundle shifting and during refueling [19].

2.4 Heat Transfer Mechanisms

When the coolant travels through the sub-channels, there are two mechanisms for heat transfer between the pellets and the heavy water. The first mechanism is by nucleate bubbles which form on the sheath surfaces' nucleation cavities [20]. Another method is by forced convective heat transfer between the sheath surface and the heavy water. Heat transfer for both methods largely depends on mass flow rate, temperature difference, heat transfer coefficient, turbulence, and the hydraulic diameter.

However, due to the compounded effects of PT diametral creep, by-pass flow, and rod deformations, reductions in sub-channel area will inevitably affect the mass flow rate of the coolant through the fuel. Even though the coolant might enter the sub-channel as a saturated single-phase liquid, the coolant could exit the outlet as a single phase vapor due to boiling. Figure 11 highlights different flow regimes as a measure of quality along a heated horizontal tube.

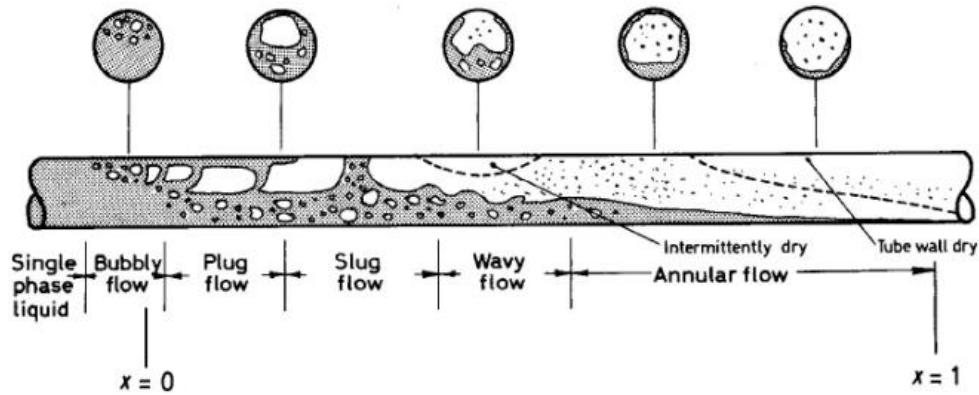


Figure 11: Horizontal flow pattern with changing quality in heated tube [7].

Bubbly flow can also be classified as the start of nucleate boiling or bubbling. As less and less liquid progresses along the channel, more bubbles are formed until they combine into voids. However, bubbles are more effective in removing heat from the surface, and once all the bubbles on the surface coalesce, this creates a film on the rod. This is classified as Departure from Nucleate Boiling (DNB). At regions on the rod beyond DNB, there is no more liquid contact with the surface and the coolant becomes a single-phase vapor. This lack of liquid contact with the sheath can lead to dryout conditions, localized overheating of the rods, and potentially fuel defects.

2.5 Safety Analysis Techniques

Several regulations are in place to ensure the safety of operation, the public, and the environment. To account for the diametral expansion and risk of fuel rupture, different manufacturing considerations and operation limits are set for safety. In terms of manufacturing, CSA-Z299 and N285.2 QA standards for Class 1 components are used for the PT and bundle parts [10]. For operation, regulatory document G144 outlines different trip parameters for reactor shutdown to maintain fuel integrity. The Canadian Nuclear Safety Commission (CNSC) provides several trip criteria to stop operation if the undesirable conditions are met. These limits include a maximum fuel sheath temperature for 60 seconds [21]. Finally, there is a 4% to 5% diametral creep limit depending on the operator, with the former limits implemented by Korean operators and the latter used by Canadian power stations [10]. To obtain diametral measurements for the PT and channels, the Channel Inspection and Gauging Apparatus for Reactors (CIGAR) are used. However, the drawbacks of the system include shutting down the reactor and emptying the fuel channels which are both lengthy and costly. Simulation and empirical correlation

that could predict bundle and PT aging behaviour would help alleviate the economic and operational costs.

3. State of the Art

Simulations and experimental testing are indispensable procedures for many researchers, but they are especially beneficial in the nuclear realm. Nuclear power plants require special expertise and skill to operate, which makes it costly with regards to development and safety if accidents do occur. Thus, the need for modelling techniques and out-reactor testing arises, which are both more economical and safer than an in-reactor test. The challenge comes in trying to recreate reactor operating and accident conditions due to the sheer complexity of a nuclear environment. The three-dimensional nature of the design, the non-linearity of the constitutive laws due to creep and plasticity, as well as the coupling effects of multiple natural phenomena add to the difficulty of capturing in-reactor conditions [22]. Different codes have been developed to investigate the structural, thermal and heat transfer properties of a fuel element and bundle. In addition, multiphysics tools have been employed to couple different effects together. However, in all stages of the analysis and simulation, assumptions must be made to simplify the model [22]. Even with many assumptions and simplifications, large computing resources must be allocated. Despite the advantages of computer modelling, the results are meaningless without proper experimental data to validate and ensure that both the computational and experimental data align. As such, validation can be seen as the quality assurance component when developing and using simulations [23]. Experimental works including bundle heat up tests and Post Irradiation Examinations (PIE), are used to study the profilometry and deformations of spent and used bundles. Codes representing fuel elements as well as models for 3D structural analysis and Computational Fluid Dynamics (CFD) along with experimental work are discussed in this Chapter.

3.1 Fuel codes

Before the advent of sophisticated 3D multiphysics modelling software, fuel codes were developed to study the performance of a single fuel element. Fuel rods encase radioactive by-products and are the first and second layers of defense against any defects. Consequently, their performance and structural strength are essential for operation and safety. The first of these codes is ELESTRES, which is used to determine the impact of different parameters such as pellet density, surface roughness, shape, and length on fuel performance [24]. In addition, the code can also predict stresses and strain near circumferential ridges and welds, determine sheath temperature during refueling, and the probability of failure over multiple

power ramps [24]. Extensive validation work was conducted at the experimental reactor in Chalk River mainly for irradiation, and in other power stations in Ontario.

Another widely used industry toolset is the BOW code. Several iterations have been made since its original debut, yet the fundamental function of the code is to determine the lateral bowing of tubes due to a temperature difference, as is the case in fuel bundles [25]. In essence, the code models the deflection and bow of a tube or a tube array under hydraulic loads, gravity, and thermal gradients. Furthermore, the code has also been tailored for nuclear specific applications by adding 2D contact with adjacent sheaths. BOW also considers boundary conditions at the endplates, rod and pellet stiffness, sheath/fuel interactions, and pellet cracking [25]. Neutron flux and thermal gradients determine how the pellets bend and are calculated by Bessel functions. Local pellet bending and their effects are captured by a Curvature Transfer Factor (CTF) which describes the imprint of the pellet's bend on the sheath walls. The rod's bending is comprised of the combination of all the pellet's CTFs and the rod's own material response to load conditions. Validation efforts were conducted at Whiteshell Nuclear Research Establishment and Chalk River Nuclear Laboratories. Verification was also carried by theoretical bending equations [25]. However, similar to the codes previously mentioned, these codes cannot model three dimensional deformations and interactions within an entire bundle. Although BOW provides an in-depth and comprehensive analysis of a single fuel rod, there is limited consideration of creep and a lack of fluid dynamics analysis.

3.2 3D Mechanical Models and Experiments

Contrary to fuel codes, multiphysics toolsets allow the user to model the fuel bundle in three dimensions and can provide a macroscopic view of the interaction between various phenomena. As a result, commercial finite element codes such as, COMSOL, ABAQUS, and ANSYS are widely used in industry and research.

For example, a team at the Korea Atomic Energy Research Institute used ABAQUS to study and compare the static strengths of a CANFLEX and the current 37-element bundles. More specifically, a string of 13 fuel bundles under axial hydraulic loads during refuelling conditions were investigated to see the effect of the end plates, the flow rate, and the axial loading on the bundle strength. To simplify the analysis, the end plates were represented by shell elements, the fuel rods by beam elements, and the spacers by truss elements [26]. The pressure tube and bearing pads were neglected, but were assumed as boundary conditions. The

hydraulic load was distributed over the 13 bundles, so the force was represented as a force per length of each fuel rod. It was discovered that the end plate design of the CANFLEX bundle reduced the maximum stress and displacement due to ribs in the end plate. Moreover, the CANFLEX bundle has a higher threshold of plastic deformation due to hydraulic drag compared to the 37 element bundle - 9200N compared to 7300N [26].

Another team studied the effects of hydraulic drag on the 37-element CANDU and CANFLEX fuel bundles, but for different refuelling conditions. Unique to the CANDU reactors is its ability to refuel while in operation. During refuelling, a side stop prevents bundles from sliding out of the pressure tube and thus, the bundles must resist the compressive forces of the hydraulic drag and side stop. Roman *et al.*, from Romania, used ANSYS to study displacements and stresses while one and two refueling side stops support the last bundle [26]. Similarly, the end plates were modelled as shell elements, but the team used pipe elements for sheaths, link elements for spacers, and contact elements for the side stops. With regards to the boundary conditions, the last bundle's 8 outer sheaths were constrained in the axial direction and the remaining bundles had 1 node on the endplate constrained transversely. The hydraulic load was distributed uniformly on all sheaths, but 7300 N was used for the 37 rod CANDU bundle and 6300 N for the CANFLEX. Bearing pad to pressure tube contact, fuel rod bowing, and endcap to plate welds were neglected for the analysis. Roman *et al.* found similar stresses on the endplate despite the difference in hydraulic loading, and difference in radial deflection were only 0.3 mm for one side stop and 0.1 mm for two side stops. Both bundles were concluded to be able to withstand the hydraulic drag during refuelling conditions.

Rather than relying on previously mentioned fuel codes to model the thermomechanical fuel behaviour, Krasnaj used ANSYS to model the coupled thermal-mechanical effects [27]. The coupling was achieved by modelling a comprehensive fuel rod with uranium dioxide pellets inside represented as both a monolithic element and as individual pellets. Pellet to pellet contact was set to allow for local heat transfer as well as with the sheath walls. Internal heat generation was applied to the pellets with a linear power rating of 50 kW/m and coolant temperature set to 573 K. Regarding the structural analysis, axial symmetry was used to reduce the number of nodes. Finally, the coolant pressure, coolant temperature, and sheath/coolant convective heat transfer were applied. With the pellets inside the sheath, the flexural rigidity of the fuel element was also estimated through simulations. The monolithic pellet, individual pellet, and cracked pellets were studied. It was found that the individual pellet model was a lower limit for flexural rigidity while the cracked fuel model provided the upper limit [27].

However, the deflections were similar for all fuel representations when operating loads were applied, and brazed appendages played a significant factor in deflection behaviour.

The closest simulation to a comprehensive full bundle structural analysis was performed by Walters and Williams from AECL where ANSYS was used to model a full CANFLEX bundle with contact. The focus was placed on the interaction between fuel pellets, rods, and endplates. Thus, the pressure tube was modelled as a non-deforming boundary condition [8]. Further assumptions include neglecting thermohydraulic and irradiation effects inside the fuel rods. The fuel pellets were assumed as a single monolithic solid element to assume no thermal resistance. Fuel to sheath contact and spacer to spacer contact were assigned as frictional with a friction coefficient of 0.2 and 0.1 respectively. A Computational Fluid Dynamics analysis was not performed, but rather, the temperature profile was assigned, and thermal deformations were derived from the temperature distribution. A gradient of 300°C to 900°C was applied from bottom to the top element to represent accident conditions with coolant flowing in the bottom portion, but with steam filling at the top. The authors noticed endplate deformation due to this temperature gradient causing different rates of thermal expansion. In addition, thermal bowing occurred for the fuel elements. A single fuel element was tested against experimental data using a tungsten heater to simulate rod bowing. The monolithic pellet assumption was believed to be the cause of slight differences with computer models and found that the individual pellets would need to be represented. However, the work lacks consideration of bearing pad to pressure tube contact, the inclusion of creep or CFD.

The current work expands on the validation work conducted by Lt. Soni with her research on the 37-element CANDU fuel bundle deformation. Her work consisted of modelling and validating the deformations of a 3D fuel bundle with the experimental work done by the Canadian Nuclear Laboratories [28]. A partial 12 rod bundle was created in ANSYS with the inclusion of thermal loading, and creep. The boundary conditions and loads were set to align with operating conditions of an out-reactor test. This model includes a temperature gradient from 930 K to 1133 K axially along the bundle as recorded by sheath thermocouples, and creep for 400 s [28]. Just as the experimental bundle sat in a non-deforming, rigid quartz pressure tube, the finite element analysis (FEA) model also has the same pressure tube to act as the radial boundary condition. The bundle is fixed at one endplate and free to expand axially. Due to computing limitations, the model was limited to 12 rods. When compared with experimental results, the predicted deformations showed good agreement regarding the outer elements, but the radial deflection for

the inner elements slightly differed from the experiment [28]. The author lists the discrepancies being a result of modelling assumptions, the need for multiple experimental tests, and only including 12 rods. However, agreement with actual experiments allowed the current work to build upon Lt. Soni's model, by adding more rods to complete the bundle.

3.3 3D Fluid dynamics model

The coolant that flows in the sub-channels is the main mechanism of heat transfer and the coolant flow must be studied both as a single phenomenon and coupled with the mechanical deformations. A team at Stern Laboratories investigated both single-and two-phase flow within a 37-element bundle with both a nominal pressure tube diameter and a 5.1% crept pressure tube [29]. Experiments with heated rods in a water loop were used to validate the CFD results. Two loops were created to simulate reactor operations with a test loop containing the bundle and a secondary loop for coolant heat transfer representing a steam generator. Ceramic liners were used to mimic a variable diameter pressure tube, and the rods were electrically heated with a temperature gradient. The instrumentations used were differential pressure transducers, absolute pressure transducers, resistance temperature detectors and internal thermocouples in the fuel rods. For the CFD model, a Reynolds Averaged Navier-Stokes method and the conjugate heat transfer model were used in conjunction with ANSYS [29].

CFD and experimental research were also performed to determine which CFD turbulence model aligned well with turbulent flow in a CANFLEX bundle. The three turbulence methods studied were the Large Eddy Simulation, Detached Eddy Simulation, and Reynolds Stress Model which are more comprehensive than the unsteady Reynolds Averaged Navier-Stokes method [30]. The physical model consisted of a water circuit with a variable speed centrifugal pump, stainless steel bundles, flow meter, and Dytran [30]. For the CFD model, the meshes were divided into upstream, bundle, and downstream segments to overcome complications in meshing the full bundle. Instantaneous and time-averaged pressures, flow rates, and hydraulic forces were compared with the experimental data. For both the model and experiment, the thermal analysis and irradiation effects were neglected. There was a good match among all three models, yet the LES method provided better comparisons regarding the instantaneous flow results [30]. In addition, the LES method more accurately captured the anisotropic turbulence that creates flow circulation between the fuel rods.

The closest coupling analysis between structural and fluid effects was performed by Piro *et al.*, when the team studied the bypass flow due to a crept pressure tube housing an as-fabricated 37 element CANDU bundle. Again, the computational results were compared with experimental work. The instrumentation of choice was the Magnetic Resonance Velocimetry (MRV) to measure the flow rate, which is a non-invasive method and the fluid does not have to be visible [15]. Light water was used as the coolant but with a copper sulfate agent for the MRV to detect. The added agent did not affect the flow significantly. The water was kept at 20.5 °C, with a flowrate of 60 L/min and the pressure tube creep up to 6% diametrically [15]. As for the CFD model, HYDRA-TH was the selected CFD code and the Large Eddy Simulation was the method as selected by other teams. Again, for both tests, there were no thermal considerations. It was seen that computational and experimental results match qualitatively up to 10 mm and 50 mm downstream from an endplate. The flow rate started to deviate towards the top of the bundle around 50 mm downstream, and the bypass flow fully occurs between 250 mm and 400 mm [15]. In total, the team found roughly 30% of the flow by-passed the bundle.

Thus, when completing the literature review, the gaps in the field of research become evident both in terms of isolated fluid and structural analyses, and also coupled analyses. A full bundle contact analysis considering interactions between fuel elements and with the pressure tube is missing, as well as a fluid dynamics model of a deformed bundle. Finally, pressure tube diametral creep must be incorporated once the different multiphysics effects are considered. The current work hopes to fill in that gap using the finite element method to perform the structural analysis to simulate the interaction between a deformed 37-element fuel bundle and a crept pressure tube. In the future, this model could incorporate the fluid aspect of a 37-element CANDU fuel bundle.

3.4 Experimental Studies

In addition to simulations, bundle heat up tests and Post Irradiation Examinations (PIE) were conducted to study new profiling techniques, observe bundle deformation, and measure bundle sag for different bundle test cases.

The first studies were undertaken by Dennier *et al.*, on bundles from both out-reactor and in-reactor tests at Sheridan Park Engineering Laboratories (SPEL) and Whiteshell Laboratories [31]. Out-reactor observations were performed using a Coordinate Measuring Machine on 16 bundles after a 40 day zero-power endurance test from Darlington unit 3. The CMM is essentially a probe linked to a computer that provides measurements on element bowing and length, endplate dishing, and

BP height for non-irradiated bundles. Figures 12 and 13 highlight the vertical deformation profiles of the outer elements along the length. Elements are labeled in the same manner in Figure 5.

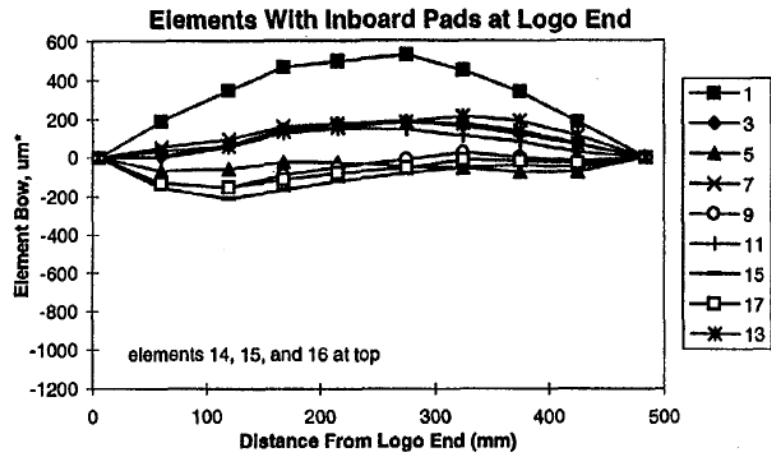


Figure 12: Odd numbered outer element vertical deflections (μm) [31].

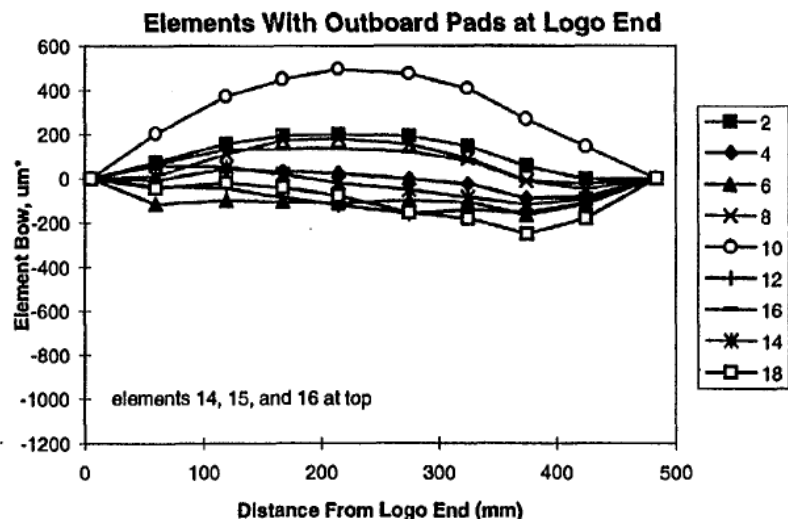


Figure 13: Even numbered outer element vertical deflections (μm) [31].

Figures 12 and 13 both generally display an ‘S’ and upside down ‘U’ deflection shape. These results are one set of benchmarks used to qualitatively compare the FE models in the current research. The researchers also discovered that the

elements welded closest to the endplate radial webs bowed the most, which could be attributed to the endplate dishing by the coolant hydraulic drag.

Irradiated bundles were profiled using a Linear Variable Displacement Transducer on three bundles from Bruce Unit 8 channel S22. In addition to studying element vertical profiles, irradiated bundles were also used to study the effects of endplate cracking and PT fretting. Investigating the fret marks required keeping the bundle intact to prevent the results from being skewed when the bundle was dismantled. Irradiation creep was found to cause a 'W' shape deflection of the top elements with the SP preventing sagging at the midplane. The researchers determined that the deflection profiles remained similar between the out-reactor and in-reactor bundles. Both tests showed instances of the rods sagging into a 'S' shape deflection, and endplate dishing playing an important role in element bowing near endplate webs. The sag of both bundles were also between 175 and 275 μm [31]. Finally, the examiners concluded the profiles from the PIE and out-reactor test were comparable.

PIE studies were also performed to determine the effects of CANLUB on fuel performance. Two CANDU-6 bundles were specially made and included select elements without the inner CANLUB coating. The bundles were then irradiated at Point Lepreau station in channels K08 and M15 achieving bundle-average burn ups of 199-202 MWh/kgU and linear powers of 47-48 kW/m for the outer elements [13]. PIE at Whiteshell consisted of visual examinations of the bundle and elements, profilometry of bundle and elements, fission gas analysis, and ceramographic and metallographic examinations. The radial bow of the outer elements was studied for both channels and is shown in Figure 14.

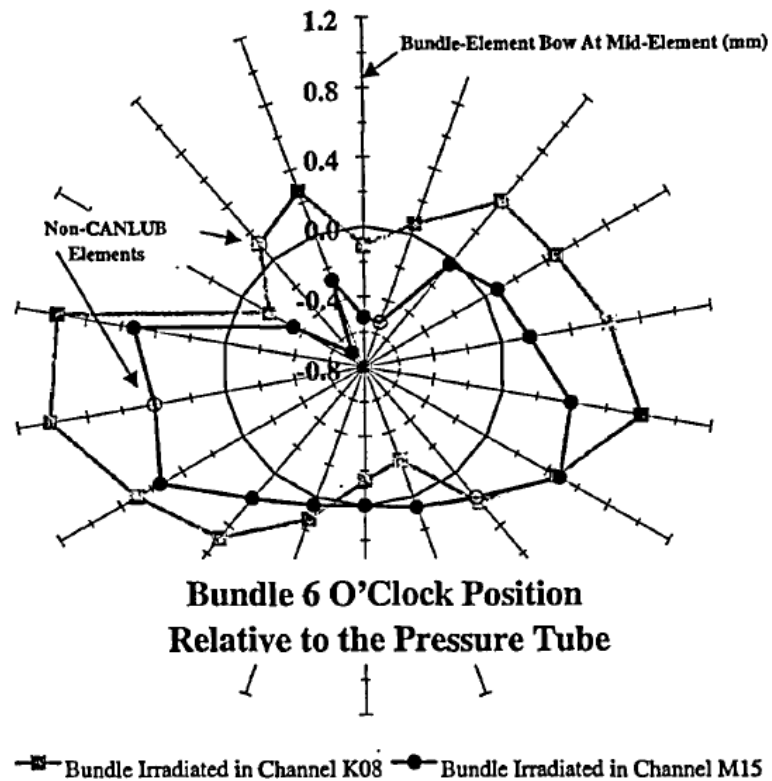


Figure 14: Outer element radial bow (mm) for both channels [13].

The two outlines show both channel locations and the outer element profiles were recorded using a dual transducer profilometer. The 2 bundles generally share the same deformation profile as the lower and side outer elements bow outwards to fit the contours of the pressure tube. The top elements also sag downwards with the lower elements displaying a ‘W’ shape deflection [13]. Along with the side profiles from Figures 12 and 13, profilometry results from Figure 14 were also used to qualitatively benchmark the results from the FE bundle model in the current work. The examiners also discovered little impact on fuel performance from using CANLUB. Centreline temperature, Fission Gas Release (FGR), and UO_2 grain growth were comparable between CANLUB and non-CANLUB elements, and sheath strain differences were caused by diametral differences due to the lack of a coating layer [13]. CANLUB offered protection against stress corrosion cracking while maintaining similar levels of fuel performance.

Another PIE was performed to study the irradiated bundle geometry using a modified spreadsheet software EXCLACS (Excel Looking A lot like CADDs) as part of a CANDU Owners Group (COG) project. The bundle was loaded into Bruce Unit 7 channel H07 for more than two years in an uncrept pressure tube. Power ratings achieved were 492 MWh/kgU and a peak linear power of 41 kW/m for the outer elements [32]. EXCLACS was the analytical tool that uses 2D geometries to model the rods inside the pressure tube and compares the irradiated geometry with the original geometry. Overall deformation patterns were consistent with previous PIE such that the top rods sag downwards while the lower and side elements bowed outwards to contact the pressure tube. Gravity and creep caused the lower bearing pads to contact the PT inner surface. Instances of bundle drooping was observed at the ends due to the weight of the endplate, endcaps, and rods. Initially, the endplates were vertical and parallel, but as the PT experienced sag and creep, the bundle also experienced the same sag. Aging, as well as the weight of the PT, bundle, and coolant further caused PT sag and endplate tilting. The same tilting caused the bundle to experience parallelogramming where the bundle would be slanted. Parallelogramming further caused the rods to bend into an 'S' shape with the greatest deflections occurring at the quarter plane. Finally, evidence of endplate doming was observed with the downstream endplates becoming convex while the upstream endplates becoming concave. Endplate doming was caused by the hydraulic drag of the coolant on the centre of the bundle while the outer elements are locked inside the PT.

4. Objectives of the Research

The objectives of the current research were to develop a finite element model of a complete 37-element CANDU fuel bundle without pellets and to study the effects of pressure tube diametral creep on the deformation response of the bundle. In a horizontally aligned PT and fuel bundle, diametral PT creep would affect the bypass flow of the coolant as well as the sub-channel flow. The finite element method was employed using the commercially available FE software, ANSYS, to perform a static structural, nonlinear analysis on the mechanical deformations of a complete fuel bundle. Due to the difficulty in mimicking exact reactor conditions, the intent was not to predict the deformed shape of the bundle due to in-reactor conditions. The purpose was to capture the interaction between the deformed fuel rods, and the interaction between the crept pressure tube and the deformed fuel bundle. The overall deformed shape of the fuel elements was represented based on Post Irradiation Examinations and bundle heat up experiments. The research is a continued effort that builds upon Lt. Rabia Soni's work on validating a partial 37-element bundle model with an out-reactor experiment [28]. Consequently, the material properties used in the current work were the same as in Soni's work.

The finite element analysis of the 37-element bundle required considerable computing hardware due to the many contact pairs between spacer pads and the contact between the bearing pads and the pressure tube. High-Powered Computing (HPC) hardware and software were acquired from CMC Microsystems in order to efficiently run the simulation. To simplify the model, UO_2 fuel pellets were omitted as well as heat generation from within the sheaths. The pellets were not required for obtaining the deformed shape of the fuel elements because this was achieved through careful consideration of the loading and boundary conditions within the model. Fuel performance considerations such as power ratings, burn ups, or fission gas releases were neglected as well.

The research was separated into two parts. The first step was to use a 1-rod model to determine the appropriate boundary conditions and loads needed to match the deformed shape of individual fuel elements from the PIE data. These preliminary studies are presented in Chapter 6. The next step was to create the full 37 element model based on sensitivity studies of boundary conditions and loads on the entire bundle. This model was used to simulate pressure tube diametral creep with diameters ranging from 0%, 2%, 4%, 6%, and 8%. Different section planes, such as the midplane and quarter plane, were observed to determine the effects of PT diametral creep on the bundle deformation. These full bundle models are presented in Chapter 7.

5. Theory

This section outlines two different approaches for performing structural analysis on the 37-element CANDU fuel bundle and the theory behind each method. The model must consider the loads to qualitatively match the experimental tests, and incorporate contact between the appendages. The commercially available finite element modeling software, ANSYS, was selected due to its multiphysics capabilities, Graphical User Interface (GUI), ability to model contact, and compatibility with HPC hardware and software. The solid mechanics equations were used to aid in model validation by ensuring that the deflection of individual rods prior to making contact was correct.

5.1 Solid Mechanics Equation

When considering the structural analysis of the fuel bundle rods, each fuel element could be modeled as an elastic tube or flexural member, and solid mechanics equations could be applied.

For example, if the rod is considered simply supported, the rod could be modeled as a simply supported beam with a uniformly distributed load as in Figure 15:

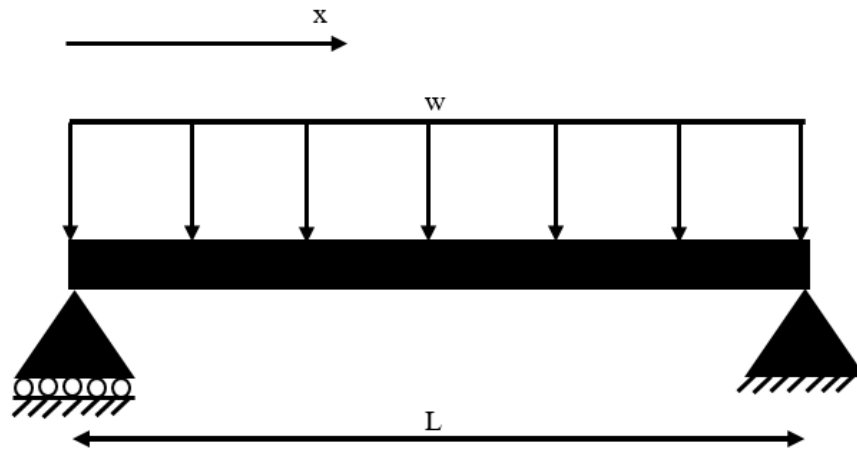


Figure 15: Simply supported beam with uniformly distributed load.

Where w is the weight per unit length, L is the length of the beam, and x is any point along the beam from the left hand end.

The shear force (V), bending moment (M) and deflections (Δ) respectively can be determined by the following equations:

$$V = w\left(\frac{L}{2} - x\right) \quad (1)$$

$$M = \frac{wx}{2}(L - x) \quad (2)$$

$$\Delta = \frac{wx}{24 EI}(L^3 - 2Lx^2 + x^3) \quad (3)$$

Where E is the modulus of elasticity of the material and I is the moment of inertia for a rod provided by:

$$I = \pi\left(\frac{D^4 - d^4}{64}\right) \quad (4)$$

with D as the outer diameter and d as the inner diameter. Thermal loading can also be applied to the structural member. The change in the length can be determined by:

$$\delta = \alpha L \Delta T \quad (5)$$

With α as the linear coefficient of thermal expansion, and ΔT as the change in temperature.

The rod could also be axially constrained at both ends which could be represented as a beam with cantilever supports at both ends as illustrated in Figure 16. While cantilever constraints also restrict radial growth, the vertical deflections are the deformations of interest.

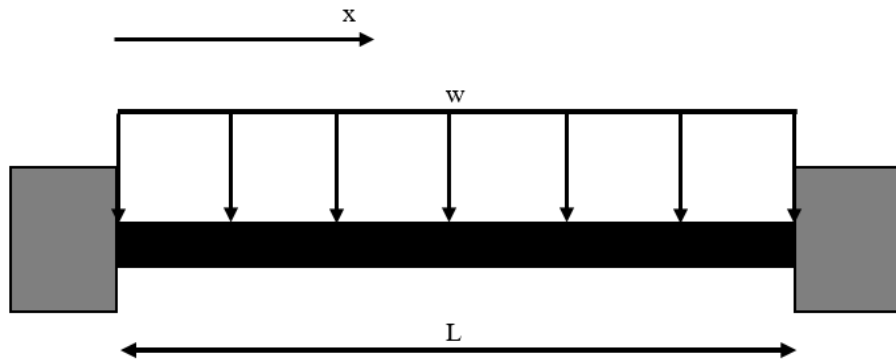


Figure 16: Both end cantilever beam with uniformly distributed load.

With the same uniformly distributed load, the shear force can be calculated by equation 1, and the bending moment (M) and deflections (Δ) respectively can be determined by:

$$M = \frac{w}{12} (6Lx - L^2 - 6x^2) \quad (6)$$

$$\Delta = \frac{wx}{24 EI} (L^3 - 2Lx^2 + x^3) \quad (7)$$

In the case of Figure 16, the end boundary conditions provide no room for expansion and any thermal loading will increase the axial force on each end determined by:

$$P = EA\alpha\Delta T \quad (8)$$

With A being the cross-sectional area of the beam or rod.

The bending moments and shear forces could be used in determining stress and strain of the member which are useful for finding critical regions of high stresses, if the structure yields, or comparing the maximum stress to a failure criteria.

Axial strain (ϵ) for a structural element can be calculated by:

$$\epsilon = \frac{\Delta L}{L_o} \quad (9)$$

where Δl is the change in length and L_o is the original length. Axial stress (σ) and strain are also related by the Young's modulus and Hooke's law as it pertains to the theory of elasticity in the elastic region:

$$\sigma = E\varepsilon \quad (10)$$

The equations for normal stress due to an axial load (σ_N) and bending moment (σ), and transverse shear stress (τ) is given by the following:

$$\sigma_N = \frac{P}{A} \quad (11)$$

$$\sigma = \frac{My}{I} \quad (12)$$

$$\tau = \frac{VQ}{It} \quad (13)$$

Where P is the axial load, y is the distance from the neutral plane, t is the thickness of the rod, and Q is the product between A', the area above or below the neutral plane and y', the distance between the neutral plane and the centroid of A' [33]. Simplifying the fuel rods as beams permits an empirical analysis and a first-estimate approach before plasticity or appendages contact.

The analytical approach may provide sufficient detail and exact solutions for a singular rod or a small cluster of fuel elements in isolation. However, the full bundle consists of 37 elements with appendages, with all the rods attached to an endcap and endplate. Unless analytical equations, correlations, and factors were developed for the bundle in a particular configuration and boundary conditions, determining the deflections and stresses for all bundle components is difficult. When stress concentrations, contact between the appendages, material plasticity, increased stiffness due to spacer and bearing pads, and torsional effects are present, solely using analytical equations becomes unfeasible. To capture all these effects, a numerical method, more specifically the finite element method, was used.

5.2 Finite Element Method

The finite element method is a numerical technique for boundary value problems expressed using partial differential equations (PDE). Boundary value problems can be defined as when one or multiple dependent variables must satisfy the differential equation within a known domain of independent variables [34].

Specific conditions on the domain boundaries must also be satisfied. The dependent variables are also called field variables, and the field represents the domain or physical geometry. Specific field variable values on the field boundaries are called boundary conditions. Depending on the phenomena under investigation, the field variable can be either displacement for structural analysis, fluid velocity for fluid dynamics, or temperature for a thermal study [35].

Finite element analysis generally follows 3 stages, preprocessing, the solution, and post-processing. The pre-processing stage involves preparing the geometry for the solver by idealizing the structure using different geometry and element types, discretizing the object into elements collectively called a mesh, and applying material properties, loads, and boundary conditions. The solution is approximate, and the accuracy depends upon the order and size of the elements chosen. Figure 17 shows the effect of meshing in capturing the geometry.

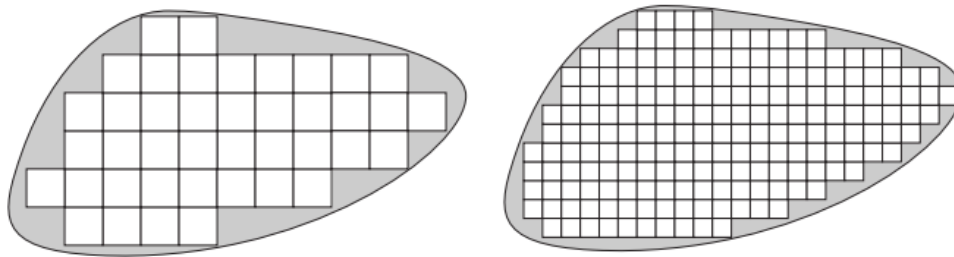


Figure 17: Effect of coarse and fine mesh in capturing geometry [34].

Though the entire domain can never be fully captured, the exact solution can be approached by discretizing the object with more elements with a smaller size. Incremental decreases in element size allows for the approximate solution to asymptotically reach the exact value [34].

FEM is based on the idea of a piecewise polynomial interpolation. Each element is joined together over the field such that the field variables are interpolated in a piecewise manner. The nodes are the locations where the field variable is directly calculated [36]. Locations between the nodes are interpolated using nodal values and shape functions that depend on the element type and the element Degrees Of Freedom (DOF). The physical geometry and the PDEs must be converted to its analogous discrete finite element form represented by a stiffness matrix. The unknown nodal variables can then be determined by the stiffness matrix with load inputs. For example, for structural analysis, the stiffness matrix encompasses the

material and geometric properties, and represents the resistance to an input force as it affects the geometry's displacement [36]. This relationship is shown by the following equation:

$$\{F\} = [K]\{u\} \quad (14)$$

Where $\{F\}$ is the external force vector, $[K]$ is the stiffness matrix comprised of the material and geometry properties, and $\{u\}$ is the field vector or displacements for structural analysis. The Galerkin Method or the Principle of Minimum Potential Energy are used to formulate the stiffness matrix for 2D and 3D geometries.

During the solution stage, the system of equations is solved for the nodal values using methods such as the Newton Raphson method. If the geometry was properly constrained, the nodal values can be calculated and values such as stresses and strains can be determined during the post processing stage.

5.4 Non-Linearity

Equation 14 describes a linear relationship between the external forces and the resulting displacement. For cases when the stiffness matrix, or the applied load, are dependent on the displacement, this is called non-linearity. The three main types of nonlinearities are geometric, material, and contact. Material non-linearity arises when the material behaves in a manner that is not elastic or exhibits a non-linear stress-strain relationship, such as plasticity, material failure, or hysteresis [37]. Geometric non-linearity occurs with large deformations or displacements such as a fishing rod being bent. Finally, the last source of non-linearity is contact between two objects. Contact will be covered in-depth in the next section.

Equation 15 shows a non-linear stiffness relationship:

$$\{F\} = [K(u)]\{u\} \quad (15)$$

Since, it is not possible to directly solve for displacement, an iterative process must be performed and the Newton Raphson method is one such method. An initial displacement is assumed and an iterative process of linear approximations is used to calculate the solution.

Let x_0 be an initial assumed displacement. Then the stiffness matrix in equation 15 can be determined by:

$$\{F\} = [K(x_0)]\{u\} \quad (16)$$

with $[K(x_0)]$ as K_0 . With F_a as the desired given load, a new displacement of x_1 can be determined with the relationship:

$$\{F_a\} = [K_0]\{x_1\} \quad (17)$$

With displacement x_1 , a new stiffness matrix K_1 is recalculated and a force, F_1 , is determined. How much the calculated force differs from the applied force is called the residual (ΔF) and is calculated by:

$$\Delta F = F_a - F_k \quad (18)$$

where F_k is the calculated force for the particular iteration. If the residual is greater than an established convergence criterion, the process repeats by determining a new stiffness matrix, displacement, then the force to calculate the residual. For ANSYS, the criteria for force convergence is the residual force must be less than 0.1% of the applied force [38]. Figure 18 provides a graphical representation of finding equilibrium for equation 15 for a non-linear structural system.

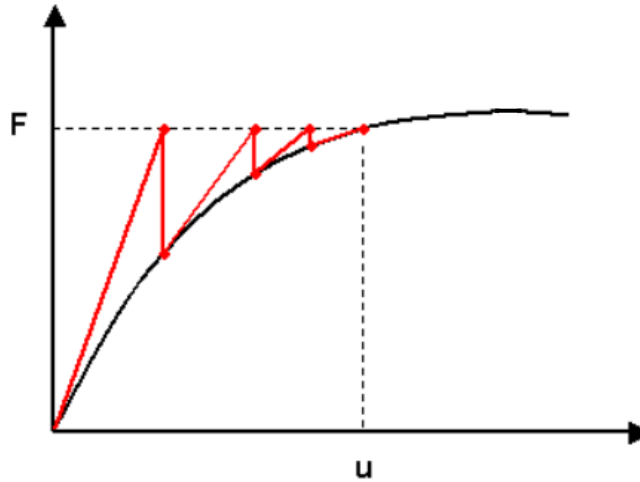


Figure 18: Newton Raphson Method [39].

5.5 Contact

Contact is one of the sources of non-linearity and is one of the biggest challenges in FE modelling. Objects are considered in contact when the contacting surfaces become mutually tangent [40]. Even though contact is just two or more object touching, modeling contact introduces more complexities and computational demands. The complexities arise from the changing stiffness matrices, changing boundary conditions and loads, presence of potential relative motion after contact, and determining the region and interface of contact [41]. Other traits of contact in FEA include the impenetrability of the surfaces and the ability to transfer compressive normal or tangential friction forces [40].

In ANSYS, contact pairs are defined by the user and the surfaces are marked as either a contact or target face shown in Figure 19.

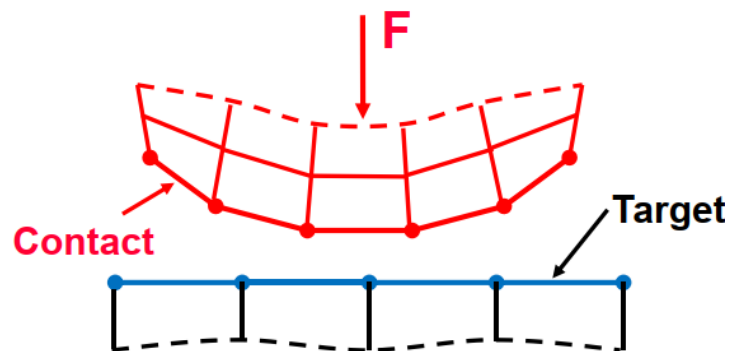


Figure 19: Contact definition in ANSYS [40].

Once a contact pair is established, several contact types can be assigned. Table 2 lists the contact types and their characteristics.

Table 2: Contact type and behaviour [42].

Name	Gap Open/Close?	Sliding Allowed?
Bonded	No	No
Rough	Yes	No, infinite μ
No Separation	No	Yes, $\mu = 0$
Frictionless	Yes	Yes, $\mu = 0$
Frictional	Yes	Yes, if $F_{\text{sliding}} > F_{\text{friction}}$

Bonded, frictional, and frictionless contact types were used for the current research. Bonded contact can be considered as a gluing between the parts, with the loads transferring directly from part to part as one body. Frictionless contact has the least amount of restriction of all the contact pairs with the two parts being able to freely come in and out of contact and slide tangentially with a coefficient of friction of zero. Frictional contact shares the same freedom of movement as a frictionless type, but also includes a frictional tangential force along the contact interface that resists the tangential movement.

The two main contact formulations used in the research were penalty-based and Multi-Contact Point (MPC), and the usage depends on the contact type. For penalty-based contact algorithms, a spring is introduced at the contact interface to resist penetration. The spring introduces a normal force shown in equation 19 for a pure penalty formulation:

$$F_n = k_n x_p \quad (19)$$

where x_p is the penetration distance between the contact and target face. Figure 20 outlines the interaction between the contact pair and the normal force.

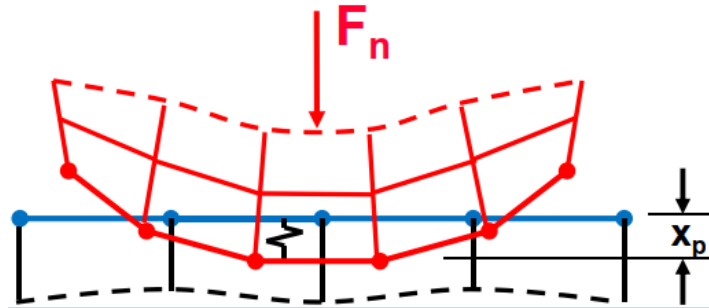


Figure 20: Normal force during contact [40].

In addition to a normal force, there is also a tangential force that determines the amount of sticking or slipping of the mutually tangent objects given by equation 20:

$$F_{\text{sliding}} = k_{\text{tangential}} x_{\text{slide}} \quad (20)$$

Accuracy of contact pairs depends on the contact stiffness. An infinite stiffness would be ideal, but is impossible numerically. A higher value would have the least

penetration and the most accuracy, but convergence may be difficult with potential oscillations of the contacting surface. To decrease the reliance and sensitivity of k_n , another penalty-based method, called the Augmented Lagrange formulation, introduces another term (λ) as in Equation 21:

$$F_n = k_n x_p + \lambda \quad (21)$$

The Augmented Lagrange method was mainly used for contact between the appendages and bearing pad to pressure tube with frictional and frictionless contact types. However, for bonded and no separation contact models, the MPC algorithm is used. For this formulation, mathematical equations join the contact pair as one body, such that the displacements and loads transfer between the bodies. Figure 21 highlights the constraints between the two surfaces.

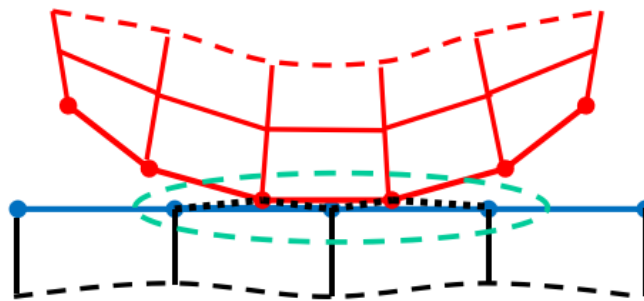


Figure 21: Constraints for MPC Formulation [40].

Bonded contact can also be considered as a linear analysis for small deformations despite being a contact type. MPC formulations allow large deformations to be run with bonded contact.

5.5.1 Parallel Computing

Advances in computing technologies and hardware allowed for the capability to solve a finite element analysis of the full fuel bundle in a matter of hours rather than weeks. Significant improvements in High Powered Computing (HPC) permits a larger node count, finer meshes, greater degrees of non-linearity, and multiphysics studies in a shorter time period. The solution phase of finite element analysis sees the most benefit from HPC systems where the computing hardware determines the solution speed independent from the user.

In terms of the hardware, there are two categories for paralleling computing, Shared Memory Parallel (SMP) versus the Distributed Memory Parallel (DMP) memory systems. SMP architecture functions by connecting all processors to a single memory unit that is shared as seen in Figure 22.

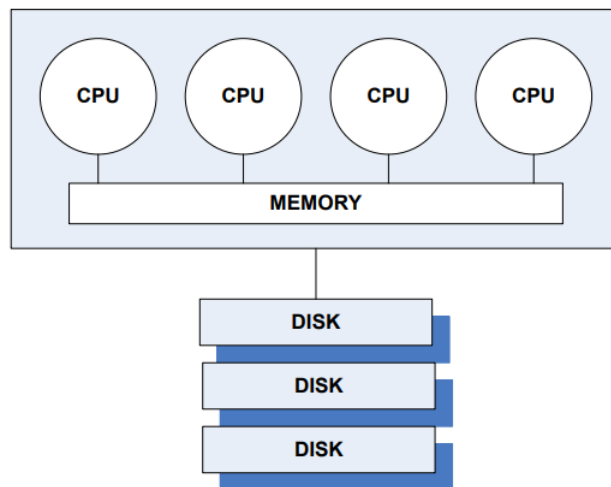


Figure 22: Shared Memory Parallel Architecture [43].

In the case of SMP, all processors are connected to a common memory unit and lack the ability to scale depending on the amount of CPUs. The layout can represent a single workstation or server [44]. On the contrary, DMP architecture separates the CPU and the memory which are independently connected to the I/O (input/output). This allows for a greater degree of parallel processing, scalability according to the CPU amount and faster solutions. The benefits also come at the cost of greater bandwidth requirements and greater complexities in the coding to allow for communication between the CPUs [45]. DMP architecture is shown in Figure 23.

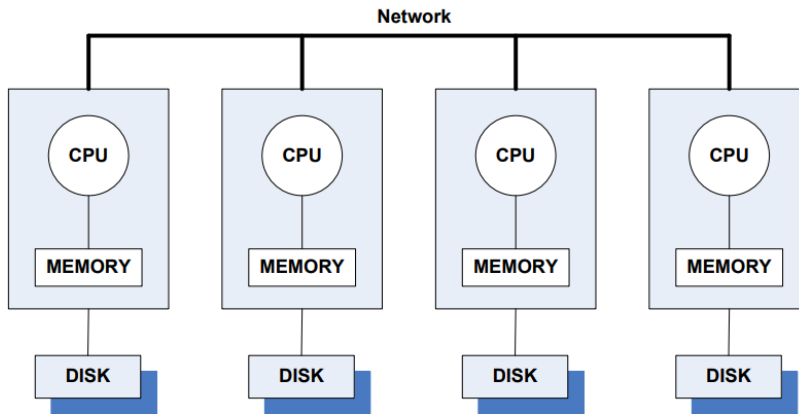


Figure 23: Distributed Memory Parallel Architecture [43].

Different benchmark nonlinear studies have shown that the relationship between runtime and CPU core count does not scale linearly. In the case of a turbine blade FEA with 3,200,000 DOF, the runtime times for each core count compared to the benchmark 2 cores is shown in Figure 24 [46].

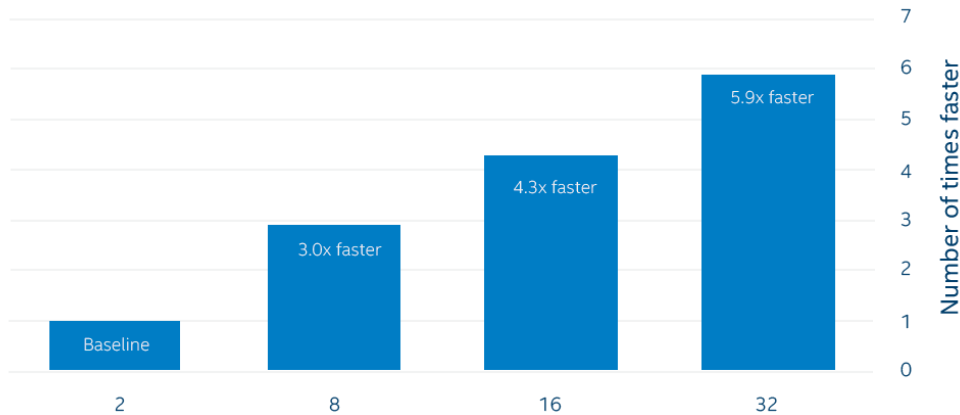


Figure 24: Runtimes compared to benchmark core count [46].

The lack of linear scaling between the core count and solution time shows the importance of software optimization to fully take advantage of the number of CPUs.

HPC hardware from CMC Microsystems was selected for the current research due to the inclusion of a Graphical User Interface for ease of use and being more cost

effective than other options. For the current research, an HPC from CMC Microsystems was utilized with an Intel Xenon processor with 16 cores with 125.8 GB of RAM on a Linux operating system. The full specifications can be seen in Appendix A.

6. Preliminary Studies

The goal of the current research was to develop a finite element model of an empty 37-element CANDU fuel bundle and to study the effects of PT creep diameters on bundle deformation. The model is built upon Lt. Soni's works on a partial 12-rod model that was validated with experimental testing and analytically verified for simple mechanical responses [28]. The model development was split into two phases consisting of preliminary studies using a single rod model, followed by simulations of the complete 37-element bundle. Chapter 6 presents the single rod model that was used to determine the loads and boundary conditions required to achieve the same deformation profile as the PIE and bundle heat up experiments from Figures 12 to 14. The single rod model was also used to determine the effect of the bearing pad locations on the deformation profile. Chapter 7 presents the complete 37-element bundle. Sensitivity analyses were conducted on the loads and boundary conditions, and the effects of pressure tube diameters on the deformation of the bundle were investigated.

6.1 Overall model approach

The goal of this section was not to predict the deformed shape of the elements based on operating parameters or to represent a specific point in time or condition such as an accident. The goal was to capture the overall shape of the experimental tests through different small scale tests. Consequently, arbitrary loading consisting of gravity, forces, temperature and creep were applied to achieve the same overall shape of an "S" as shown in Figures 12 and 13. There are numerous profiles for a bundle, but difficulty arises in trying to mimic all the reactor conditions for all the bundles. For the 1-rod model with the rod sitting on the PT, the 'S' shape was selected due to the greater probability of occurrence for lower elements in contact with the PT due to the 3 planes of BP. Also, endplate dishing caused by the coolant hydraulic load and bundle parallelogramming from PT sag both contribute to the 'S' shape. Pellets are not included because the overall deformed shape could be achieved by other means, without requiring this level of complexity and due to the assumption of no pellet heat generation. The two aspects that were most important were the contact and the end conditions. This meant that bearing pads were needed as well as the end plates and end caps.

6.2 Single rod model description

Models of a single rod were used for preliminary tests due to their relatively short runtimes. The purpose of the preliminary studies was to determine the appropriate boundary conditions and loading to achieve the same overall deformation profile as the PIE experiments from Figures 12 and 13. The first study looks at different constraints on the bearing pads that are in contact with the pressure tube as well as the end plates being free to expand axially or being constrained. The second study focuses on the applied thermal gradient for a fuel rod with pellets inside and without pellets. The final study examines the bearing pad configuration and between in-line or staggered.

6.2.1 Geometry and Element Type

The bundle design studied by Lt. Soni follows the Bruce Power and Darlington nuclear stations with the CAD files representing the geometry used experimentally at CNL. As described in Section 2.1, currently manufactured and operated CANDU fuel bundles consist of 37 fuel rods all welded to an endplate with brazed appendages on the rods for different functions. An isotropic view of the full bundle can be seen in Figure 25 and an axial view of the bundle encased in a nominal diameter pressure tube is shown in Figure 26 along with the coordinate system.

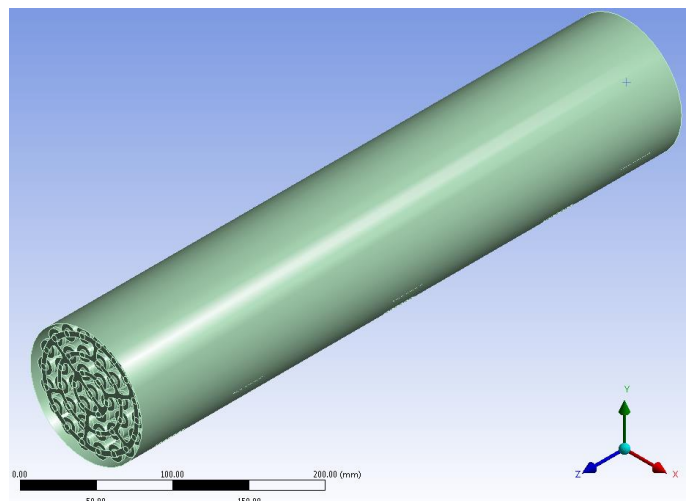


Figure 25: Full bundle isometric view with coordinate system.

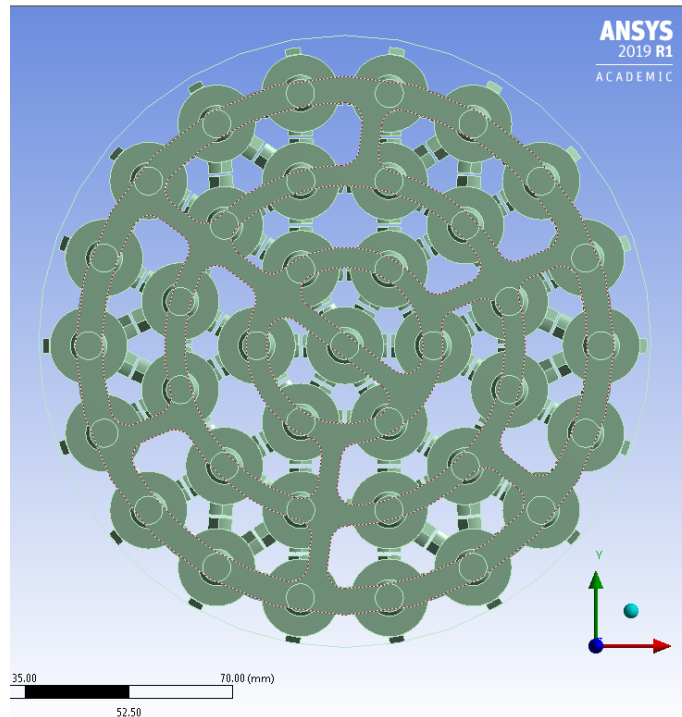


Figure 26: Full bundle axial view.

The spacer pads are not in-line, but instead, the SP pairs are configured in an 'X' formation, shown in Figure 27, to mitigate sheath-to-sheath contact. Unfortunately, due to this configuration, symmetry along any geometric plane was not possible.

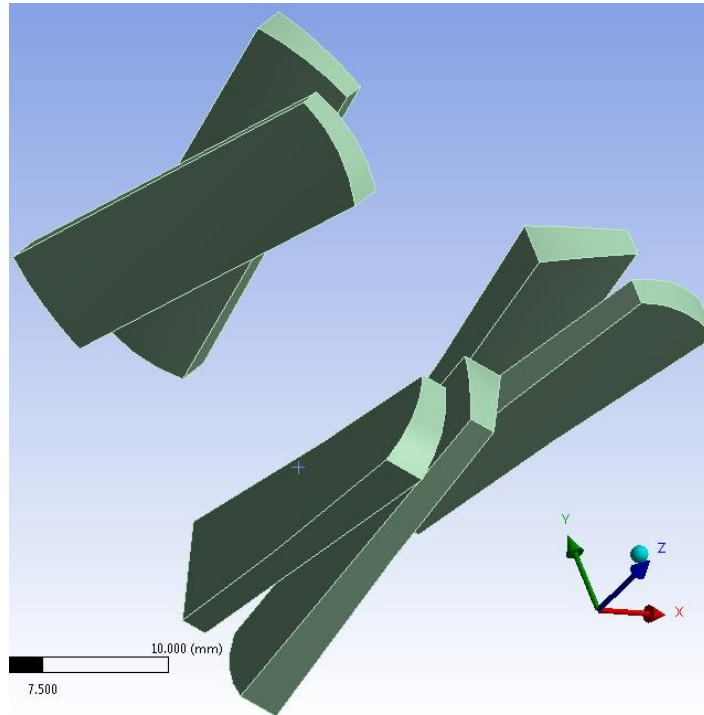


Figure 27: Spacer pad contact pair misalignment.

The 1-rod model consists of a single rod with bearing pads, end plates, endcaps and the PT seen in Figure 28. The thin walls relative to the length and diameter of the sheath and pressure tube allowed for 3D shell elements to be assigned rather than 3D solids. 3D solids allow stresses through the thickness, but for the current research only the deflections of the sheaths are of interest. Lt. Soni demonstrated a minimal difference between the deflection values of a fuel rod when 3D solid and a 3D shell elements were used [28]. The endplates were also assumed to be shells due to the large, flat, and thin geometry, and the lack of penetrative contact. The endplates merely assist in supporting the sheaths. Assigning these components as shells rather than solids aided in simplifying the model by reducing the number of nodes as the thickness was not explicitly meshed. The bearing pads, spacer pads, and endcaps were maintained as solid elements. A table of dimensions of Figure 28 can be seen in Appendix B.

The PT was kept at a nominal diameter with 0% diametral creep. The PT was also assumed to be rigid as its only role is to provide a contact surface to support the bundle.

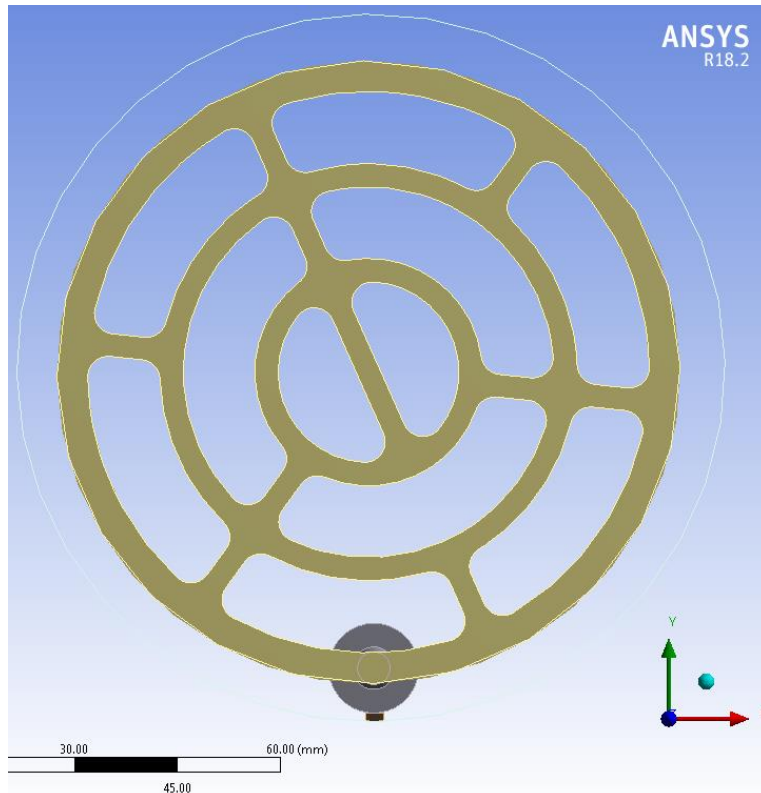


Figure 28: Axial view of 1 rod model configuration inside pressure tube.

6.2.2 Mesh

The tubular sheath and the pressure tube were meshed with a mapped mesh of higher order quadrilateral elements. Lower order tetrahedral elements were used for the endcaps due to their rounded features. Because the end components were only used for structural support and load transfer, lower order elements were justified. The appendages' meshes were sized according to their contact pair with the pressure tube, and their uniform nature allowed for higher order quadrilateral elements. Figure 29 shows the overall mesh of the single sheath contained in the pressure tube.

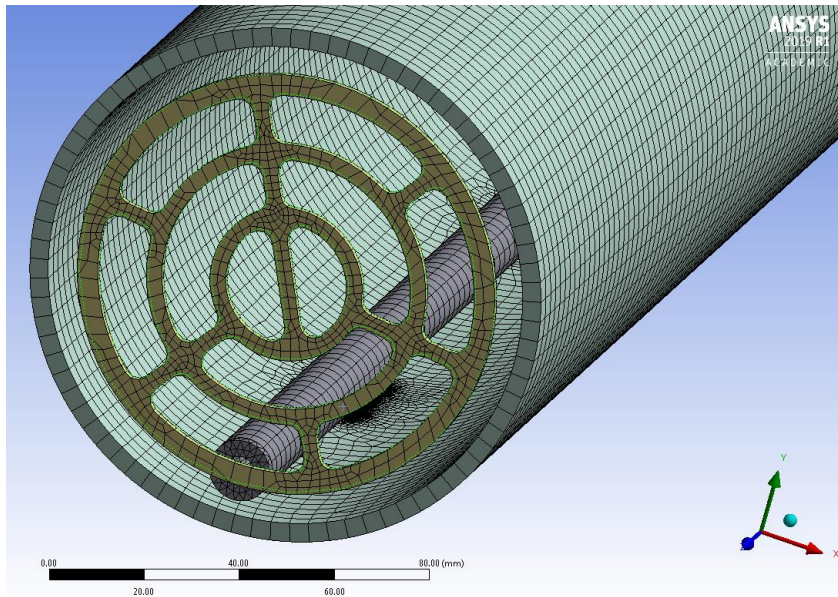


Figure 29: Mesh for rod 10 in the PT.

The region of densely packed nodes under the bearing pad and on the pressure tube shows the contact sizing method, and was the biggest contributor to the node count. This is the result of a contact pair sizing where the mesh between a contact pair is aligned and concentrated to assist in numerical convergence.

6.2.3 Contact

Bonded and frictional contact were used in the simulation as outlined in Table 2. Bonded contact was used between the sheath and the end cap, the end cap and the end plate and between the sheath and the bearing pads to mimic the brazings and welds between the endplate, endcap, sheath, and appendages. Bonded contact is essentially the joining of two parts into one, and was used to keep the parts together. The bearing pad to pressure tube was assigned a frictional contact definition with a coefficient of friction of 0.1. This assumption also was made by Atomic Energy of Canada Limited for their modeling of the CANFLEX bundle and was deemed appropriate due to the same Zircaloy-4 material being used [8]. A value of 0.1 is near frictionless but still allows some resistance due to unknown surface conditions in an operating environment.

6.2.4 Material Properties

The material properties were the same for Zircaloy-4 as found in the MATPRO, such as the Young's modulus and coefficient of thermal expansion. The temperature change of the Young's Modulus and Poisson's Ratio can be seen in Table 3. The coefficient of thermal expansion is $0.000006721 \text{ } ^\circ\text{C}^{-1}$.

Table 3: Zircaloy - 4 Young's Modulus temperature dependence [47]

Temperature (C)	Modulus of Elasticity (GPa)	Poisson's Ratio
290	92.9	0.2
400	86.9	0.21
500	81.4	0.22
600	76	0.23
700	70.5	0.23

The Norton Creep law was selected to represent the diffusional creep experienced by the bundle components. The creep strain rate is determined by:

$$\dot{\epsilon} = C_1(\sigma_a)^{C_2} e^{\frac{-C_3}{T}} \quad (22)$$

Where T is the temperature, σ_a is the stress, and the Norton creep constants are listed in Table 4.

Table 4: Zircaloy - 4 Norton creep constants temperature dependence [47]

Temperature ($^\circ\text{C}$)	C_1	C_2	C_3
290	4.7E-13	2	9431
700	8.6E-13	2	9431

Several assumptions were made for the material properties to simplify the analysis. First, the Zircaloy-4 properties were assumed to be isotropic. Despite the PT's material being a Zirconium alloy with 2.5% niobium, the PT was also assigned as Zircaloy-4 because it only acted as structural support. Finally, all analyses were done before the alpha-beta transition of Zircaloy-4 at approximately $800 \text{ } ^\circ\text{C}$ and only the alpha grain structure was considered in the model for simplification.

6.2.5 Loads and Boundary Conditions

Three preliminary studies were conducted with different boundary and loading conditions as outlined in Table 5. The overall goal was to qualitatively match the deformation profiles with those presented by PIE and bundle heat up results from Figures 12 to 14.

Table 5: Preliminary studies using the single rod model

Preliminary Test	Parameter under investigation
1	Effects of Boundary Conditions
2	Effects of Thermal Loading (constant vs. gradient for with/without pellets)
3	Effects of Bearing Pad placement (staggered vs. in-lined)

Gravity was included for all models as well as thermal creep of 100 s. The overall goal was to qualitatively match the deformation profiles with those presented by PIE results. The specific boundary conditions and loads for each preliminary test will be discussed in the following sections 6.2.5.1 to 6.2.5.3.

6.2.5.1 Preliminary study on boundary conditions

A one rod model connected to endplates and sitting on a pressure tube was prepared to test the boundary conditions listed in Table 6. At least one BP was bonded to the PT at all times to prevent rigid body motion of the entire bundle. The studies aim to show the most appropriate BP and endplate constraint to obtain the ‘S’ shape seen in Figures 12 and 13. The overall bundle sits in the PT supported by 3 planes of bearing pads. The bearing pads are free to slide along the PT surface as the bundle expands and deforms. The bundles sit end to end within the channel with small gaps between them. The gaps may close due to bundle axial expansion and there may be end to end contact. The final bundle in the downward stream is held against the coolant flow by a side stop that also aids during refueling. These conditions are represented in the FE model in the FE model with appropriate BCs. The forces on the bundle are idealized in Figure 30. The ideal case of the endplates being axially constrained, or free were considered.

Table 6: Boundary condition small scale test cases.

Boundary condition test	BCs
1	Bundle mid-plane BP bonded to PT, outer BPs frictionally constrained, and endplates axially fixed
2	All 3 planes of BP bonded to PT, endplates axially fixed
3	Centre BP bonded to PT, outer BPs frictionally constrained, endplates axially free
4	Outer BPs bonded to PT, centre BP frictionally constrained, endplates axially fixed

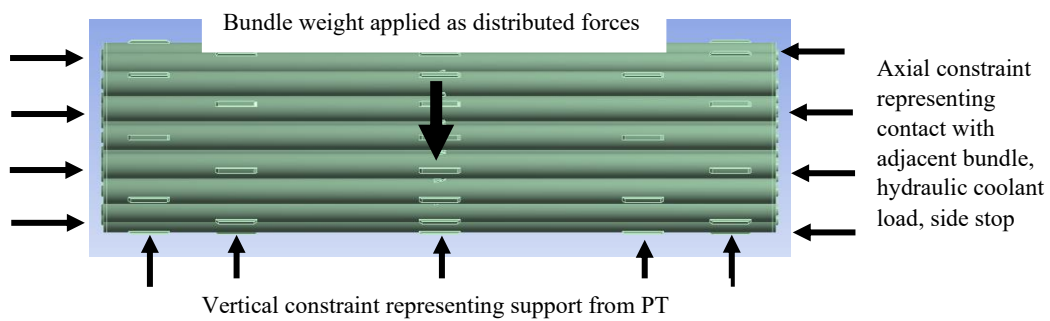


Figure 30: Idealized loading and boundary conditions.

The BCs in Table 6 are illustrated in Figures 31 to 34 with red circles signifying bonded contact to the PT and yellow denoting an axially constrained endplate.

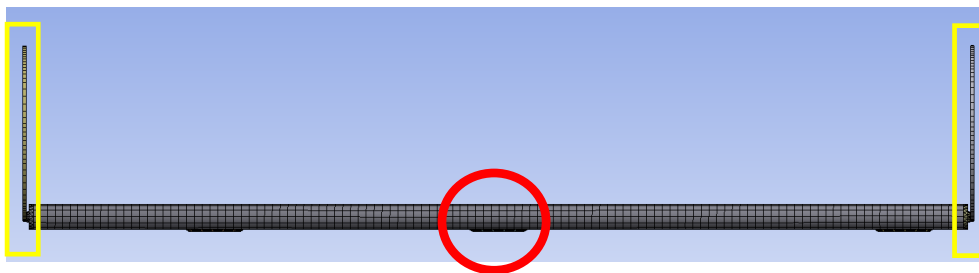


Figure 31: Illustration of test 1.

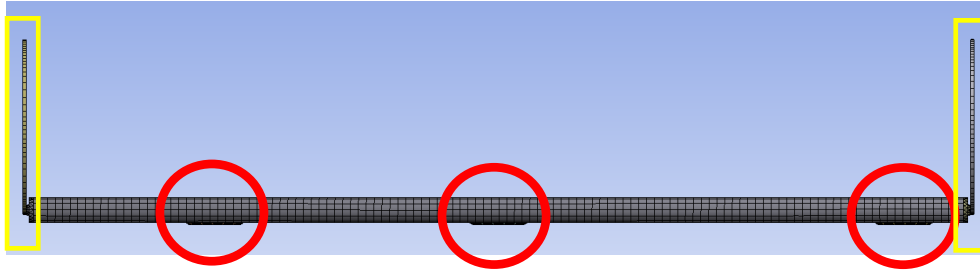


Figure 32: Illustration of test 2.

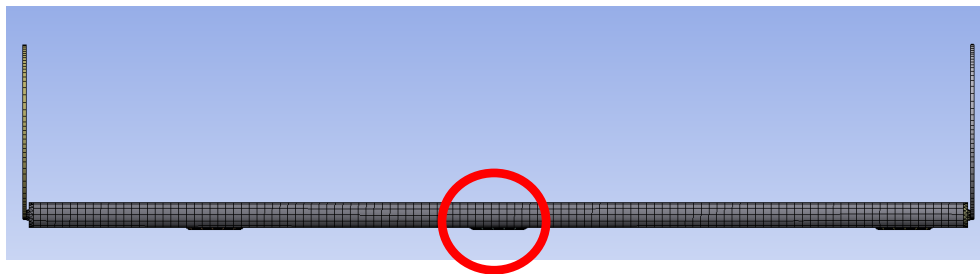


Figure 33: Illustration of test 3.

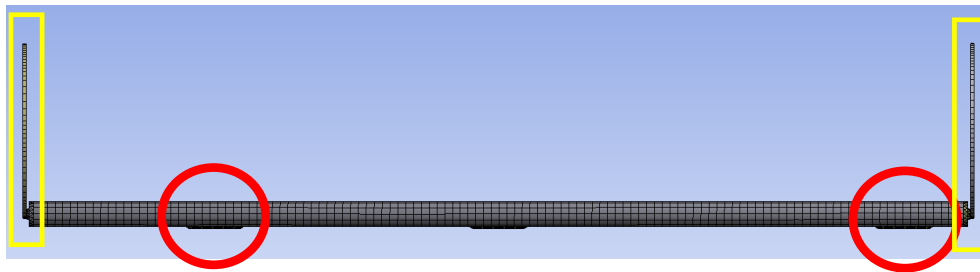


Figure 34: Illustration of test 4.

Loads of 50 N downwards on the sheath, temperature of 450 °C, thermal creep of 100 s, and effects of gravity on the sheath, endplates, endcaps, and appendages were included. The thermal load is higher than normal operating conditions to increase the effects of thermal expansion and accelerate the influence of creep. For the cases where the endplates were constrained, the entire face was axially fixed and kept parallel because it was assumed that all the bundles in a channel are kept together by neighbouring bundles. Thus, any slanting of the endplates and rods were neglected which removes the consideration for endplate dishing or doming.

6.2.5.2 Preliminary study on thermal loading

The next study was used to determine if the inclusion of pellets and which type of thermal loads would garner the ‘S’ shaped from PIE. Thermal load effects were compared by applying the temperature as an axial gradient from 400 °C to 650 °C to represent the differential cooling, and as a constant temperature of 500 °C. These temperatures are higher than operating temperatures, yet before the Zr-4 grain structure transition, to artificially accelerate the creep effects. Pellets were also included to see if they contributed to the ‘S’ shape or if the pellets could be neglected. Individual pellets were included in the rods and can be seen in Figure 35. Pellets were included by assigning frictionless contact and no separation contact between the rod and pellets. Table 7 shows the different test cases. The axial thermal gradient was included by assigning a linear temperature distribution of 400 °C on the furthest left pellet face and 650 °C on the furthest right pellet face.

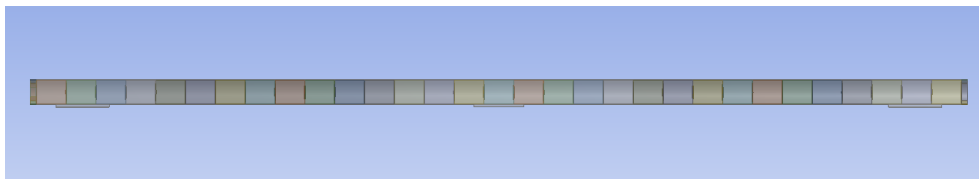


Figure 35: Configuration of the pellets inside the rods [27].

Table 7: Load condition small scale test cases.

Thermal Loading Test	Vertical Force	Pellet Weight	Creep	Thermal Load	Thermal Gradient	Pellet
1	✓	✓	✓	✓		
2	✓	✓	✓	✓		✓
3	✓	✓	✓		✓	
4	✓	✓	✓		✓	✓

6.2.5.3 Preliminary study on bearing pad placement

The two bearing pad configurations considered were the staggered design from Bruce and Darlington stations versus the in-line configuration seen in the Pickering and CANDU-6 stations. Consequently, while the current research is based on the staggered configuration, a single rod with the BPs in-line was also created. The spacer pads, endplates, and PT were not included. Boundary conditions were used

to represent the PT by preventing motion through vertical Z axis. The two configurations are shown below in Figures 36 and 37, the bearing pads are highlighted in green, and the distance between the BPs are highlighted in yellow. Pellets are included due to the relatively low node count of the 1 rod model while maintaining a realistic approach.

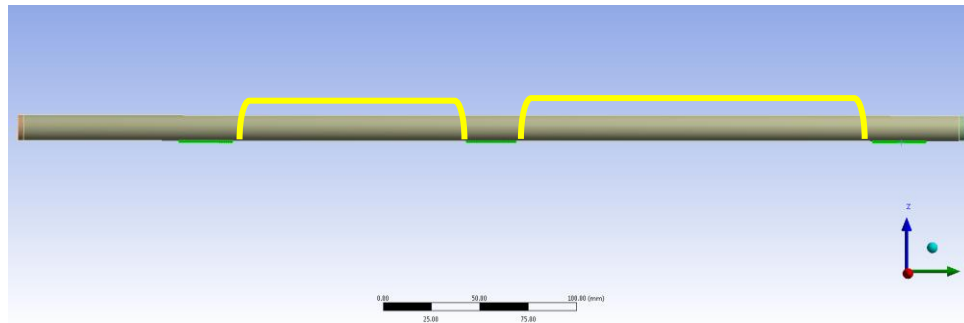


Figure 36: One rod model with staggered BPs.

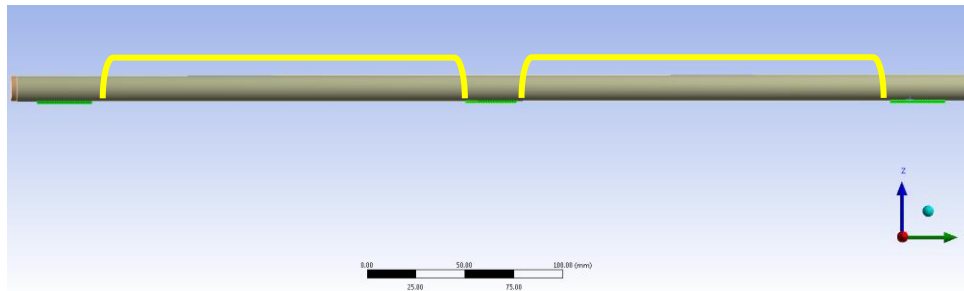


Figure 37: One rod model with in-line BPs.

The same linear axial temperature gradient from 400 °C to 650 °C in section 6.2.5.2 was applied lengthwise on the rod with pellets included.

6.2.6 Solution

The analysis for the 1-rod model was non-linear with large deflections and with 2 load steps. These two load steps are important for separating the static loading from the creep strain [48]. The first load step allows all the loads to be applied initially, then the second load step simulates the influence of creep. All models were considered static and at steady state.

6.3 Single Rod Results

The side view of the vertical deflections from the 1-rod models was compared with the profilometry data from Figures 12 to 13. The deformations were viewed magnified to better visualize the resulting bundle sag. The goal of the 1 rod small scale tests was to determine the appropriate loads and boundary conditions that would qualitatively match the profile shown by PIE results and bundle heat up tests. The suitable loads and BCs would be implemented on the full bundle.

6.3.1 Effects of Boundary Conditions

The side profile of the vertical deflections without the pressure tube is shown in Figures 38 to 41. The deformation results are scaled to exaggerate the results and better visualize the profile. Figure 38 shows the deformed shape with endplates axially fixed with the centre BP bonded to the PT. The left end deflects more than the right because the left BP is further from the left end. A slight upwards displacement is seen between the left and centre BP because of this. The BPs are able to lift off the PT and rotate, allowing more deflection to occur because there are no rods above to keep the lowest rod down. Figure 39 shows the deformed shape with the endplates axially fixed and all 3 BPs bonded to the PT. When all 3 BPs are fixed, the regions between the BP thermally expands and actually displace upwards. The end plates droop because of their self weight. Figure 40 reveals the deformed shape of the endplates axially free and only the centre BP bonded to the PT. When the endplates are free to expand, there is no ‘S’ shape because the rods thermally expand axially. Figure 41 shows the endplates axially free, and the outer BPs bonded to the PT with the centre BP able to come out of contact with the PT.

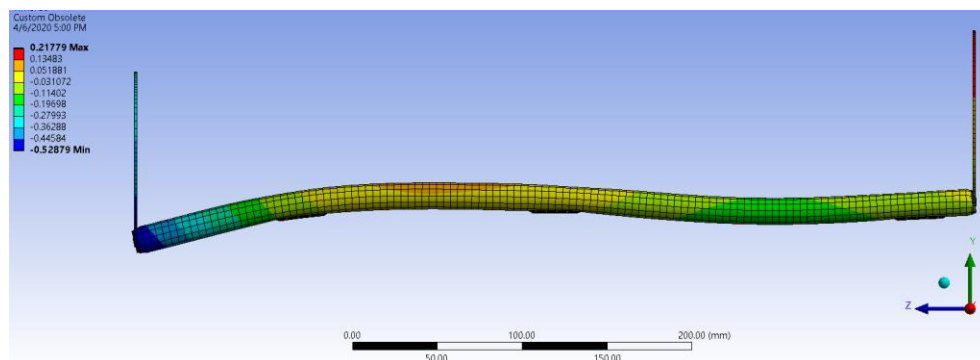


Figure 38: Test 1 - vertical deflection (mm) of 1 rod at 55x scale with endplates axially fixed, centre BP bonded to PT.

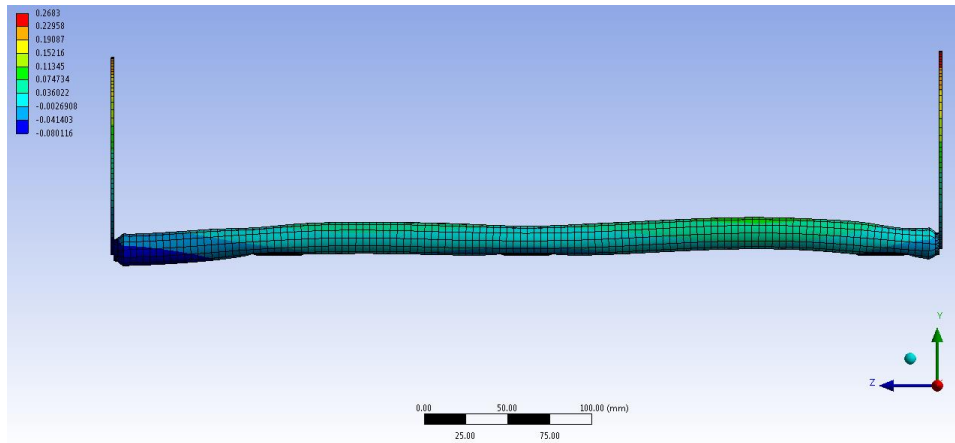


Figure 39: Test 2 - vertical deflection (mm) of 1 rod at 96x scale with endplates axially fixed, all 3 BP bonded to PT.

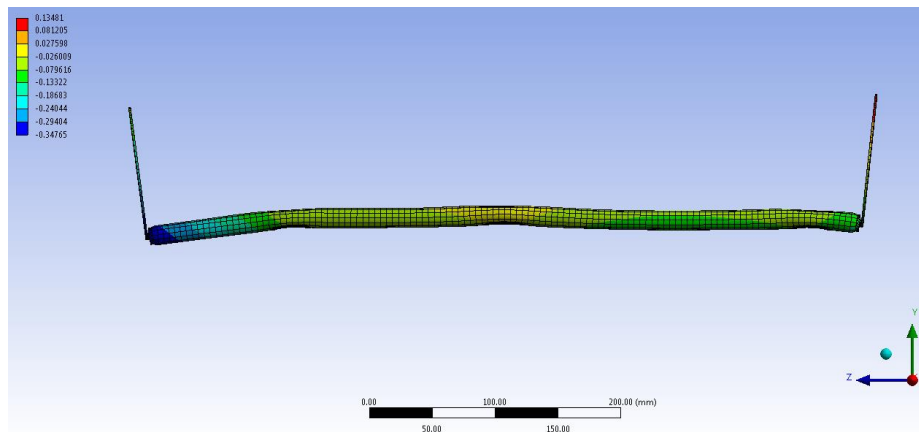


Figure 40: Test 3 - vertical deflection (mm) of 1 rod at 51x scale with endplates axially free, centre BP bonded to PT.

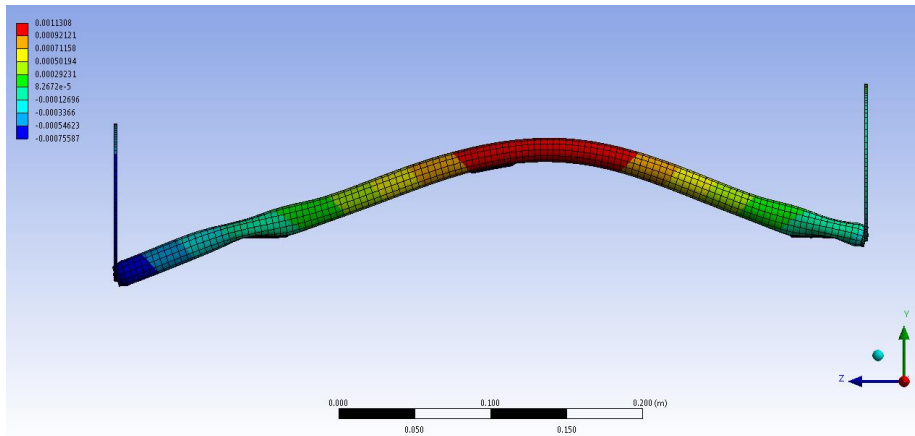


Figure 41: Test 4 - vertical deflection (m) of 1 rod at 45x scale with endplates axially fixed, centre BP frictional condition, outer BPs bonded to PT.

The boundary conditions applied on Figure 38 were the most appropriate in matching the PIE results from Figures 12 and 13. Figure 42 plots the vertical deflection measurements lengthwise for the BC found in Figure 38. The endcaps are not at the 0 μm locations compared to Figures 12 and 13 due to the cradle keeping the ends fixed for the measurement device. The 1-rod model only considered a single element and has an exaggerated effect of endplate drooping as seen by the left.

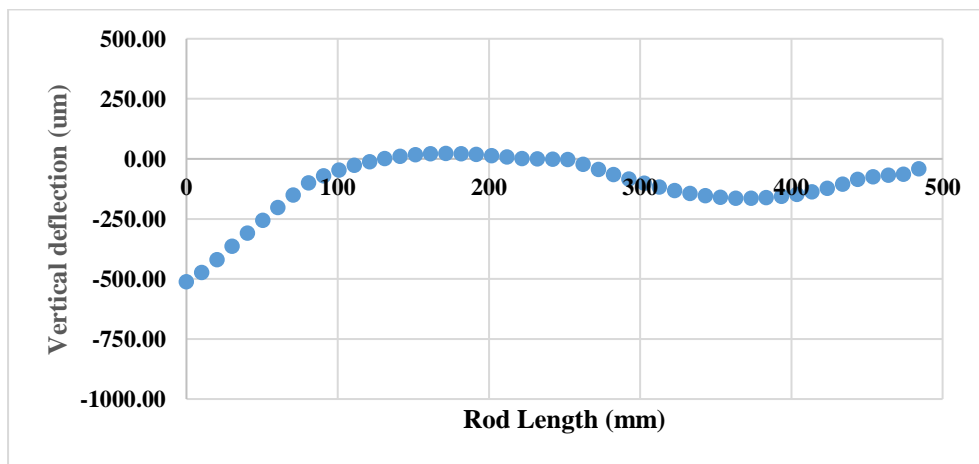


Figure 42: Vertical deflections (μm) lengthwise plot of BC test case 1.

6.3.2 Effects of Thermal Loading

With the boundary conditions established, different thermal loads were considered to determine which load garners similar ‘S’ deflection profiles as the bundle heat up tests. The loads from Table 7 were applied on four different models as shown from Figures 43 to 46. Figure 43 garnered a similar ‘S’ deflection shape as in Figure 38, but in Figure 44, the rods remained relatively horizontal due to the added pellets. When the thermal gradient was included in Figure 45, there is an ‘S’ shape up to the right BP, at which point the right end deflects up again. Figure 46 with both the pellets and thermal gradient allowed for a desired ‘S’ shape.

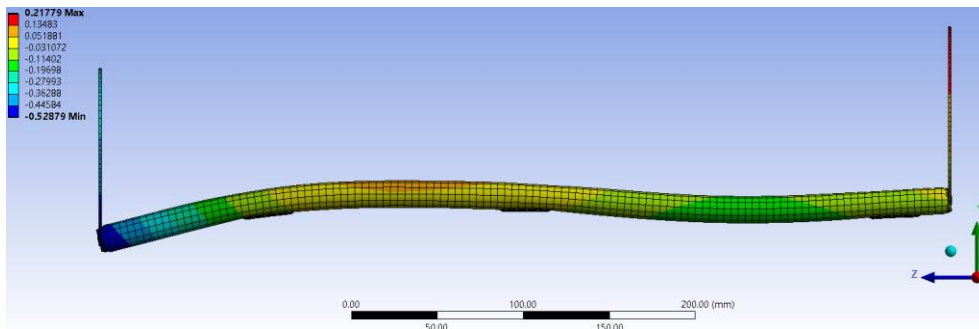


Figure 43: Test 1 - side view of vertical deflections (mm) at 48x scale of an empty rod with vertical force, gravity, thermal creep, and constant thermal load.

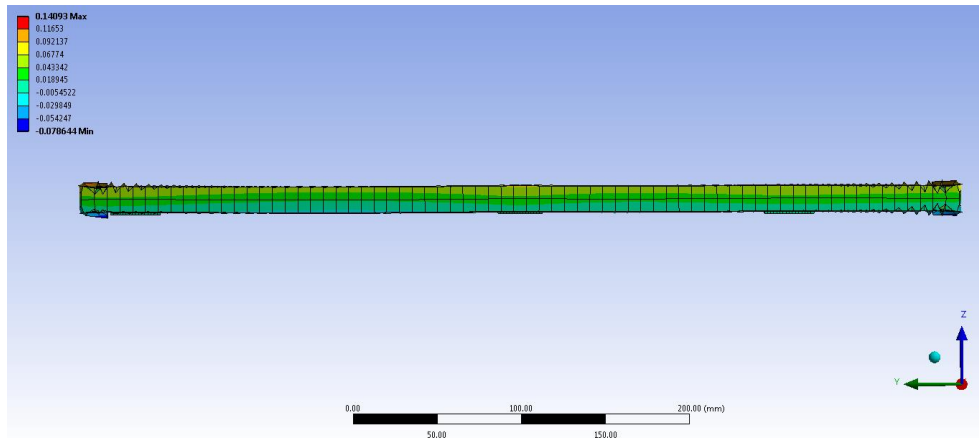


Figure 44: Test 2 - side view of vertical deflections (mm) at 44x scale of a rod with pellets and vertical force, gravity, thermal creep, and constant thermal load.

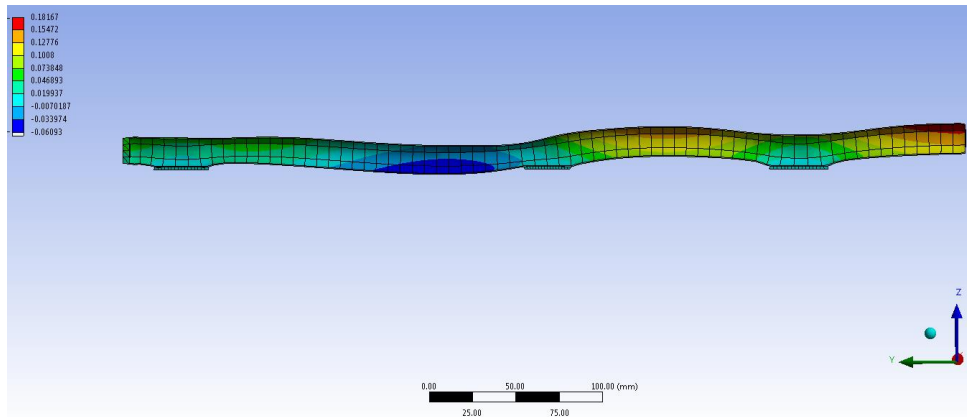


Figure 45: Test 3 - side view of vertical deflections (mm) at 67x scale of an empty rod with an axial thermal gradient.

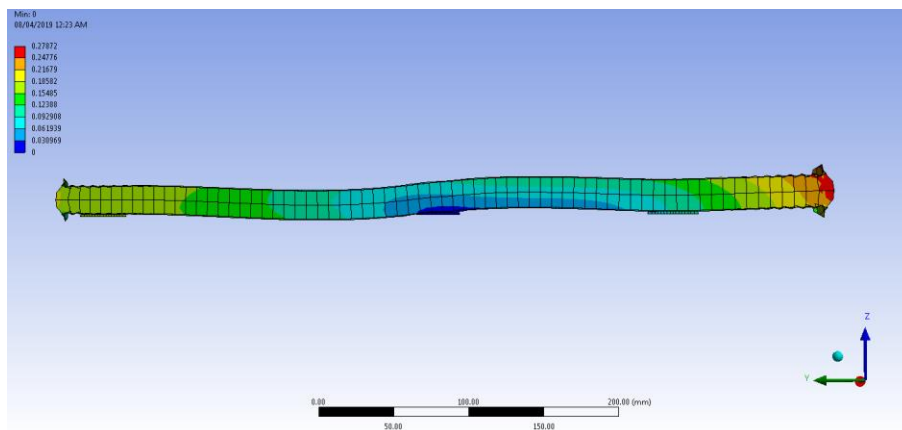


Figure 46: Test 4 - side view of vertical deflections (mm) at 78x scale with pellets and thermal gradient.

6.3.3 Effects of Bearing Pad Placement

The final test was performed to see the effects of bearing pad placement on the deformed shape of the rods. An axial temperature gradient from 400 °C to 650 °C was applied lengthwise on the rod with pellets included. The thermal gradient was already applied for the staggered BP rod illustrated in Figure 46. The same analysis was performed on the in-line BP rod and is illustrated in Figure 47.

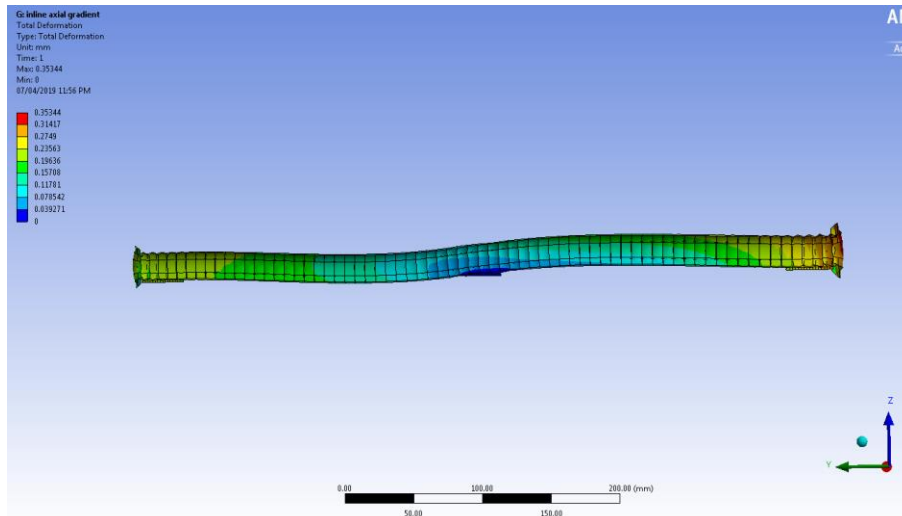


Figure 47: Side view of vertical deflection (mm) of in line BPs at 78x scale.

6.4 Discussion and Conclusions

The following remarks could be made from the preliminary results. The boundary conditions play a significant role in bundle deformation behaviour and garnering the desired deflection profile with regards to the PIE tests. Figure 38 aligns well with the PIE tests compared to the other boundary conditions. Bonding all the BPs and fixing the endplates would prevent the rod from deforming into the ‘S’ shape due to the overly restrictive boundary conditions. Furthermore, when the endplates were free, then the rod was able to expand axially and remained relatively horizontal with just the thermal expansion occurring. Finally, when the centre BP was not bonded to the PT, but the endplates were still fixed, this caused the rod to bulge upwards in the centre to relieve the compressive stresses. Thus, fixing the endplates to mimic neighbouring bundles, and bonding the centre BP to PT to represent the bundle sitting on the PT provided the most realistic deformations.

For the thermal loads, if a constant temperature was incorporated with pellets inside the rod, then the rod becomes too rigid and remained relatively horizontal as seen in Figure 44. However, when the axial thermal gradient was applied with pellets inside, then the rod deformed into an ‘S’ shape. As indicated in Figure 45, there is an ‘S’ shape until the right BP, where the rod deflects back up again due to the higher temperature. If pellets are included in the rod, while maintaining the same boundary conditions and just applying a thermal gradient, then the rod provides a deflection similar to the bundle heat up test as seen in Figure 13. With

regards to the thermal load, a combination of vertical force, thermal creep, constant temperature, and gravity results in an ‘S’ shape deflection for an empty rod. Once pellets are incorporated, then a thermal gradient is more appropriate in garnering the ‘S’ deflection profile. However, adding pellets for all 37 fuel elements necessitated too much computational hardware so an empty rod was chosen to proceed to the full bundle.

With the same thermal gradient and pellets included in the model, the same ‘S’ deflection is seen in both a staggered and in-lined BP configuration corresponding to different stations’ bundle design when viewing the vertical deflections at 78x scale in Figures 46 and 47. While for a single rod the differences are negligible, once the whole bundle is incorporated, the BP placements could have a greater impact due to the increased overall weight of all the rods.

A mesh convergence study was performed on just the rod without any appendages, end components or PT. A temperature load of 320 °C with just the pellet weight was applied with the ends axially constrained. The sheath mesh size was varied from 1 mm to 7 mm and the displacement was the result of interest. The node count for each mesh size was plotted with the displacement in Figure 48.

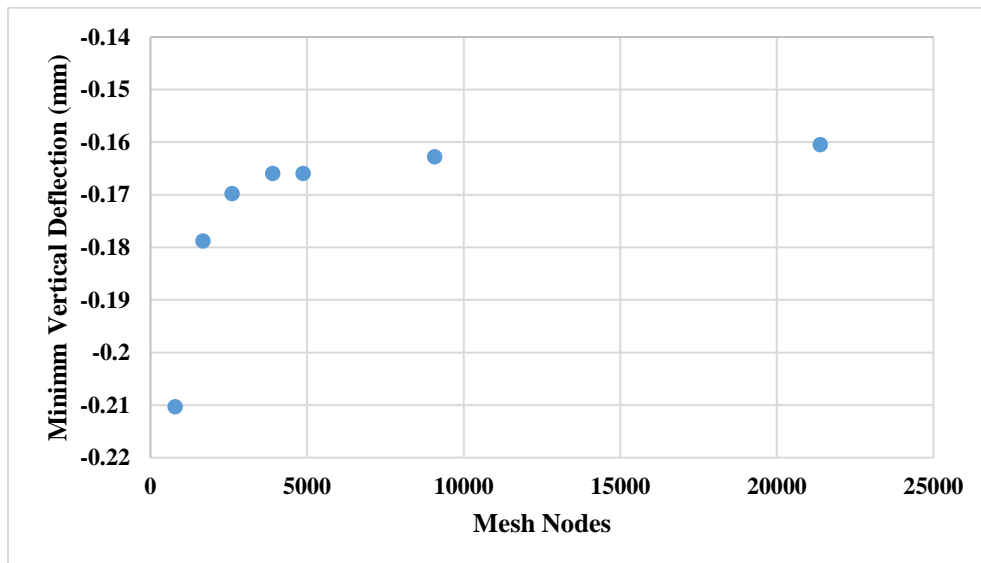


Figure 48: Mesh convergence study on a single rod.

Displacements was determined to be insensitive to the mesh size. The focus was on the contact between the appendages, keeping memory demands lower, and

predicting displacements, therefore a node count of 4880 or a mesh size of 2 mm for the rod was selected and applied to the full bundle.

As a result of the preliminary tests, empty rods with vertical forces, constant thermal loads, gravity, and the same BP configuration as Lt. Soni was selected to proceed with the full bundle analysis.

7. Thirty Seven Element bundle models

The results of the 1-rod small scale tests were implemented on the 37-element fuel bundle model, including removing the pellets and thermal creep, while including the vertical force, constant temperature, axially constrained endplates, and bonded contact between the centre BP and PT. Since the loads and boundary conditions from the 1-rod tests were only calibrated for the lowest rod in contact with the PT, sensitivity analyses were completed on the loads and boundary conditions for the full bundle in order to qualitatively match all rods to the PIE. First the results from the first iteration bundle model will be presented, followed by two sensitivity studies that looked at the axial constraint and the applied force. The results from the two sensitivity studies were used to create a final bundle model which was then used to determine the effect of PT creep on the bundle deformation.

7.1 First iteration bundle model

7.1.1 First iteration bundle model description

7.1.1.1 Geometry and Element Type

The geometry was kept similar to the 1-rod model with the only changes being the inclusion of all 37 rods. As in the 1-rod models, the sheaths, pressure tube, and endplates were represented as 2D shell elements due to their tubular and planar nature. This eliminated the physical thickness of the components, but the thicknesses were assigned to simplify the mesh. The appendages and endcaps were maintained as solid elements.

7.1.1.2 Mesh

The main method for meshing was drastically changed from the 1-rod models. Contact sizing was the predominant mesh method implemented for previous analyses, but was impractical when scaled up to a full bundle requiring multiple models with different PT diameters. Several changes were applied to the mesh in order to reduce the run times to less than 15 hours. First, the tubular shaped rods and pressure tube were meshed with linear multizone quadrilaterals to reduce the node count and because the focus was mainly on the qualitative shape rather than the numerical amount. A 2 mm element size was sufficient for capturing the geometry of the PT. The endplates were meshed with linear quadrilateral elements of size 1.5 mm while the endcaps were meshed with tetrahedral elements. The

spacer pads were sized as 0.5 mm with quadrilateral elements as well. Finally, the bearing pads were meshed with 0.4 mm hexahedral multizone elements. Figures 49 to 51 show the bundle mesh. With a final node count of 958501, the model required less Random Access Memory and the runtime was decreased to a practical duration. Further mesh settings are found in Appendix C.

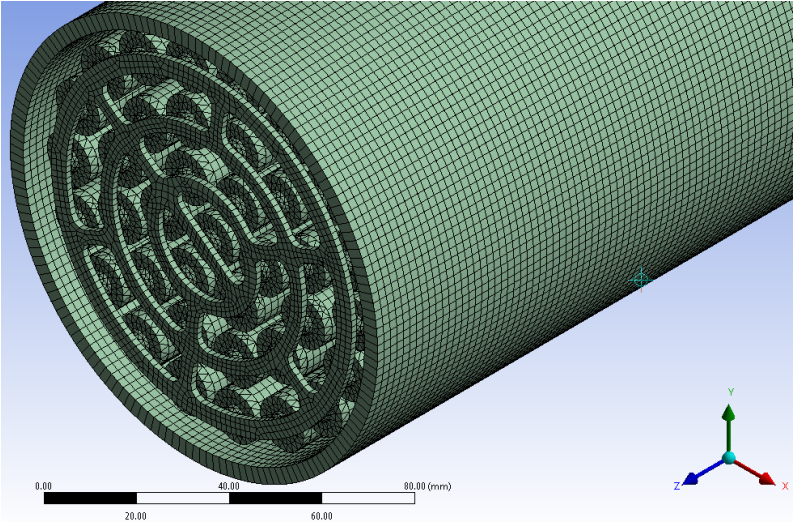


Figure 49: Isometric view of the bundle and PT mesh.

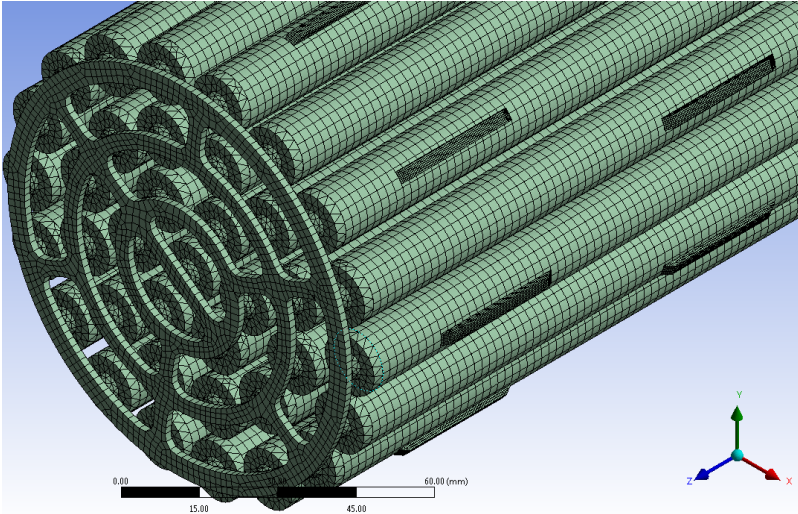


Figure 50: Isometric view of the bundle mesh.

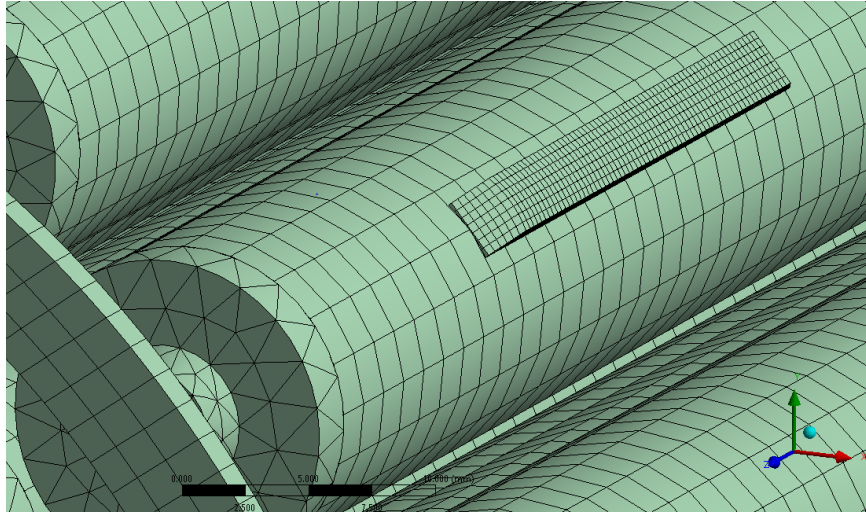


Figure 51: Close up of a sheath.

7.1.1.3 Contact

Contact was kept similar to the 1-rod bundle as described in Section 6.2.3, such as frictional contact with a coefficient of 0.1 was defined between each spacer pad pair and between each bearing pad and the PT. The uppermost 4 sheaths' BP to PT contact settings were removed to simplify the model as no contact was expected to occur within the top region of the PT.

7.1.1.4 Material Properties

The material properties were the same as outlined in Section 6.2.4, but creep data was removed to simplify the model.

7.1.1.5 Loads and Boundary Conditions

The 37-element model required an adjustment to the boundary conditions and loading as compared to the 1-rod models in order for all rods to deform as expected. Axially fixing both endplate faces to represent contact with the adjacent bundles was too restrictive for the full bundle model and resulted in non-convergence. To relieve some of the stress buildup while still preserving the same overall boundary condition effects, the webs on one of the endplates were fixed axially with remote displacement settings which allowed the rods' endcaps to

deform locally. This local bending permits a relief of compressive stress build up due to thermal expansion. The boundary conditions were applied to webs with no connected endcaps, as this allowed for minimal interference with how the rods would deform as seen in Figure 52. The remote displacement also allowed for localized bending and deflections of the webs while maintaining the axial constraint. The other endplate was still axially constrained by fixing the entire face to represent being held in place by neighboring bundles.

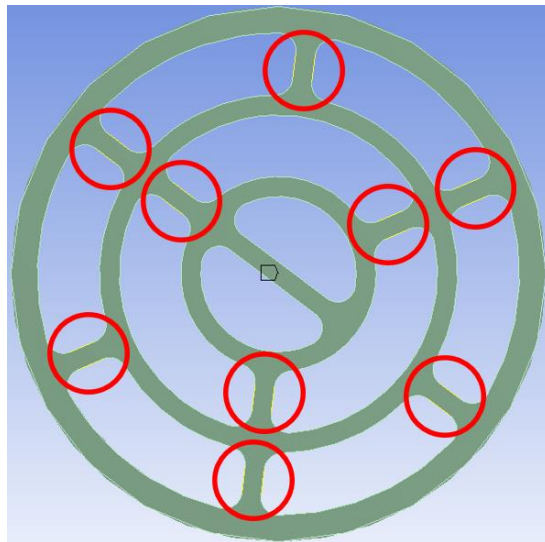


Figure 52: Remote displacements for the first iteration full bundle model.

After the sensitivity analysis on the boundary conditions was performed, one configuration of displacements on the endplate garnered the suitable deflection shape that matched the PIE and bundle heat up tests.

For the first iteration model, fixing all the endplate's webs allowed for a solution, however, the overall deformed shape did not match the PIE shape directly, particularly the outer elements. The constraints were all applied in the axial direction.

The first iteration of the full bundle maintained the same loads from the 1-rod models, in particular, the pellet weight as the vertical load, gravity, thermal load, gravity.

7.1.1.6 Solution

The first iteration model was run with 16 cores on the CMC cluster. Similar to the 1-rod models, the analyses were static, steady state, non-linear with large deflections. With all 37 elements, only one load step was applied because creep was not included. 10 initial substeps were applied and the runtime for the first iteration model was 47881 seconds or 13.3 hours.

7.1.2 Results

The first iteration bundle model was examined for proper contact between the appendages and the PT, and for deformation to match the PIE and bundle heat up tests. This results section presents the first iteration bundle results as well as the results from studies on the end plate constraints and the applied force.

7.1.2.1 First iteration Full Bundle Results

The axial view of the vertical deflections at true scale is shown in Figure 53. Contact was verified between the spacer to spacer pads and bearing pads to the pressure tube. Locations of spacer pad slippage and obstructed sub-channels are circled in red and yellow respectively. Deformation behaviour between the right and left halves of the cross-section are also different even when the same loads were applied equally on all rods due to the non-symmetric endplates. The centre bearing pads of rods 1, 18, 17, 16, and 15 in the upper left quadrant all contacted the pressure tube which was surprising because all rods in the top half were expected to sag down.

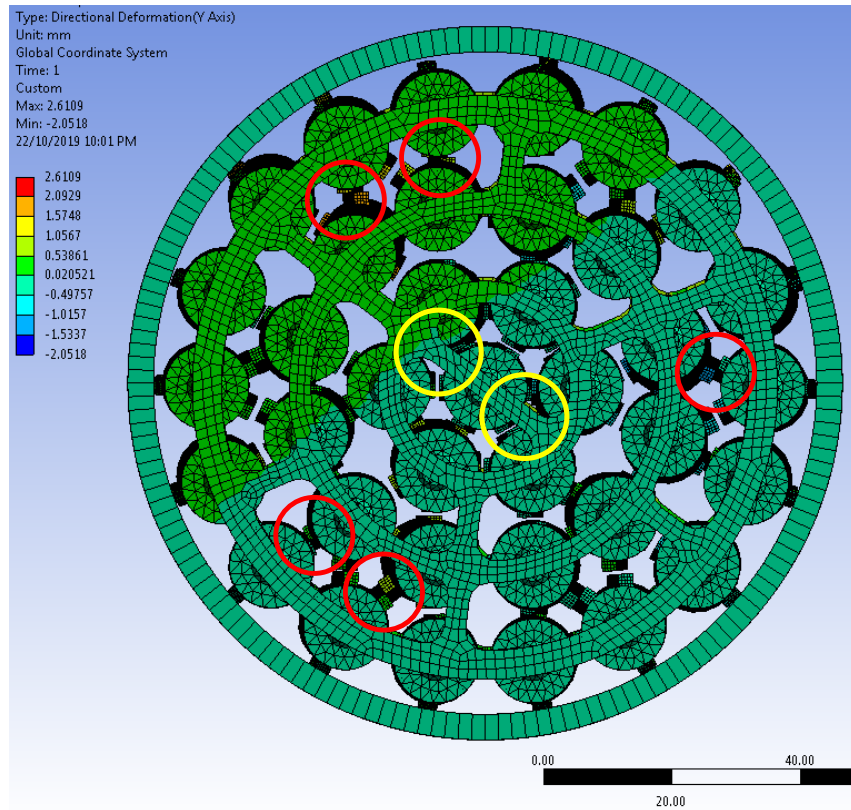


Figure 53: First iteration full bundle vertical deflections (mm) true scale.

The magnified vertical displacements of the outer rods are shown in Figure 54. The upward bowing of the upper half rods become more evident, in particular rods numbered 16, 17, 18, 1, 2, and 3. However, the lowest half sheaths better align with the PIE results as they bow outwards to fit the contours of the pressure tube.

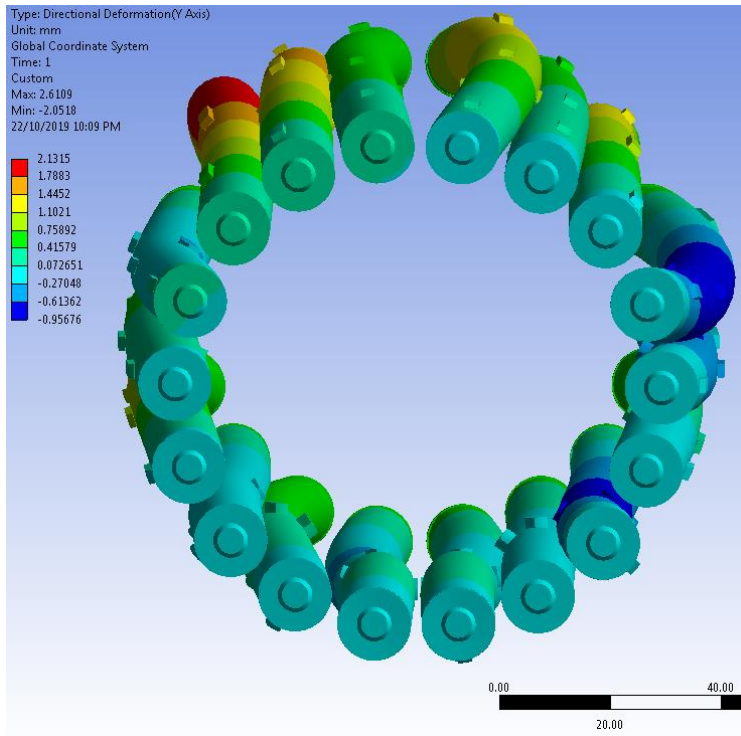


Figure 54: Vertical deflections (mm) of outer elements axial view 5x scale.

Inspection of rods 10 and 9 in Figure 55 show the side view of the vertical deflections at 19x true scale. The scaled displacements show the ‘S’ shape seen by the bundle heat up and small-scale tests.

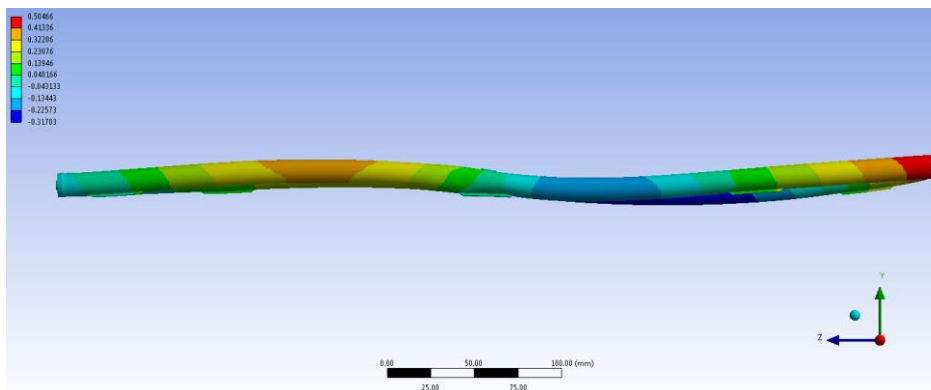


Figure 55: Vertical deflections (mm) of rods 10 and 9 side view 19x scale.

The effects of fixing the webs rather than the entire surface of the end plate are evident in Figure 56a), especially when the deformed shape is scaled up. There is localized bending at the locations where the endcaps are welded to the endplate. Figure 56b) clearly shows that the end plate does not deform when the entire face is axially fixed. The locations of where the rods are connected to the endplate and how the endplate is constrained become significant due to the ability to locally rotate at the flange locations.

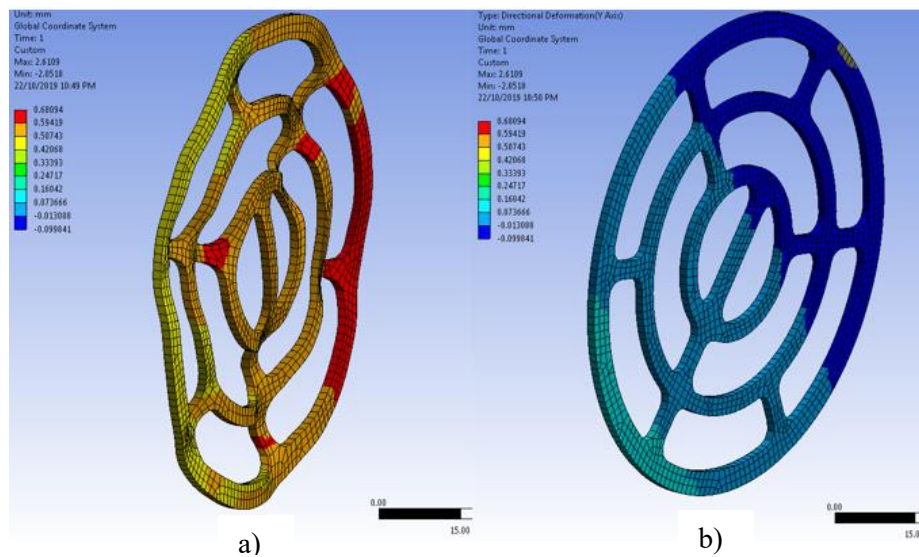


Figure 56: Vertical deflection (mm) of endplates with fixed webs (a) and constrained face (b) 5x scale.

The importance of boundary conditions applied on the radial webs was further explored by performing a sensitivity analysis on the location and number of webs that were axially fixed.

7.1.2.2 Sensitivity Analysis on Web Constraint

Six different boundary conditions were tested with all other loads and boundary conditions kept the same as the first iteration model shown in Table 8.

Table 8: Boundary conditions sensitivity analysis on Full Bundle Cases.

1. Endplate face fixed All webs fixed *first iteration model	4. Both sides outer webs fixed
2. Endplate face fixed Outer webs fixed	5. Both sides inner webs fixed
3. Endplate face fixed Inner webs fixed	6. Endplate face fixed Lower webs fixed

The goal was to match the PIE in terms of the overall sag, especially for the upper half and outer elements, and the 'S' profile of the lowest rods. Figures 57 to 59 show the endplate constraint for tests 2, 3, and 6 listed in Table 8. Table 9 presents axial and side views of the vertical deflections for the 6 different web constraint configurations.

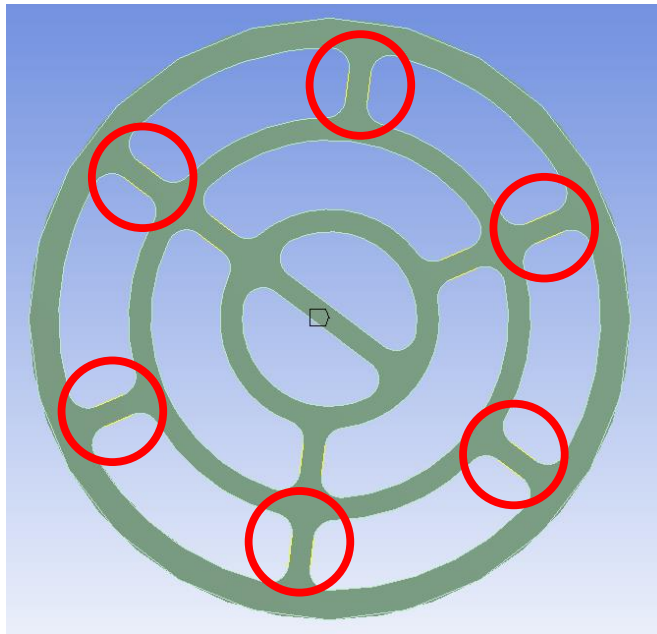


Figure 57: Test 2 - one endplate faced fixed, outer webs fixed

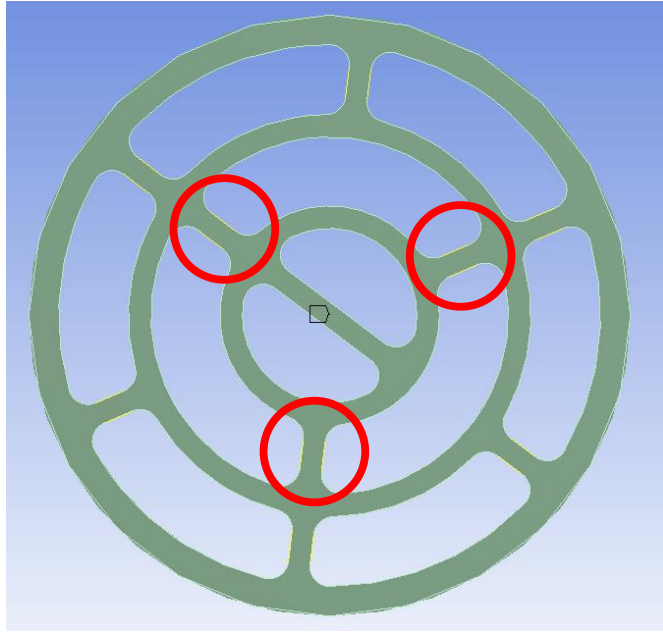


Figure 58: Test 3 - one endplate faced fixed, inner webs fixed

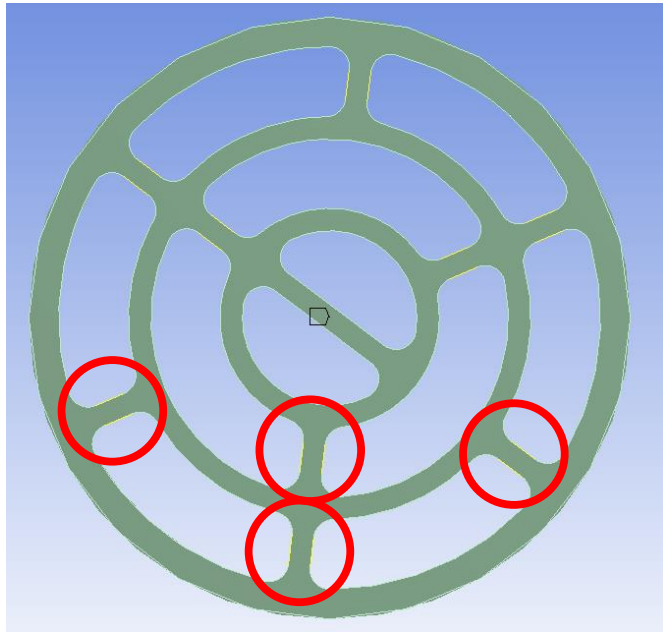


Figure 59: Test 6 - one endplate faced fixed, lower 4 webs fixed

Table 9: Vertical deflections of various endplate radial web axial constraints.

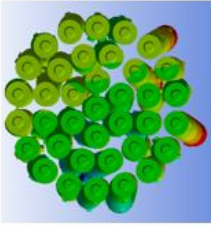
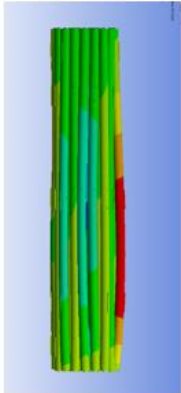

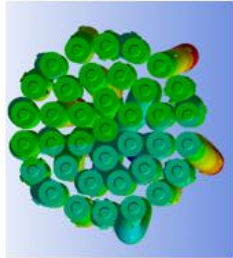


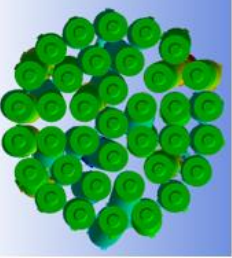

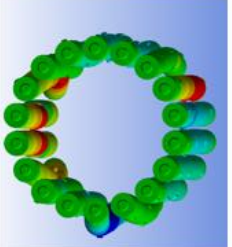
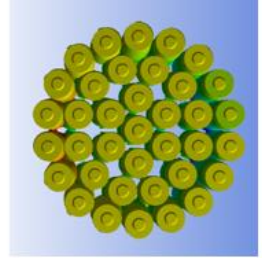
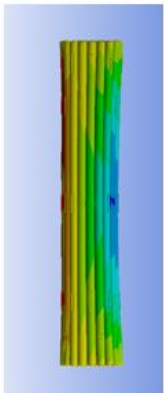
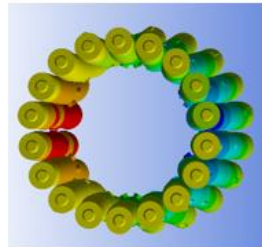
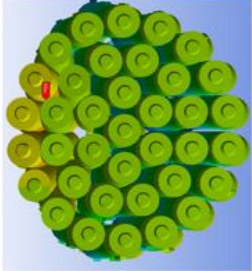
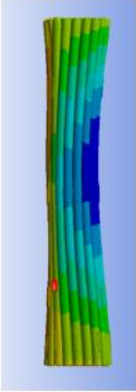

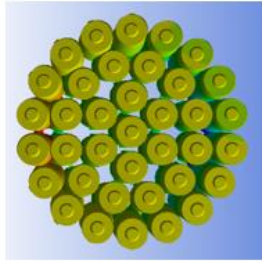
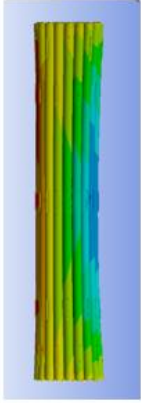

Boundary	Axial View	Side View	Outer Rods View
One end plate fixed All webs fixed 6.3x scale			
One end plate fixed Outer webs fixed 8.2x scale			
One end plate fixed Inner webs fixed 13x scale			
Both sides inner webs fixed 16x scale			

Table 9: Continued vertical deflections of various endplate radial web axial constraints.

<p>Lower webs fixed One end plate fixed 7.6x scale</p>			
<p>Both sides outer webs fixed 17x scale</p>			

When all the webs or just the outer webs were constrained, the top elements bowed outwards. When both ends had either the outer or inner webs fixed, the outer rods bowed inwards including the side rods which are supposed to bow out like Figure 14. The axial constraint on the lowest 4 webs as shown in Figure 59 best represents the bundle heat up tests. This configuration allowed the upper webs to bend and enabled the rods at the top to sag. After the sensitivity analysis on the boundary conditions was performed, Test case 6 garnered the suitable deflection shape that matched the PIE and bundle heat up tests. Fixing the lower 4 webs was selected to proceed to study the effects of loads and crept PTs.

7.1.2.3 Effects of applied load on bundle deformation

With the boundary conditions established, a sensitivity study of the loads was performed. The goal was for the outer elements along the bottom of the bundle to contact the PT and to fit the contour. But once the pressure tube was expanded with 8% creep, rods 12, 11, 8, and 7 disengaged contact with the pressure tube. To mimic the effect of creep on the rods, increased vertical forces were considered. Instead of running the simulation for a long time to simulate creep, the same deformed shape was achieved by applying a force. Increasing the thermal load was not considered because the goal was a downward sag rather than a uniform radial expansion. Figures 60 to 63 show the axial view of vertical deflections of both 0% and 8% PT creep with downward forces of the pellet weight of about 6.1 N and arbitrary loads of 60 N, 120 N, and 240 N respectively. The effects of the applied loads can be estimated to be greater than the pellet weight because of the sag due to creep and the hydraulic drag load as high as 7300 N on the channel [49].

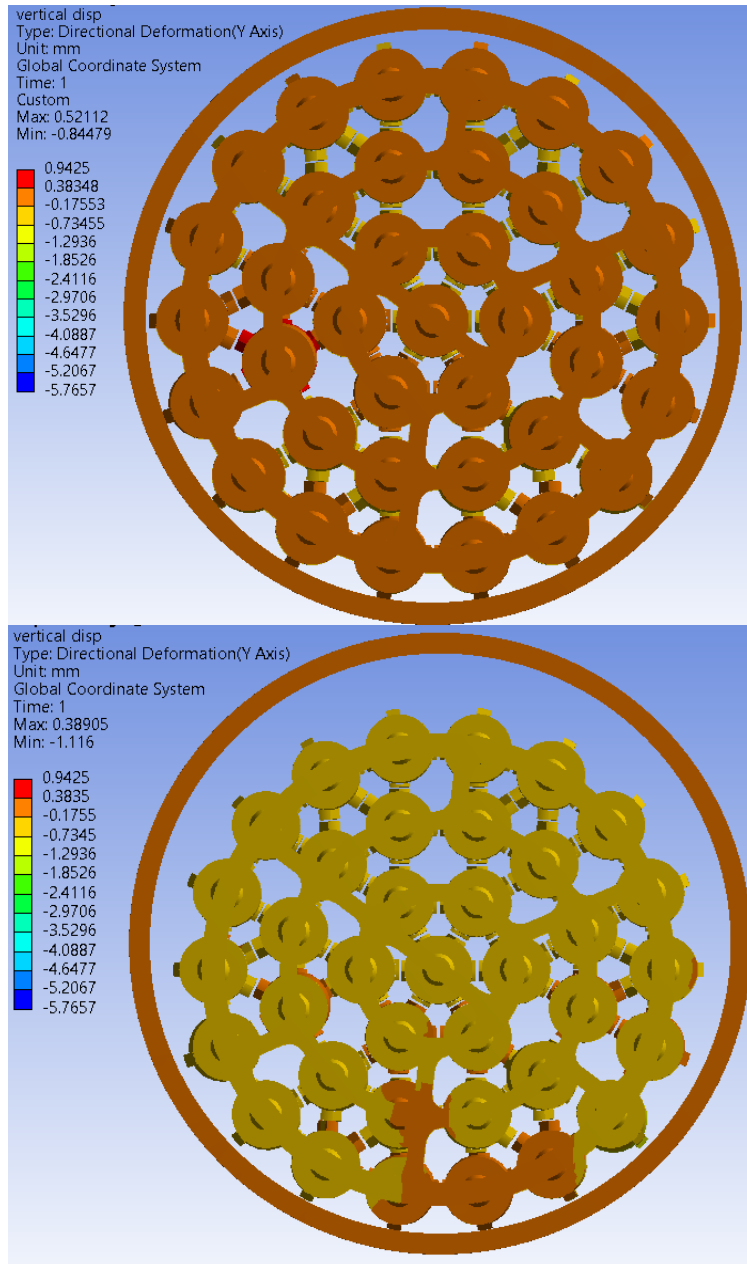


Figure 60: Axial view of vertical deflections (mm) of entire bundle with nominal PT diameter (top) and 8% diametral creep (bottom) with pellet weight at true scale.

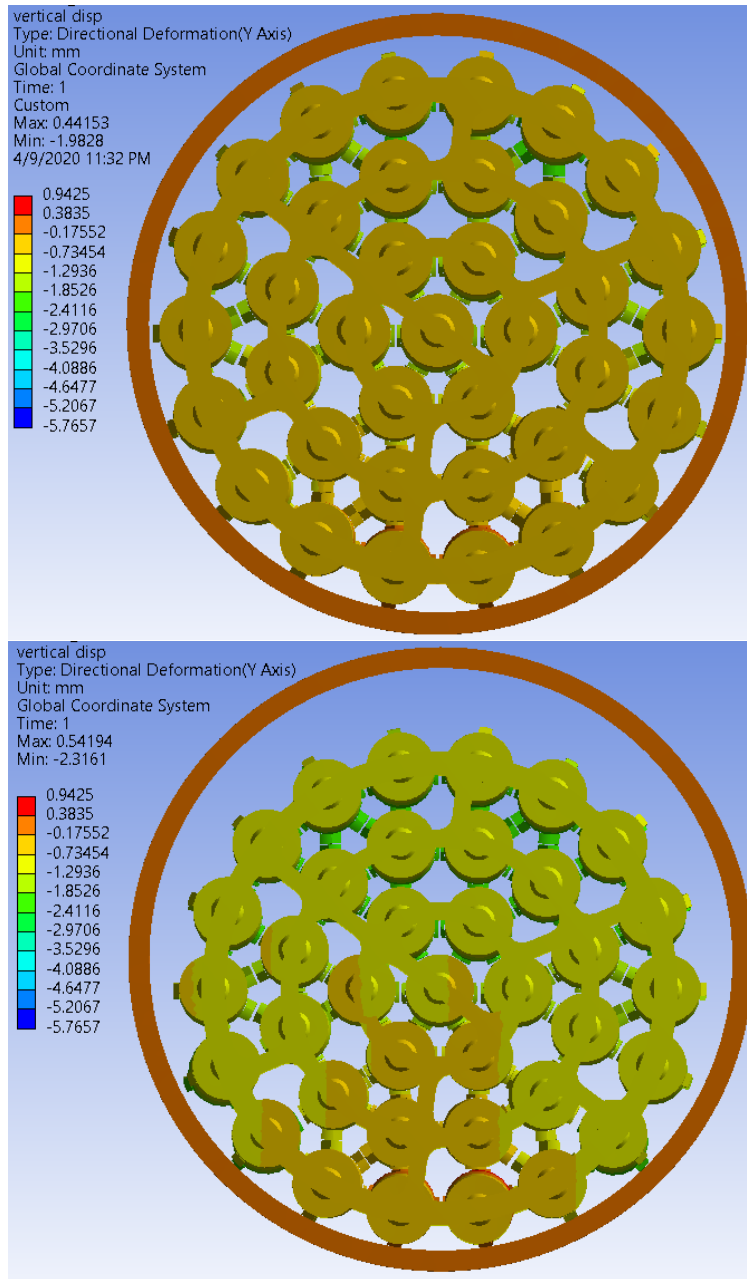


Figure 61: Axial view of vertical deflections (mm) of entire bundle with nominal PT diameter (top) and 8% diametral creep (bottom) with 60 N at true scale.

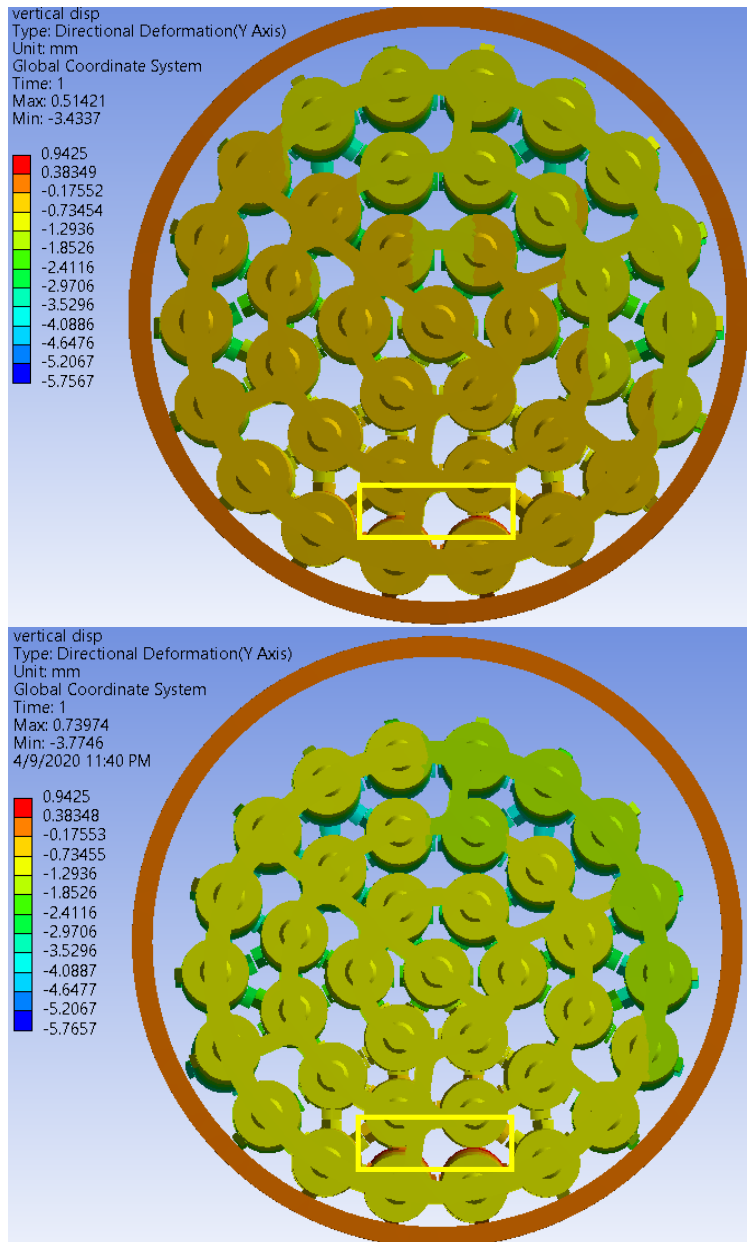


Figure 62: Axial view of vertical deflections (mm) of entire bundle with nominal PT diameter (top) and 8% diametral creep (bottom) with 120 N at true scale.

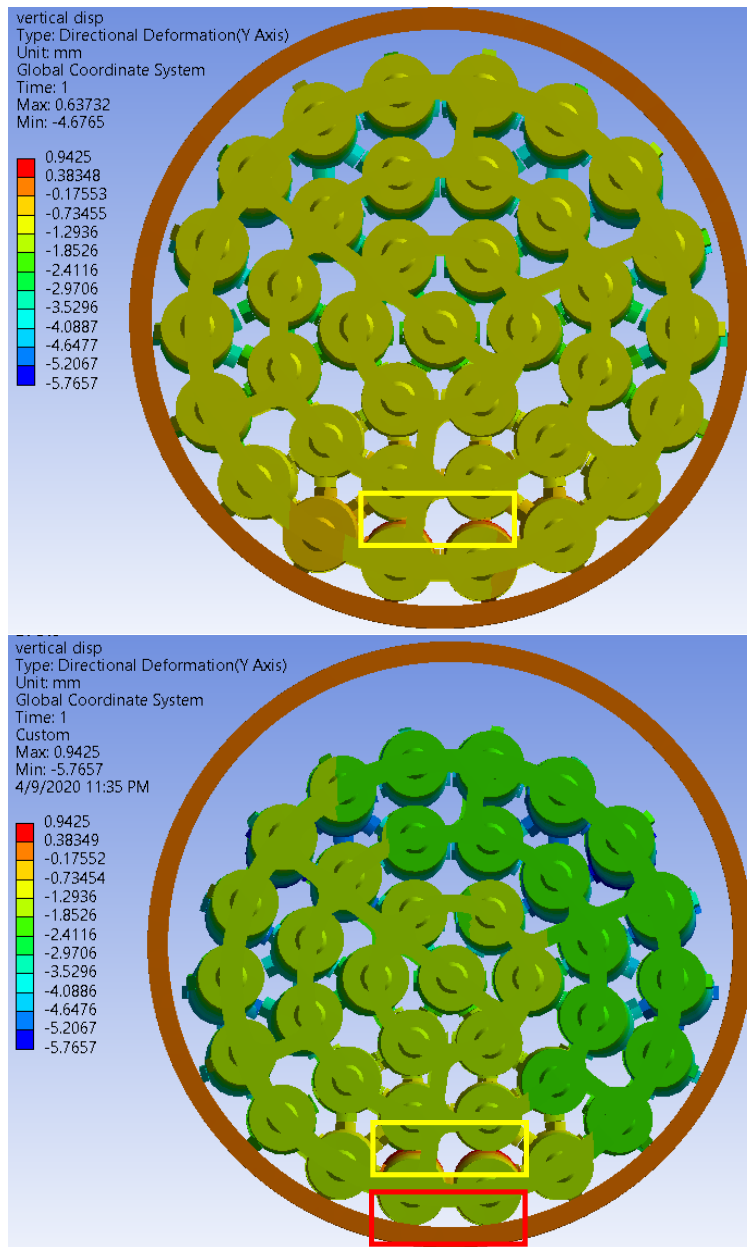


Figure 63: Axial view of vertical deflections (mm) of entire bundle with nominal PT diameter (top) and 8% diametral creep (bottom) with 240 N at true scale.

With a load of 240 N, rods 6 and 13 exhibited BP to PT contact even with 8% PT creep. However, the greater force and diameter causes the lowest two endcaps to contact the PT with 8% creep as highlighted in red in Figure 63. Furthermore, the quarter plane was determined to be the critical region with loads of 120 N and 240 N applied due to the sheath to sheath contact in yellow highlight. The load of 60 N was selected to proceed with- a PT diametral creep comparative study as the 120 N and 240 N were seen to be excessive due to the sheath to sheath, and endcap to PT contacts. The only expected contact is between the SPs and the lower elements' BPs and the PT.

The baseline vertical deflections for the 60 N model are plotted and compared to the undeformed bundle for the outer elements in Figure 64.

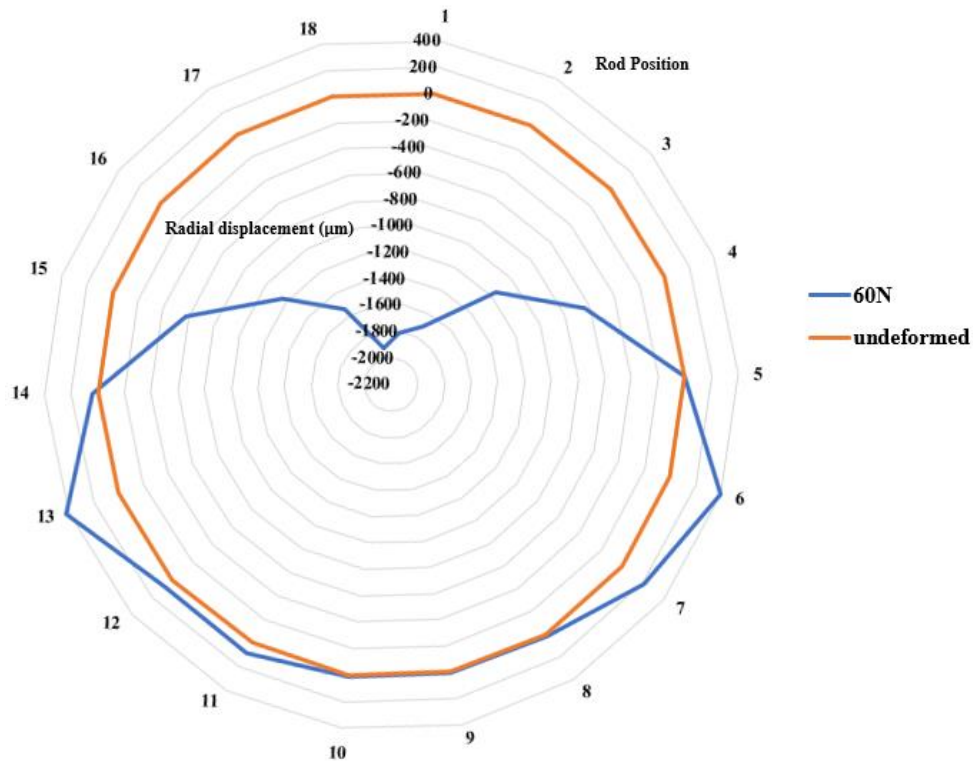


Figure 64: Plot of outer elements' radial displacement (μm) compared to undeformed bundle

Figure 64 shows the downward sag of all the elements compared to the original bundle and outward expansion of the lower side elements such as from rods 13 to 6.

7.2 Crept PT Bundle Deformation Comparisons

7.2.1. 37-Element Final Bundle Model Description

With the lower 4 webs constrained and a selected vertical force of 60 N, the PT diametral creep was incorporated. PT creep was represented by a circular tube with increasing diameter of 0%, 2%, 4%, 6%, and 8% of the nominal diameter. The axial views of the bundles contained within the respective pressure tubes are shown in Figures 72 to 76 in appendix D.

7.2.2. Results

The results of the boundary conditions and loads sensitivity analysis were implemented for a PT diameter with 0%, 2%, 4%, 6%, and 8% diametral creep for comparison. The axial views of the vertical deflection results of the entire bundle, midplane, and quarter planes at true scale are outlined from Figures 65 to 69.

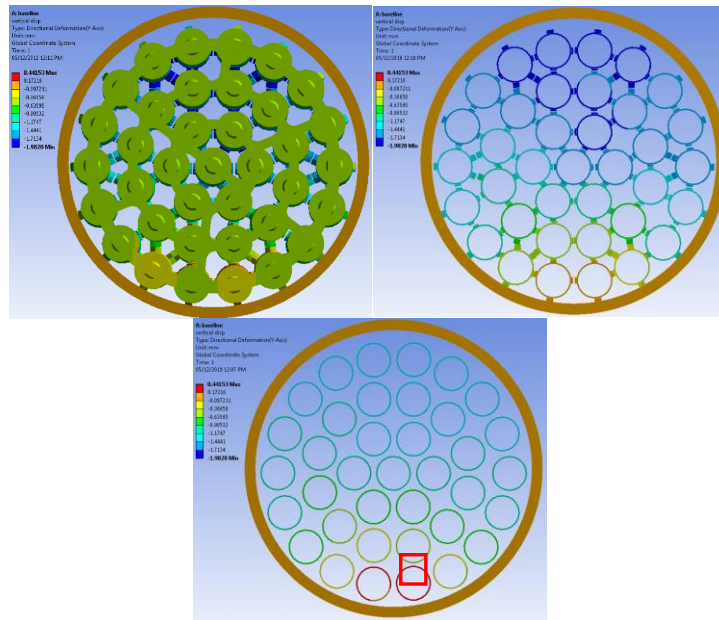


Figure 65: Axial view of vertical deflections (mm) entire bundle (left), midplane (right), quarter plane (bottom) of nominal PT diameter at true scale.

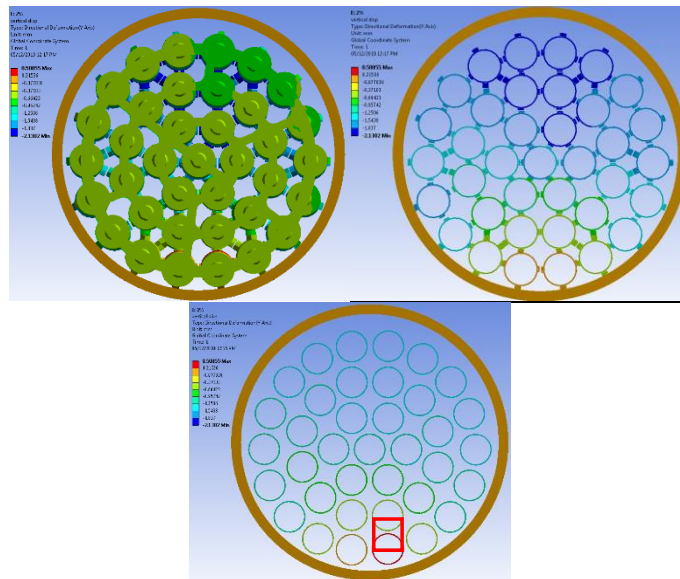


Figure 66: Axial view of vertical deflections (mm) entire bundle (left), midplane (right), quarter plane (bottom) of 2% crept PT diameter at true scale.

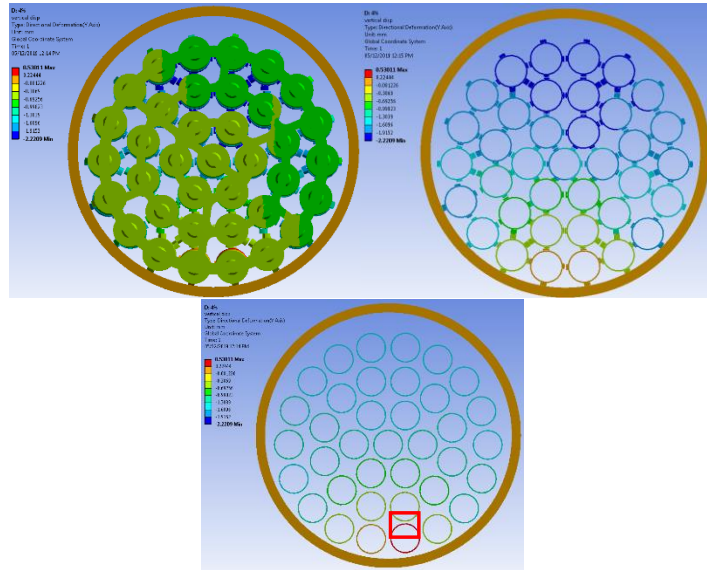


Figure 67: Axial view of vertical deflections (mm) entire bundle (left), midplane (right), quarter plane (bottom) of 4% crept PT diameter at true scale.

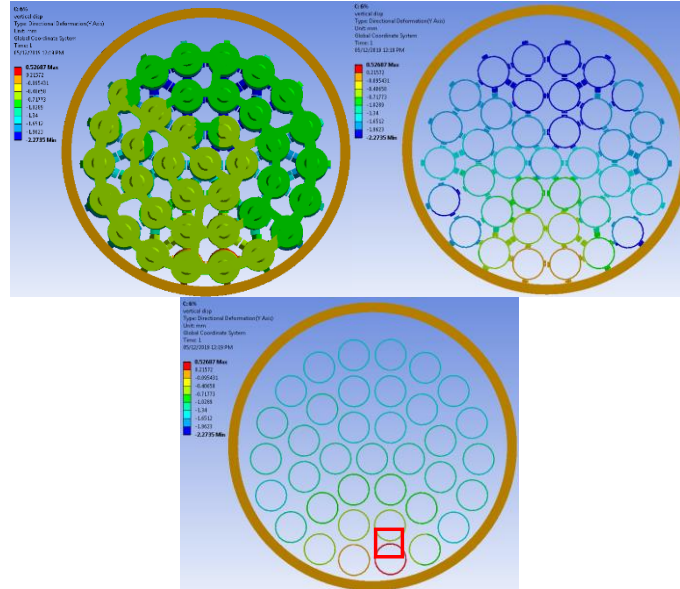


Figure 68: Axial view of vertical deflections (mm) entire bundle (left), midplane (right), quarter plane (bottom) of 6% crept PT diameter at true scale.

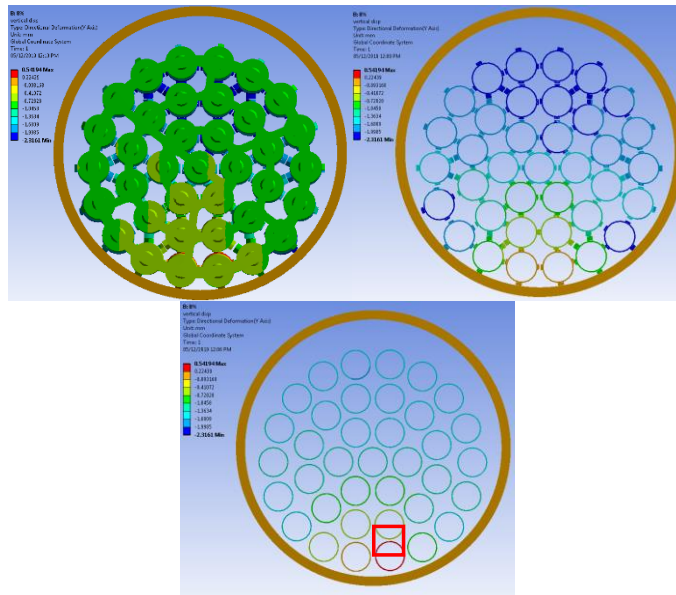


Figure 69: Axial view of vertical deflections (mm) entire bundle (left), midplane (right), quarter plane (bottom) of 8% crept PT diameter at true scale.

Contact between rods 24 and 9 was likely with increasing PT diameter highlighted in red. The gap clearance between the sheath to sheath surfaces was measured and is listed in Table 10. The undeformed bundle has a gap distance of 1.72 mm.

Table 10: Gap measurement between rods 24 and 9.

Creep (%)	Gap distance (mm)
0	0.825
2	0.696
4	0.643
6	0.623
8	0.5741

The trend is generally linear and shows a decrease in the gap with increasing PT diametral creep. The trend is more evident in Figure 70.

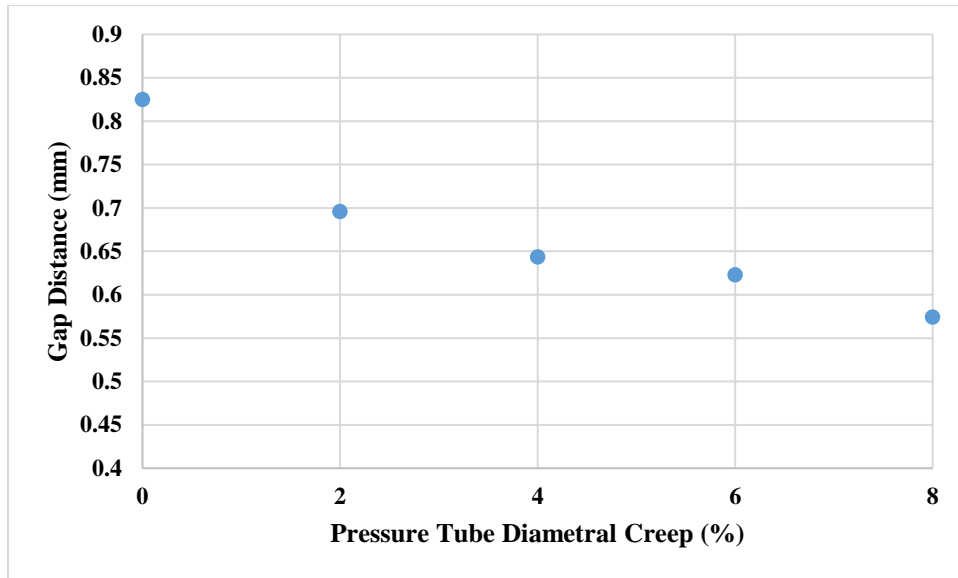


Figure 70: Gap distance between rods 24 and 9 with increasing diametral creep.

8. Discussion

First iteration model

The first iteration of the full bundle model with contact was demonstrated using the HPC cluster. Figure 53 shows the axial view of the full bundle at true scale, and contact between the appendages and with the pressure tube was evident. The red highlights show the spacer pads actually contacting and sliding under the loads. Though the forces and temperature were not enough to cause the SPs to completely slip and contact the sheath surface, the sliding causes the sub-channel area to become smaller and could affect the coolant flow through the sub-channels. Apart from the SP slippage, obstruction of the sub-channel flow was also caused by sagging. The centre endplate radial web completely covered the sub-channels as circled in yellow. These highlighted areas are regions of interest for future fluid studies coupled with a structural analysis.

The first iteration model has some inconsistencies with the PIE bundle heat up test data especially with the outer elements. A bundle's lifetime in a channel would cause most of the elements to sag or behave in a manner similar to the PIE findings. The outer elements in the upper half of the bundle show an upward bulge, in particular rods 16, 17, 18, 1, 2, and 3 as illustrated in Figure 54. The rods in the lower half qualitatively align with the PIE by expanding outwards to fit the contours of the pressure tube. Examining just the lowest two rods in Figure 55 shows the 'S' shape predicted by the small scale tests and the same order of magnitude seen by the PIE. The lowest two rods are calibrated to the rod models with the sheath sitting on the pressure tube and could explain the similarities of the deformed shape.

Closer inspection of the endplate deformation highlights the differences between how the endplates react to different boundary conditions. With only the radial webs axially fixed in Figure 56a), the localized bending is evident on both the webs and the flanges where the rods are connected via the endcaps. Compared to when the entire face was constrained, there is a greater degree of waviness when only the webs are fixed. This suggests that the endplate bends locally to accommodate the axial compressive stress build up. This relief of the axial stress build up can also be seen when observing the endplate vertical deflection magnitude; the

web-constrained side slightly lifts up while the face-constrained side slightly drops. This suggests a vertical slanting of the bundle to relieve the compressive stress from axially fixing both sides.

The compressive stress accumulation of the bundle could account for the greatest bowing found on rods attached closest to the radial webs, as seen on PIE and bundle heat up test reports. Experimental profilometry showed that the rod's location on the endplate determined the rods' shapes. In fact, elements nearest to the radial spokes experienced the most outward bowing [31]. The report also links the large deformation of the rods near the webs to the endplate dishing caused by the coolant hydraulic load which supports the boundary condition of axially constraining the webs. The rods closest to the fixed webs could explain why the top outer elements bowed upwards to contact the pressure tube. Given the importance of boundary conditions in garnering the suitable deformation profile, a sensitivity study on the boundary conditions was performed and outlined in Section 7.1.2.2.

Boundary Condition Sensitivity Test

The first iteration of a full bundle, and with literature from Whiteshell and Chalk River Laboratories, showed that the endplate, more specifically the radial web, played a significant role in the deformation profile [13]. The upward bulge of rods 16, 17, 18 can be attributed to the fixed radial web closest to rod 29. This axial constraint causes an upward bowing of rod 29 that pushes the above rods all upwards. Rods closest to other radial spokes also experience the most bowing. This observation is also consistent with out-reactor tests done at SPEL and analysis by Whiteshell Laboratories [31].

The boundary condition sensitivity study was performed by constraining different combinations of radial webs as listed by Table 8. The axial and side views, as well as the outer rods side axial views, are shown in Table 9. Axially fixing one endplate and the radial webs of the other endplate provided enough constraint to cause the upwards bowing of rods especially for rods 2, 17 and 29. Fixing the inner and outer radial spokes of both endplates did allow the top rods to sag downwards, but even the side rods bowed inwards rather than outwards to fit the contours of the pressure tube. To capture the downward sag of the upper half rods, the outward bow of the side rods, and the 'S' shape of the lowest rods, one endplate had to be constrained and the radial webs of the other endplate had to be strategically fixed. Test case 6 on Table 8 achieved all the targets and most closely fits the bundle heat up tests and PIE data. Constraining only the lowest 4 radial webs and the endplate of the other side allowed the top rods to sag down and the side rods to bulge out to

contact the pressure tube, while still providing an 'S' shape of the lowest 2 rods. This boundary condition was selected for the final 37 element bundle model.

Loads sensitivity test

Determining the appropriate vertical load such that the side rods bow outwards to fit the PT contours was the goal of the load sensitivity analysis. Creep is the main driver for the downward sag of the bundle, but running the model for a bundle lifetime of 9 months was unrealistic. Increasing the thermal loads would cause uniform expansion and was not considered for the sensitivity test. Vertical downward forces of the pellet weight, 60 N, 120 N and 240 N were applied on all 37-elements for the bundle at nominal diameter and 8% diametral creep. The increased forces allowed for the lower and side outer rods' BPs to contact the PT even up to rods 14 and 5 with nominal PT diameter. However, when observing the 8% crept PT, applying 240 N allowed the BPs of up to rods 13 and 6 to contact the PT as shown in Figure 63, while only BPs of up to rods 12 and 7 contacted the PT with 120 N and 60 N. More side elements contacting the PT means a greater pronounced deformed profile especially with the lower side elements bulge. Having just the pellet weight without creep effects was insufficient to cause the side elements to bow enough to contact the PT.

The greater force and diameter of 120 N with 8% creep also caused more endplate drooping to the point of having endcap to PT contact. There was also sheath to sheath contact on the quarter plane with 240 N and 120 N vertical loads. 60 N was chosen as the logical vertical force to avoid the unrealistic endcap to PT contact, and sheath to sheath contact during normal operating conditions, while still allowing some side elements to contact the PT as seen in Figure 61.

Effect of PT creep using the final 37-element bundle model

With a working baseline model and sensitivity studies on boundary conditions and vertical forces completed, the PT diameter was expanded from 0% to 8% diametral creep. As expected, an increase in bypass flow area was observed with increasing pressure tube creep. There were fewer bearing pads contacting the pressure tube on the sides as the PT diameter expanded. When observing the midplane, the sub-channels maintained their areas because of the spacer pads preventing further sag and highlighted the robust design of the spacer pads.

However, the quarter plane was deemed to be the critical region due to the lack of spacer pads. In fact, the quarter plane was where bundles with 120 N and 240 N all

experienced sheath to sheath contact between rods 24 and 9. This might be interpreted as conditions under an accident. When 60 N was applied, the gap between rods 9 and 24 was measured and compiled in Table 10. There is an overall linear trend between increasing the PT diameter and a reduction in the sheath to sheath clearance. However, when the load and BC remain constant without any fluid consideration, the PT can creep even up to 8% while maintain clearance between the rods. When considering just a purely structural analysis with the set boundary conditions and loads, there appears to be adequate gap clearance even for a worst-case scenario like 8% diametral creep.

9. Limitations

A finite element model of a 37-element CANDU fuel bundle was established, along with a better understanding of endplate boundary conditions and PT diametral creep, but this model has some limitations. First, the rods were empty, and did not account for the increased stiffness or heat generation from the pellets within the fuel sheath. Next, the overall deformation shape was compared with the PIE results both from out-reactor and bundle heat up tests. However, the current model does not account for some of the deformations seen that may be observed in the PIE, such as endplate dishing and doming, and bundle parallelogramming. A partial 12 rod model was validated by Lt. Soni with experiments from CNL, but experimental validation for the full bundle is required. Material considerations with irradiation effects were not included. In addition, pressure tube creep also consists of PT sagging and axial elongation which were not accounted for. Finally, there are no fluid considerations to determine any temperature distributions or the effects of cooling on the rods.

10. Conclusion

The objectives of the research were to develop a finite element model of an empty 37-element CANDU fuel bundle and to study the effects of pressure tube diametral creep on the bundle deformation. Using the commercially available finite element software, ANSYS, and HPC hardware and software from CMC Microsystems, a full bundle deformation model was achieved - a first ever for a 37-element bundle. By studying the PT diametral creep of 0%, 2%, 4%, 6%, and 8%, greater insight into the bypass flow and sub-channel area became available. The model was simplified by excluding fuel performance considerations such as the UO₂ fuel pellets, heat generation, FGR, PT sag and elongation and anisotropic material properties. Rather, loads of vertical force, gravity, and constant temperature were used to mimic experimental profilometry results from PIE and bundle heat up tests.

Small scale tests using a 1-rod model inside a pressure tube were used to determine which boundary conditions and loads to apply that qualitatively matched profilometry results of an 'S' style deflection shape. The following are the conclusions from the small scale tests:

- Axially fixing the endplates and bonding the centre BP to the PT garnered the 'S' shape and the most realistic deformations.
- Applying a thermal gradient with pellets inside the rods resulted in an 'S' shape while a constant temperature garnered the 'S' shape for an empty rod.
- Both the in-line and staggered bearing pad configurations resulted in an 'S' shape with pellets and a thermal gradient applied.

To proceed with the full bundle model, the boundary conditions and loads required adjustments. The axial constraint on the endplates was found to be too restrictive on all 37 elements and caused some rods to buckle under the compressive stresses. Certain radial spokes on one endplates were axially fixed to provide the same restriction as the entire endplate, while allowing localized bending for the rods connected to the flanges. A sensitivity analysis was performed on the boundary conditions to determine the axial constraint that best aligned with the experimental tests. Constraining only the lowest 4 webs allowed the bundle to sag, the endplates to droop, the top elements to bow downwards, and the bottom and side elements to bow outwards to fit the PT contours.

A load sensitivity test was also performed by varying the vertical load from pellet weight, 60 N, 120 N, and 240 N on a baseline diameter and 8% crept PT. Increased force allowed for a more pronounced deformation effects and more side rods to contact the PT on the 8% diametral creep. Greater forces also caused a more dramatic endplate drooping effect with the endplate contacting the PT with 240 N. Sheath to sheath contact was also noticed at the quarter plane for 120 N and 240 N vertical loads. 60 N vertical was a balance between bundle sagging effects while preventing sheath to sheath and endplate to PT contact.

With the loads and BCs established, a comparative study was conducted on the PT diametral creep by changing the values from 2%, 4%, 6%, and 8%. An increase in bypass flow area was observed with increasing diameter. However, the sub-channel areas in the midplane remained constant with changing diameters due to the spacer pads preventing further sheath sagging. The quarter plane was determined to be the critical plane at risk of dry out and sheath to sheath contact with increasing diametral due to the omission of any spacer pads preventing further rod deformation and reduction in sub-channel area.

11. Recommendations

The finite element analysis was performed to study the 3D deformation of a 37-element CANDU fuel bundle under the effects of pressure tube creep. Though the thesis demonstrated a working structural full bundle model with contact implemented, recommendations are outlined to provide a greater understanding of the thermal-mechanical response of the bundle with pressure tube creep.

1. With a working full empty bundle model, a more realistic thermal-mechanical model can be achieved by combining the current thesis with Mr. Krasnaj's work on the pellet-fuel rod interaction. His research studied the thermal induced bowing of fuel elements caused by applying a power rating on the encased pellets. He also looked at the stiffness due to the inclusion of pellets inside the sheath – both as individual pellets and as a monolithic entity. Incorporating Mr. Krasnaj's pellets into the current empty full bundle would allow for a more realistic thermal model with an actual power rating. Mechanically, the rod stiffness would not need any calibration of changing the material properties because the pellets themselves would actually be included and aid in stiffening the rods. Different power rating and flux distributions could be acquired to model a specific in any channel under NOC or accident conditions. The biggest anticipated challenge would be acquiring additional computing hardware due to the increase in contact pairs including pellet to pellet, pellet to fuel rod, spacer to spacer pad, and bearing pad to pressure tube.
2. However, even with the current work both with and without pellets, the model could be coupled with a fluid study to determine the bundle temperature profile and to quantify the effects of increasing the PT diameter on bundle deformation. Using the PT nominal diameter, a fluid analysis would allow for a closer observation of how the rod sagging and changes in sub-channel areas are affected. This may help to better understand the fitness for return to service criterion. Single phase laminar flow could be the starting point for a comparison between different PT diameters. Different turbulence models can then be included and coupled with physics to study severe accidents. The same analysis can be continued using the CANFLEX bundle with the turbulence inducing buttons. CFD training and familiarization with turbulence models are anticipated to hinder progress in addition to the added computational demands of coupling a mechanical and fluid analysis

3. The current work obtained suitable boundary conditions for the full bundle by matching the deformation to PIE results, yet the most realistic way is load all 12 or 13 bundles in a fuel channel. With an entire fuel channel, the axial deformation for each bundle would be limited by the neighboring bundle and hydraulic load while still allowing each rod to have localized bending on the endplate. Modeling the entire channel would take away the guess work, and trial and error, from just using the PIE to determine appropriate boundary conditions. In addition, with adequate hardware, the aforementioned inclusions of pellets and fluid study could be included for a robust full channel analysis for different power ratings and flux distributions for both NOC and accidental environments. While this may be the ultimate goal in modeling techniques, an equally robust supercomputer must be utilized.
4. Any simulations must be verified and validated with experimental data, thus bundle heat up tests or further PIE results could be beneficial in validating the full bundle model. Currently, because of the proprietary nature of sag profiles and bundle deformation, PIE and bundle heat up data available are from the 1980s. Furthermore, due to the lack of pellets in the finite element model, the experimental data at hand presently can only verify the correct shape of the sag profile. The closest test that most aligns with the current model would be a bundle heat up test of an empty bundle. The finite element model can be adjusted according to how the experiment was set up and constrained because contact was already verified. Experimental data would be the most valuable information to validate the correct functioning of the finite element model.
5. CANDU fuel bundles within the channel are known to experience excitations and have a frequency response due the coolant flow. As a result, a study on the acoustics of the fuel bundle is necessary and its effect such as the bearing pad and pressure tube wear. Currently, the finite element model is for a static structural analysis, however, introducing frequencies to the model would allow for a modal analysis. Similar difficulties remain with the static analysis, such as determining the most appropriate boundary conditions and loads, while introducing new challenges in terms of familiarization with the software.
6. The next recommendation is the acquisition of more nuclear specific data such as material properties and reactor conditions. Phenomena such as radiation hardening, sheath oxidation, and radiation creep all affect the material properties of the Zircaloy-4 cladding and Niobium infused pressure tubes. Furthermore, once pellets are incorporated, then data on pellets and CANLUB are required for a more accurate simulation. With the

current thesis, sensitivity analyses were performed on the boundary conditions and loads to best qualitatively match the sag as seen as by the PIE results. A better understanding of the fuel channel environment would allow for an improved deformation behaviour justified by actual conditions under both normal and accidental conditions. The proprietary nature of some information once again makes it a challenge in obtaining these specific data.

7. Accident Tolerant Fuel is also a domain that could be explored by the CANDU industry, more specifically is the application of a chromium coating on the Zircaloy sheath. A Chromium coating of a few microns demonstrate a slight improvement of a single rod deformation and oxidation of the sheath. Preliminary studies also show minimal impact on the neutronics and burn up of the fuel. The goal would be to apply the coating on a full bundle then perform a sensitivity study to determine the optimal coating thickness. A fuel performance code would be used to see the effects on fuel performance despite the added coating. The anticipated difficulty comes from the increased computing demands, particularly from the increased mesh size. Surface coatings require a solid element base, compared to the shell elements currently employed, and could increase the node count because the full bundle must be coated.
8. Redesigns and sensitivity analyses of the physical geometry of the bundle can also be explored with a working full bundle finite element model. The changes would support using less material to save on costs or adding features to lessen sheath sag, while maintaining the same structural and physical capacities. Some of the options include, bearing pad and spacer pad height changes, adding more planes of bearing pads, and changing the thickness of parts. The full bundle models and PIE results showed that the location of where the rods are welded on the endplate played a significant part on how the rod bowed. Thus, a redesign of the endplate could be conducted that imparts more stiffness to the rods while using less material and aiding in fluid flow through the sub-channels.

12. References

- [1] R. Chandrappa, S. Gupta, and U. C. Kulshrestha, *Coping with climate change*, no. 1. 2011.
- [2] “Climate Change and Nuclear Power 2018,” Vienna, 2018.
- [3] IAEA, “International status and prospects of nuclear power,” 2010.
- [4] “CANDU Technology.” [Online]. Available: <https://cna.ca/technology/energy/candu-technology/>
- [5] “Supply Overview,” *Independent Electricity System Operator*. [Online]. Available: <http://www.ieso.ca/power-data/supply-overview/transmission-connected-generation>.
- [6] M. H. A. Piro, F. Wassermann, S. Grundmann, B. W. Leitch, and C. Tropea, “Progress in on-going experimental and computational fluid dynamic investigations within a CANDU fuel channel,” *Nuclear Engineering and Design*, vol. 299, pp. 184–200, 2016.
- [7] B. Garland, *The Essential CANDU: A Textbook on the CANDU Nuclear Power Plant Technology*. Hamilton: UNENE, 2014.
- [8] L. C. Walters and A. F. Williams, “Fuel Bundle Deformation Model,” *International Conference on CANDU Fuel*, 2003.
- [9] N. Christodoulou *et al.*, “Modeling In-Reactor Deformation of Zr-2.5Nb Pressure Tubes in CANDU Power Reactors,” *Zirconium in the Nuclear Industry: 11th International Symposium*. January, pp. 518–537, 1996.
- [10] IAEA, “Assessment and management of ageing of major nuclear power plant components important to safety: CANDU pressure tubes,” *IAEA*, vol. 33, p. 107, 1998.
- [11] A. M. Manzer, “CANDU FUEL PERFORMANCE A.M. MANZER Atomic Energy Canada Ltd, Mississauga, Ontario, Canada,” *Atomic Energy Canada Limited*, pp. 19–34.
- [12] P. Chan, “Part 2: Fuel Production,” *R. Mil. Coll. CC533*, pp. 1–133.

- [13] J. Montin, M. R. Floyd, Z. He, E. Kohn, F. D. Branch, and O. P. Generation, “Performance of Two Candu-6 Fuel Bundles Containing Canlub and Non-Canlub Production Elements.”
- [14] N. J. Fisher, M. K. Weckwerth, D. A. E. Grandison, and B. M. Cotnam, “Fretting-wear of zirconium alloys,” *Nuclear Engineering Design*, vol. 213, no. 1, pp. 79–90, 2002.
- [15] M. H. A. Piro *et al.*, “Experimental and Computational Investigations of Flow By-Pass in a 37-Element Candu Fuel Bundle in a Crept Pressure Tube,” *OECD/NEA IAEA Work. Comput. Fluid Dyn. Nucl. React. Safety, Cambridge, USA*, pp. 1–14, 2016.
- [16] W. Hartmann and J. Y. Jung, “Safety analysis methodology for aged CANDU® 6 nuclear reactors,” *Nuclear Engineering and Technology*, vol. 45, no. 5, pp. 581–588, 2013.
- [17] P. Chan, “Part 8 : Fuel and Fuel Channel Accident Analysis, Safety Analysis Fundamentals, Fuel Channel and Fuel R & D,” Kingston, 2015.
- [18] J. Veeder and M. H. Schankula, “Bowing of Pelletized Fuel Elements: Theory and In-Reactor Experiments,” *Nuclear Engineering and Design*, vol. 29, pp. 167–179, 1974.
- [19] H. C. Suk, K. S. Sim, J. H. Park, and G. S. Park, “Thermally-Induced Bowing of CANDU Fuel Elements,” Korea Atomic Energy Research Institute.
- [20] S. G. Kandlikar, “Critical Heat Flux in Subcooled Flow Boiling - An Assessment of Current Understanding and Future Directions for Research,” *Multiphase Science and Technology.*, vol. 13, no. 3, pp. 207–232, 2001.
- [21] “G-144: Trip Parameter Acceptance Criteria for the Safety Analysis of CANDU Nuclear Power Plants,” Canadian Nuclear Safety Commission, May 2006.
- [22] K. Lassmann, “The structure of fuel element codes,” *Nuclear Engineering and Design.*, vol. 57, no. 1, pp. 17–39, 1980.
- [23] M. Göring and A. Fay, “Method for the analysis of temporal change of physical structure in the instrumentation and control life-cycle,” *Nuclear Engineering and Design*, vol. 45, no. 5, pp. 653–664, 2013.

- [24] S. D. Yu, M. Tayal, and P. N. Singh, “Improvements, Verifications and Validation of the Bow Code,” pp. 38–51, 1995.
- [25] M. Tayal, “BOW : A Computer Code to Predict Lateral Deflections of Composite Beams.” *The 9th International Conference on Structural Mechanics in Reactor Technology*, Switzerland, 1987.
- [26] M. S. Cho, K. S. Sim, H. Chun Suk, and S. K. Chang, “Static strength analysis of CANDU-6 reactor fuel bundle,” *Nuclear Engineering and Design*, vol. 200, no. 3, pp. 407–419, 2000.
- [27] C. J. P. J. Krasnaj, “A Solid Element Approach to Analyzing CANDU Fuel Element Behaviour Under Post-Dryout Heat Transfer Conditions.” Kingston: RMC Thesis, 2015.
- [28] R. Soni, “ Analyzing the 3-Dimensional Deformation Behaviour of An Empty CANDU Fuel Bundle Using the Finite Element Method,” Kingston: RMC Thesis, 2017.
- [29] F. Abbasian, G. I. Hadaller, and R. A. Fortman, “Single-Phase and Two-Phase CFD Simulations of the Coolant Flow Inside a Bruce/Darlington CANDU Flow Channel,” *NURETH-16*, pp. 7820–7829, 2015.
- [30] F. Abbasian, S. D. Yu, and J. Cao, “Experimental and numerical investigations of three-dimensional turbulent flow of water surrounding a CANDU simulation fuel bundle structure inside a channel,” *Nuclear Engineering and Design*, vol. 239, no. 11, pp. 2224–2235, 2009.
- [31] D. Dennier, A. M. Manzer, M. A. Ryuz, and E. Kohn, “Element Bow Profiles from New and Irradiated CANDU Fuel Bundles,” *AECL*, no. 5975, 1978.
- [32] A. M. Manzer, “DEFORMATION ASSESSMENT OF EXTENDED BURNUP BRUCE B BUNDLE G85159W.” CANDU Owners Group Inc, 2003.
- [33] R. C. Hibbeler, *Mechanics of Materials 9th Edition*. 2014.
- [34] D. V. Hutton, *Fundamentals of Finite Element Analysis*. McGraw Hill, 2004.

- [35] O. Weck and I. Y. Kim, “Finite Element Method,” *Engineering Design and Rapid Prototyping*, Massachusetts Institute of Technology, 2004.
- [36] K. J. Bathe, “Introduction to Finite Element Analysis or Finite Element Method,” Victoria, 2016.
- [37] R. Kernaghan, “Geometric Nonlinear Finite Element Analysis of Active Fibre Composite Bimorphs,” Carleton University, 2011.
- [38] J. T. Metrisin, “Guidelines for Obtaining Contact Convergence,” *International ANSYS Conference*, pp. 1–29, 2008.
- [39] H. SHI, “Nonlinear Finite Element Modeling and Characterization of Guyed Towers Under Severe Loading,” Columbia, 2007.
- [40] “Introduction to Contact,” ANSYS, December. 2010.
- [41] N. Kim, “Finite Element Analysis of Contact Problem.” Springer, pp. 1–78.
- [42] D. Oatis, “Getting in Touch with ANSYS Contact,” *The Focus*, vol. 5, no. 58, 2007.
- [43] “NX Nastran 10,” TAUCS, pp. 1–97.
- [44] J. Beisheim, “High - Performance Computing for Mechanical Simulations using ANSYS,” *Automotive Simulation World Congress*, p. 33, 2012.
- [45] W. Slagter, “Understanding Hardware Selection to Speedup Your FEA Simulations,” ANSYS, 2015.
- [46] Intel Corporation, “Engineer Productivity Boosted by Higher-Core CPUs,” 2017.
- [47] Idaho National Engineering and Environmental Laboratory, “MATPRO - A Library of Materials Properties for Light Water Reactor Accident Analysis,” vol. 4, pp. 1–241, 2000.
- [48] “Rate Dependent Creep.” Ansys Inc, 2015.
- [49] M. R. Roman, D. V Ionescu, G. H. Olteanu, S. Florea, and A. C. Radut, “Finite Element Modelling of Different CANDU Fuel Bundle Types in Various Refuelling Conditions,” pp. 121–128, 2016.

Appendices

Appendix A: CMC HPC Hardware Specifications



Figure 71: Hardware specifications of CMC Microsystem HPC.

Appendix B: Major Dimensions for 1-Rod Model

Table 11: Major dimensions for 1-rod model

Bundle Component	Dimensions
PT	Thickness: 4 mm Diameter: 100 mm Length: 500 mm
Sheath	Thickness: 0.525 mm Diameter (avg): 13 mm Length: 484.3 mm
Endplate	Diameter: 91 mm Thickness: 1.55 mm
Spacer pad	Height (avg): 0.6943 mm Length: 7.93 mm Width: 2.29 mm
Bearing pad	Height: 1.22 mm Length: 30 mm Width: 2.54 mm

Appendix C: Table of Mesh Settings

Table 12: Mesh settings for full bundle model

Bundle Component	Mesh Setting
PT	2 mm lower order quadrilateral
Sheath	2 mm lower order quadrilateral
Bearing Pad	0.4 mm higher order hexahedral
Spacer Pad	0.5 mm higher order hexahedral
Endplate	1.5 mm higher order quadrilateral
Endcap	Higher order tetrahedral

Appendix D: Full Bundle with crept PT axial views

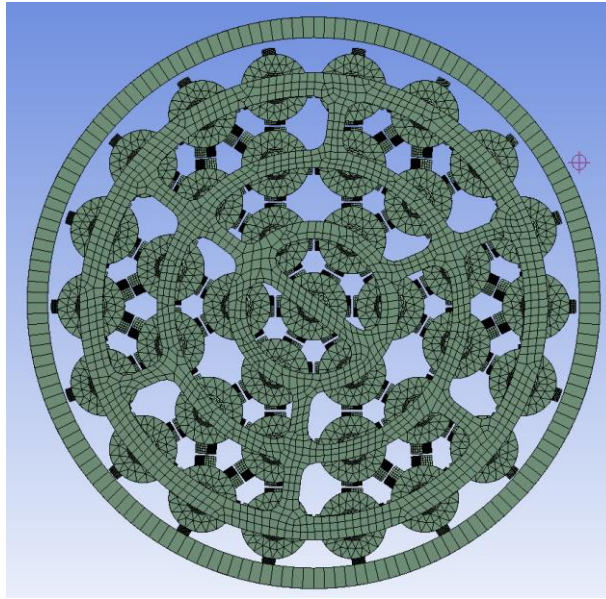


Figure 72: Axial view of full bundle mesh with 0% PT diametral creep.

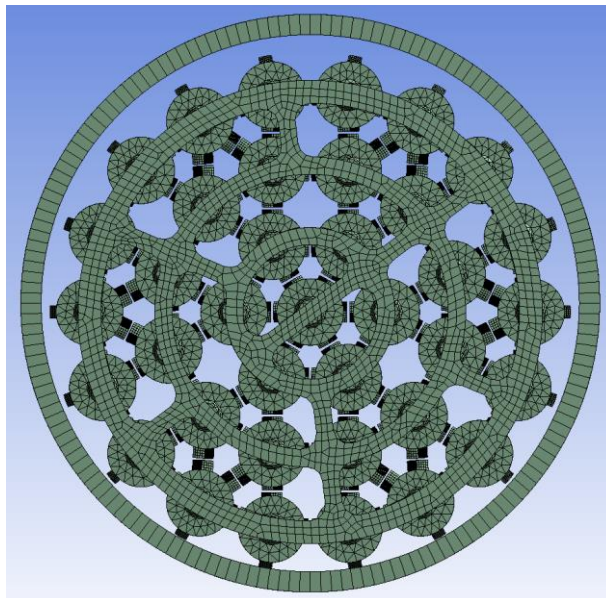


Figure 73: Axial view of full bundle mesh with 2% PT diametral creep.

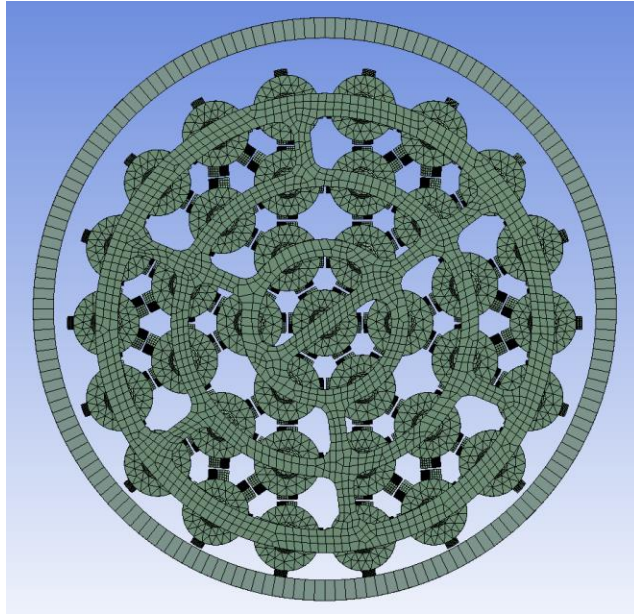


Figure 74: Axial view of full bundle mesh with 4% PT diametral creep.

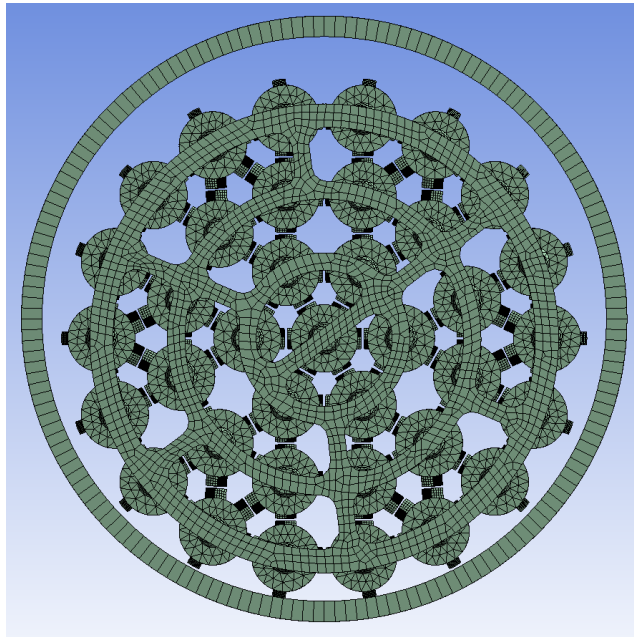


Figure 75: Axial view of full bundle mesh with 6% PT diametral creep.

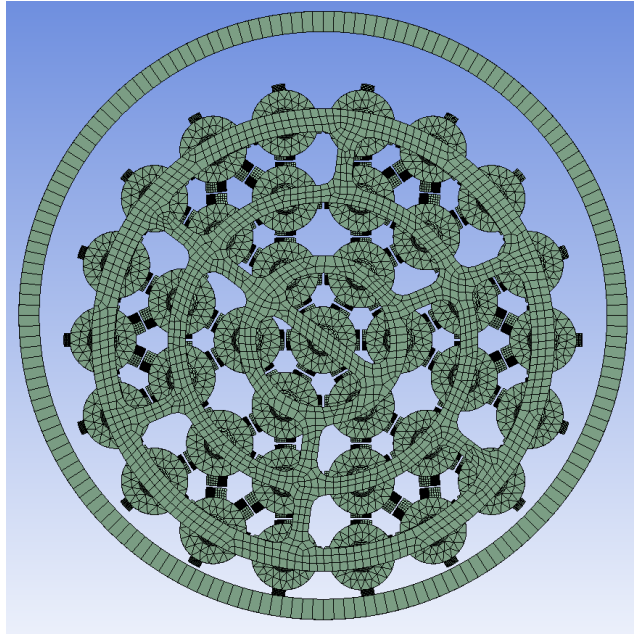


Figure 76: Axial view of full bundle mesh with 8% PT diametral creep.